# HOT JET IGNITION DELAY CHARACTERIZATION OF METHANE AND HYDROGEN AT ELEVATED TEMPERATURES

A Thesis

Submitted to the Faculty

of

Purdue University

by

Ali Tarraf Kojok

In Partial Fulfillment of the

Requirements for the Degree

of

Master of Science in Mechanical Engineering

August 2017

Purdue University

Indianapolis, Indiana

## THE PURDUE UNIVERSITY GRADUATE SCHOOL
## STATEMENT OF COMMITTEE APPROVAL

Dr. M. Razi Nalim, Chair

Department of Mechanical Engineering

Dr. Carlos Larriba-Andaluz

Department of Mechanical Engineering

Dr. Likhun Zhu

Department of Mechanical Engineering

**Approved by:**

Dr. Sohel Anwar

Chair of the Graduate Program

To Sagha, my brother and my parents.

# ACKNOWLEDGMENTS

I would like to express my appreciation and gratitude to my advisor Professor Razi Nalim. I would also like to thank Joe Huerkamp for his help in the machine shop, and my colleagues at the Combustion and Propulsion Research Lab Mohamed Ebrahim Feyz, and Yup Kyong Paik. I also thank Regal Beloit for the statistical analysis training support. This work was partially supported by the National Science Foundation under grant NSF/CBET -1235696 and by Aerodyn Combustion LLC.

TABLE OF CONTENTS

Page

Page

# LIST OF TABLES

# LIST OF FIGURES

Figure Page

Figure Page

Figure Page

# SYMBOLS

| | |
|---|---|
| $m$ | mass |
| $L/D$ | Length over diameter |
| $L/D_H$ | Length over hydraulic diameter |
| $AR$ | Aspect ratio defined as width over length |
| $V_p$ | Volume of pre-chamber |
| $V_m$ | Volume of main chamber |
| $P_{Tot}$ | Total fuel and air pressure |
| $P_{Fuel}$ | Partial pressure of fuel in the mixture |
| $P_{AirResidual}$ | Partial pressure of the residual air in the mixture |
| $P_{AirInitial}$ | Partial pressure of air in the initial mixture |
| $\Delta P$ | Difference in pressure |
| $X_{AirResidual}$ | Ratio of partial pressure of residual air to total mixture |
| $P_{CH_4}$ | Partial pressure of methane |
| $P_{H_2}$ | Partial pressure of hydrogen |
| $\phi$ | Equivalence ratio defined as ratio of the actual fuel/air ratio to the stoichiometric fuel/air ratio. |
| $m_{fuel}$ | Mass of fuel |
| $V_{main}$ | Volume of main chamber |
| $M_{air}$ | Molecular weight of air |
| $A/F$ | Ratio of mass of air to mass of fuel |
| $R$ | Gas constant |
| $T_{air}$ | Temperature of air |
| $t_{on}$ | Time the mass flow controller is "on" discharging fuel |
| $X_{CH_4}$ | Ratio of partial pressure of methane to total mixture |

| | |
|---|---|
| $X_{H_2}$ | Ratio of partial pressure of hydrogen to total mixture |
| $k$ | Constant derived from calibration of the mass flow controller |
| $\tau$ | Chemical ignition delay time |

# ABBREVIATIONS

| | |
|---|---|
| VAC | Voltage alternating current |
| DC | Direct current |
| CPRL | Combustion and Propulsion Research Lab |
| DAQ | Data Acquisition |
| ID | Ignition Delay time |
| MFC | Mass Flow Controller |
| PT | Pressure transducer |
| RPM | Rotation per minute |
| TC | Thermocouple |
| VFD | Variable frequency drive |
| SCCM | Standard Cubic Centimeter per Minute |
| TIGN | Ignition delay time |
| PID | ProportionalIntegralDerivative control process |

# ABSTRACT

Tarraf Kojok, Ali M.S.M.E., Purdue University, August 2017. Hot Jet Ignition Delay Characterization Of Methane And Hydrogen At Elevated Temperatures. Major Professor: M. Razi Nalim.

This study contributes to a better understanding of ignition by hot combustion gases which finds application in internal combustion chambers with pre-chamber ignition as well as in wave rotor engine applications. The experimental apparatus consists of two combustion chambers: a pre chamber that generates the transient hot jet of gas and a main chamber which contains the main fuel air blend under study. Variables considered are three fuel mixtures (Hydrogen, Methane, 50% Hydrogen-Methane), initial pressure in the pre-chamber ranging from 1 to 2 atm, equivalence ratio of the fuel air mixture in the main combustion chamber ranging from 0.4 to 1.5, and initial temperature of the main combustion chamber mixture ranging from 297 K to 500 K. Experimental data makes use of 4 pressure sensors with a recorded sampling rate up to 300 kHz, as well as high speed Schlieren imaging with a recorded frame rate up to 20,833 frame per seconds. Results shows an overall increase in ignition delay with increasing equivalence ratio. High temperature of the main chamber blend was found not to affect hot jet ignition delay considerably. Physical mixing effects, and density of the main chamber mixture have a greater effect on hot jet ignition delay.

# 1. INTRODUCTION

## 1.1 Wave Rotor Development

Pressure wave machines can be traced to 1928 when Burghard [1] patented a cell rotor device. A compressible fluid entering the cell compresses the column of fluid in the cell through a pressure wave. Several elongated cells arranged on a rotating wheel are opened and closed at a precise timing allowing the compression and discharge cycle to fully complete in one rotation of the wheel.

This pressure wave exchange idea was first developed practically by Brown Boveri Company (BBC) in Switzerland [2] with the COMPREX as a superstage of a gas turbine compressor in 1942. Later ABB developed further the technology and matured it into the Comprex supercharger used in passenger cars like Mazda 626 Capella in 1988. This was the most successful commercial implementation of the pressure wave exchanger as more than 150,000 units were in production. [3]

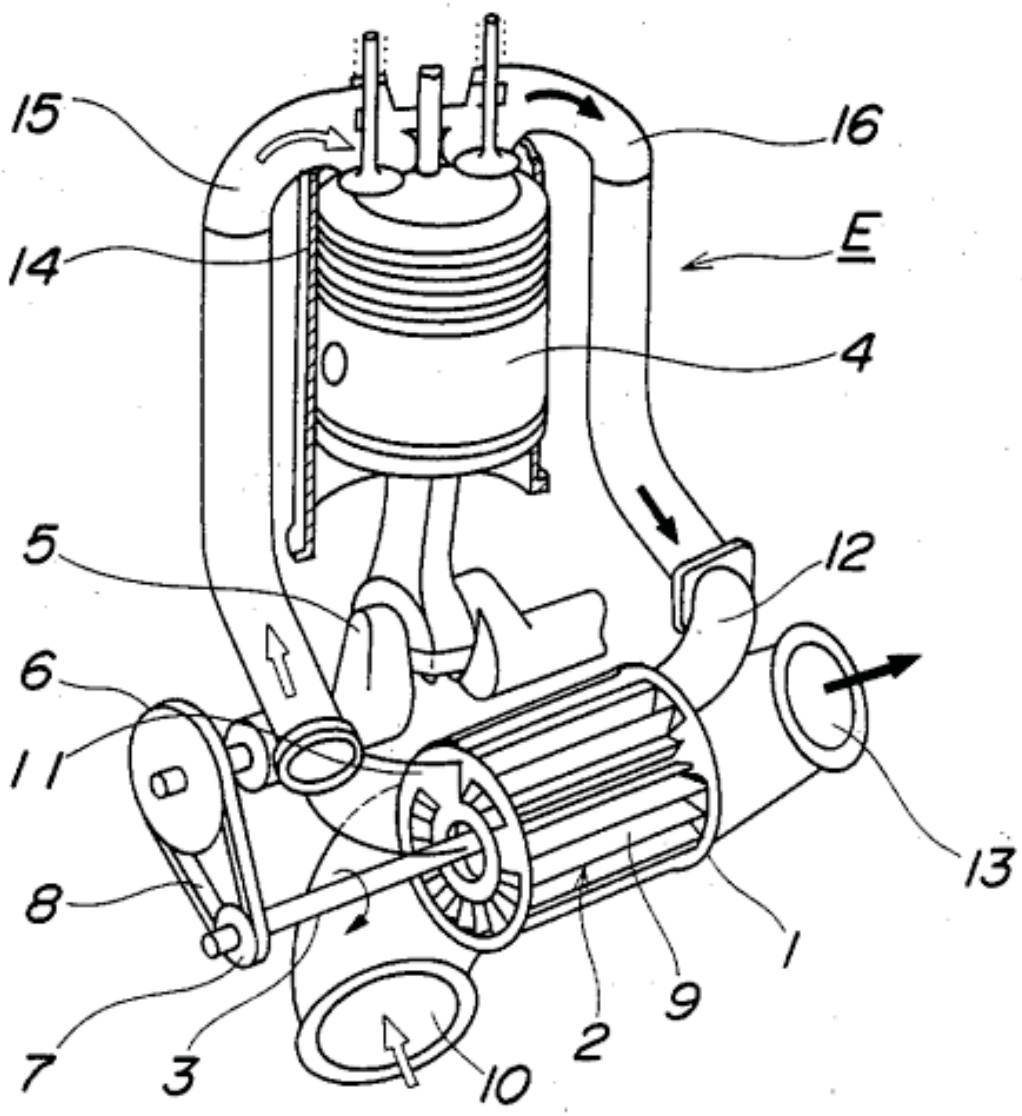


Fig. 1.1.: Comprex supercharger integrated in an internal combustion engine. [4]

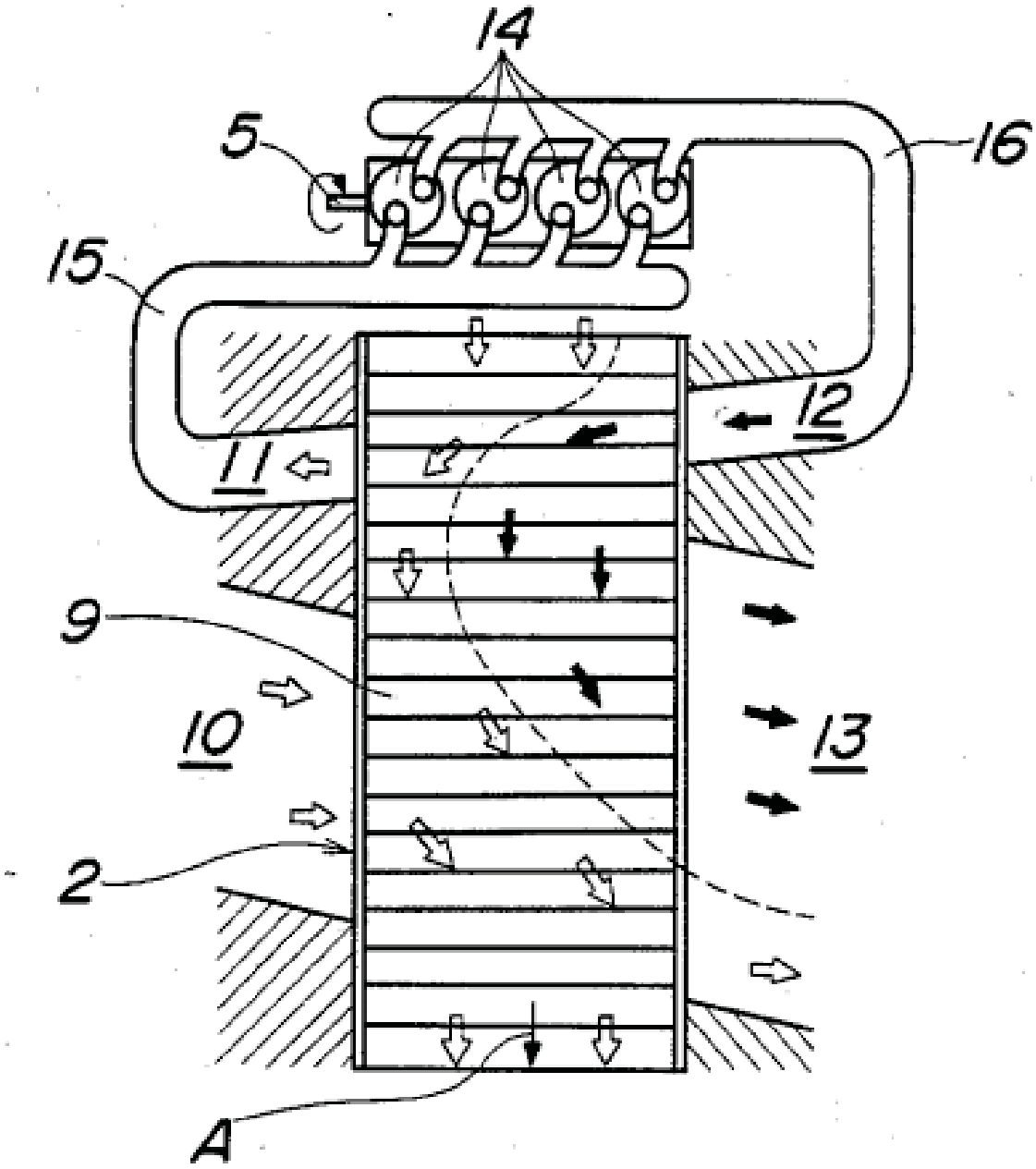


Fig. 1.2.: Comprex supercharger operation principle showing exhaust of the engine compressing the fresh intake air. [4]

In addition to internal combustion engine application, an effort was made to integrate pressure wave device into a gas turbine combustor. Claude Seippel a Swiss engineer at BBC first proposed topping a gas turbine cycle with a pressure wave supercharger [5]. ETH Zurich joined BBC in an effort to develop an integrated combustion wave rotor (ICWR) with the idea that a wave rotor cell can be filled with a mixture of air and fuel from one end, ignited with both cell end closed, and then discharging the combusted product at a higher pressure from the opposite end. [2]. ABB later took on the project and developed a one cell testing rig, in addition to a full 36 cell wave rotor combustor in 1990s. The demonstrator engine produced 17% increases in efficiency and 25 % specific power respectively.

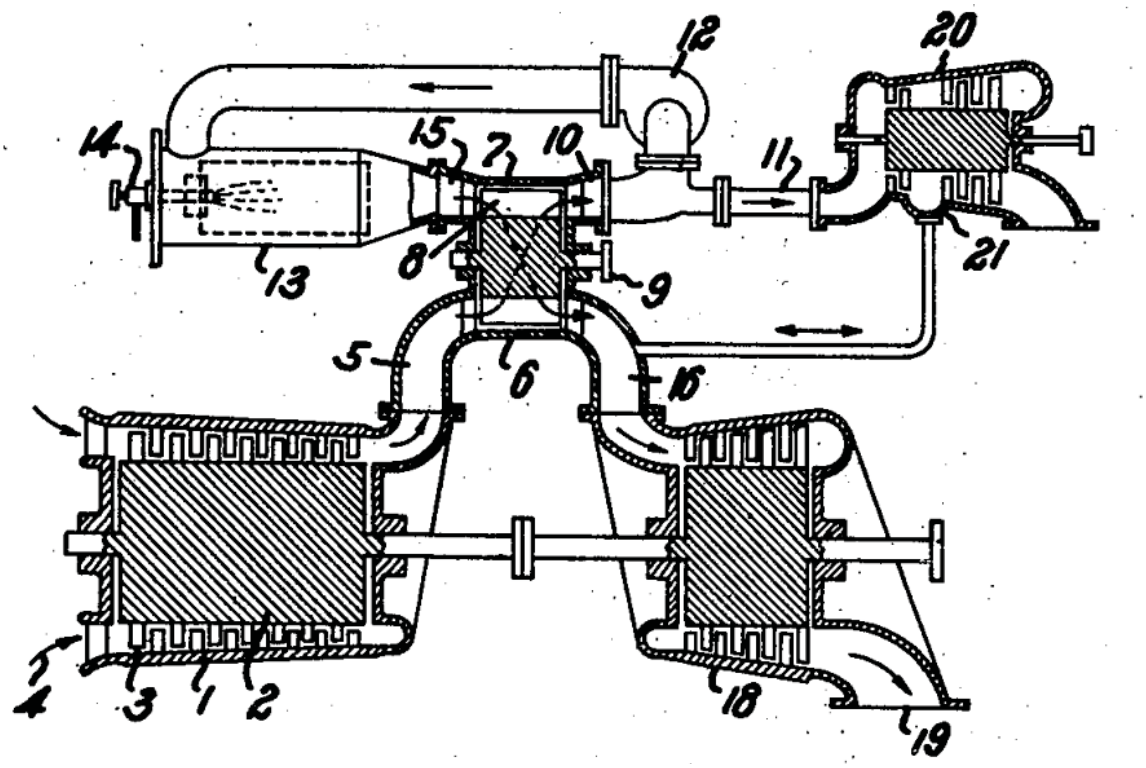


Fig. 1.3.: Claude Seippel patent showing a wave rotor topping of a gas turbine cycle. [5]

Some other places looked at wave rotor technology for different applications. The Cornell Aeronautical Laboratory in 1958 developed an impressive 2 m wave

superheater as part of a high enthalpy air supply for their hypersonic wind tunnel. Power Jets Ltd (1949-1967) in the UK looked at aircraft gas turbine applications and developed two prototype air-cycle refrigerators using wave rotors for gold mines in India and South Africa. The Pearson Rotor of the Ruston-Hornsby Turbine Company in the 1950s had successful operations over a wide speed range (3000-18000 RPM) and generated up to 26kW of power.General Electrics developed a wave rotor with internal combustion in the channels in 1958. Their efforts were stalled by rotor expansion problems and sealing issues between the rotor and the stator. Despite that GEs wave rotor had respectable performance of up to 1.3 pressure ratios. General Power Corporation (1960s-1985) sponsored by the Ford Motor Company was interested in wave rotor application in gas turbine for automotive transportation. GPC design aimed to generate shaft power by using curve blades channels. Their design was inefficient suffering from excessive blade curvature as opposed to the Pearson rotor which relied heavily on impulsive loading to achieve power output. Rolls Royce (1965-1972) began experimenting with wave rotor as a topping spool for a small helicopter engine Allison Model 250. The enhanced engine had leakages, start up, bearing durability, and other control issues. Mathematical Science Northwest Inc (1978-1985) designed a lab scale wave rotor to verify scaling laws for predicting performance of larger wave rotors and produced designs for a small turbofan engine generating 600 lb of thrust. The Office of Naval Research through the Turbopropulsion Laboratory took over the GE rig and conducted more experiments producing some shaft work at 5000 to 6000 rpm. They also developed a two dimensional code to analyze the flow in wave rotor channels.

Paxson and Nalim at NASA Glenn Research Center developed a quasi-one dimensional code to estimate a wave rotor combustor performance, and validated the code with experiment. At Rolls Royce Allison studies showed an 18-20% increase in specific power, and 15-20% increase in specific fuel consumption for an integrated wave rotor combustor in an Allison 250 turboshaft gas turbine engine. Lear et al at the University of Florida (1992-1998) developed numerical and analytical methods

to analyse flow in the wave rotor and their adjoining duct. They used their code to simulate the NASA three ports wave rotor and the GPC wave rotor. ONERA in France (1995-1999) also developed a one dimensional code and applied it to the three ports, through flow, and reverse flow wave rotor configurations.

Indiana University Purdue University (IUPUI) has been doing extensive numerical and experimental work on a single channel wave rotor test rig. IUPUI wave rotor research will be discussed in further details in the next section. Nagashima et al at the University of Tokyo developed codes to simulate flow inside a four port through flow port wave rotor. Michigan State University has been investigating micro-turbines with wave rotor topping cycles. For further details of the historical evolution of the wave rotor research refer to paper by Akbari [6].

As outlined in this section, research in constant volume wave rotor technology has been ongoing for close to a century now. The main motivation driving wave rotor combustion research efforts can be summarized as follows:

1. An improved thermodynamic efficiency due to higher pressure and temperature operation

2. A decrease in nitric oxides production due to the short residence time of combustion gas in the channel

3. Self-cooling channels due the colder fuel air mixture entering the channel each cycle

4. Wave rotor operations is continuous and steady unlike other unsteady pulse detonation devices

## 1.2 Wave Rotor Operation

The previous section reported many applications to the pressure wave technologies ranging from pressure exchanger superchargers for internal combustion engines, to wave superheater applications, to wave rotor in refrigeration cycles, to

wave rotor topping gas turbine cycle and to integrated wave rotor constant volume combustor for gas turbines. All these applications share a common operation mode of harnessing the pressure wave effects through opening and closing constant volume channels arranged on a revolving wheel. In the case of integrated constant volume combustor wave rotor (WR) for a gas turbine, the WR is replacing the constant pressure combustor typically found in gas turbines.

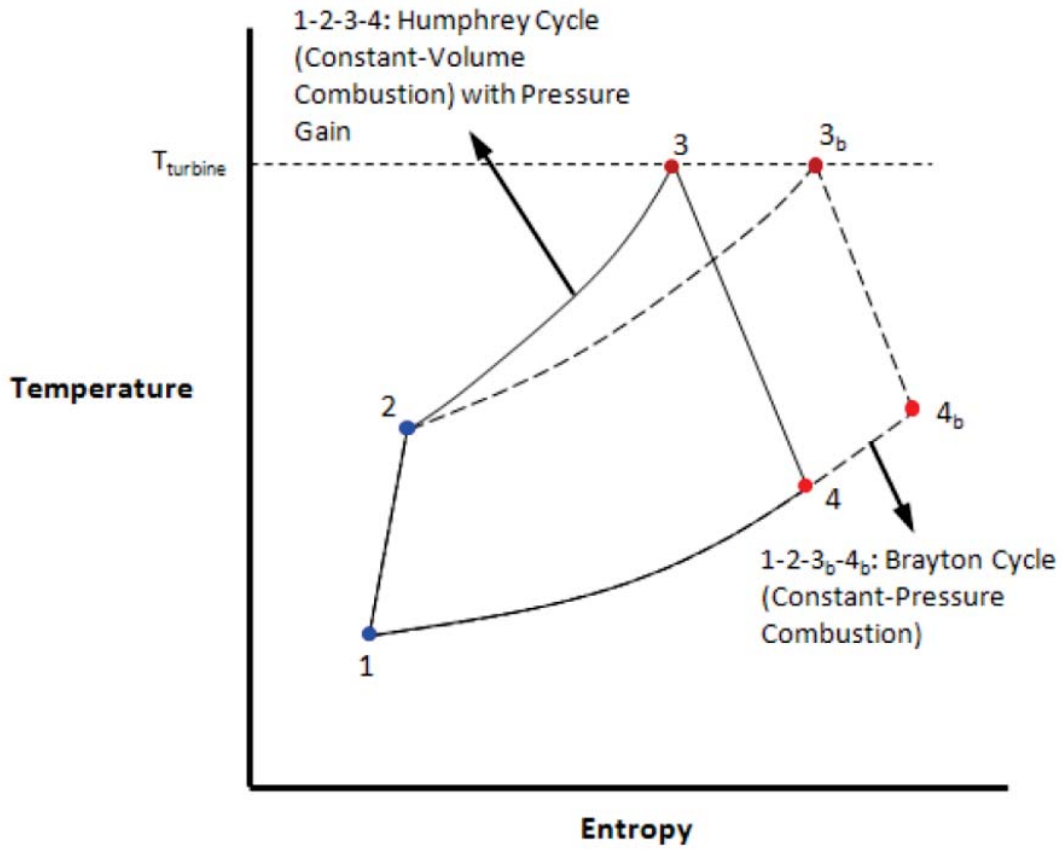


Fig. 1.4.: Brayton cycle compared to Humphrey cycle on a T-S diagram. [7]

Typical gas turbines follow the Brayton cycle process illustrated in the T-S diagram Fig. 1.4. The compressor spool increases the air pressure from 1-2, heat addition through a constant pressure combustion occurs from 2-3b and the high pressure, high temperature gas expands in the turbine section producing shaft work

from 3b-4b. In the case of a wave rotor constant volume combustor the heat addition section from 2-3 costs less entropy thus reaching the required turbine inlet temperature at point 3 at a lower entropy state compared to point 3b from the Brayton cycle. This is due to the pressure gain from the constant volume combustion process. Akbari [6] estimated that the ideal Humphrey cycle has 25 % less entropy compared to the Brayton cycle.

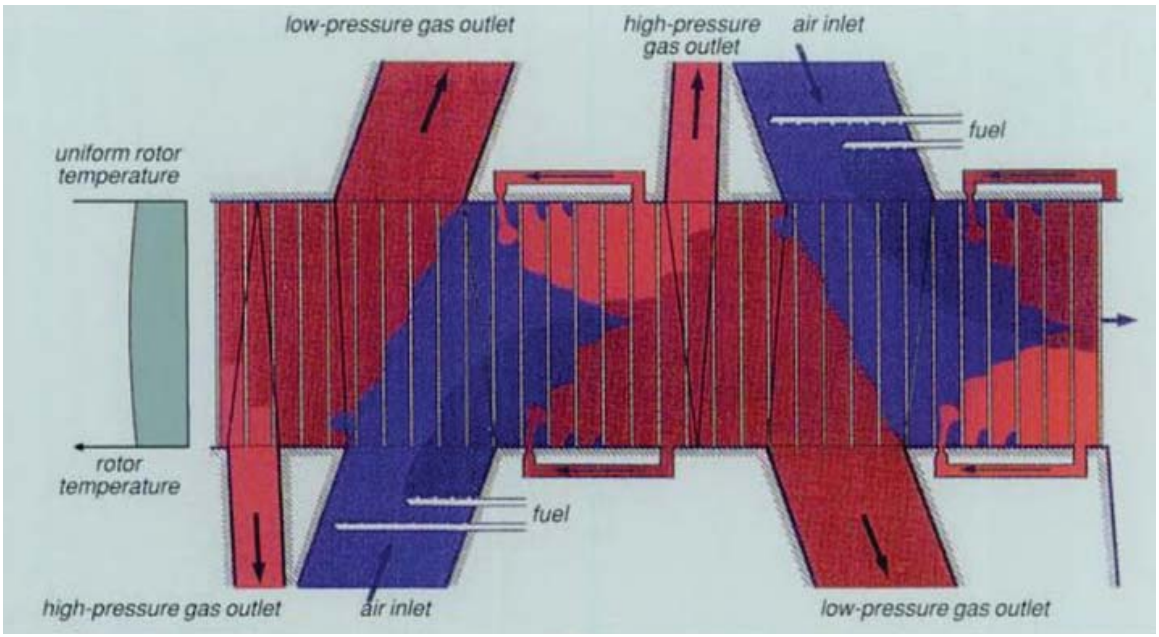


Fig. 1.5.: Integrated combustion wave rotor schematic showing one cycle of operation with hot jet ignition recirculation of the exhaust gas product. [2]

A cycle of operation of the wave rotor can be described by following Fig.1.5. The image shows a version of the integrated combustion wave rotor developed by ABB. The flat vertical lines represent the channels as they go through one full rotation in one cycle of operation. Cold air and fuel enters the channels as shown by the blue color and is ignited by a hot jet taken from the combusted product channels. Ignition occurs and consumes the fuel air mixtures and a high pressure gas is exhausted. And the cycle repeats itself, in a self-sustaining operation.

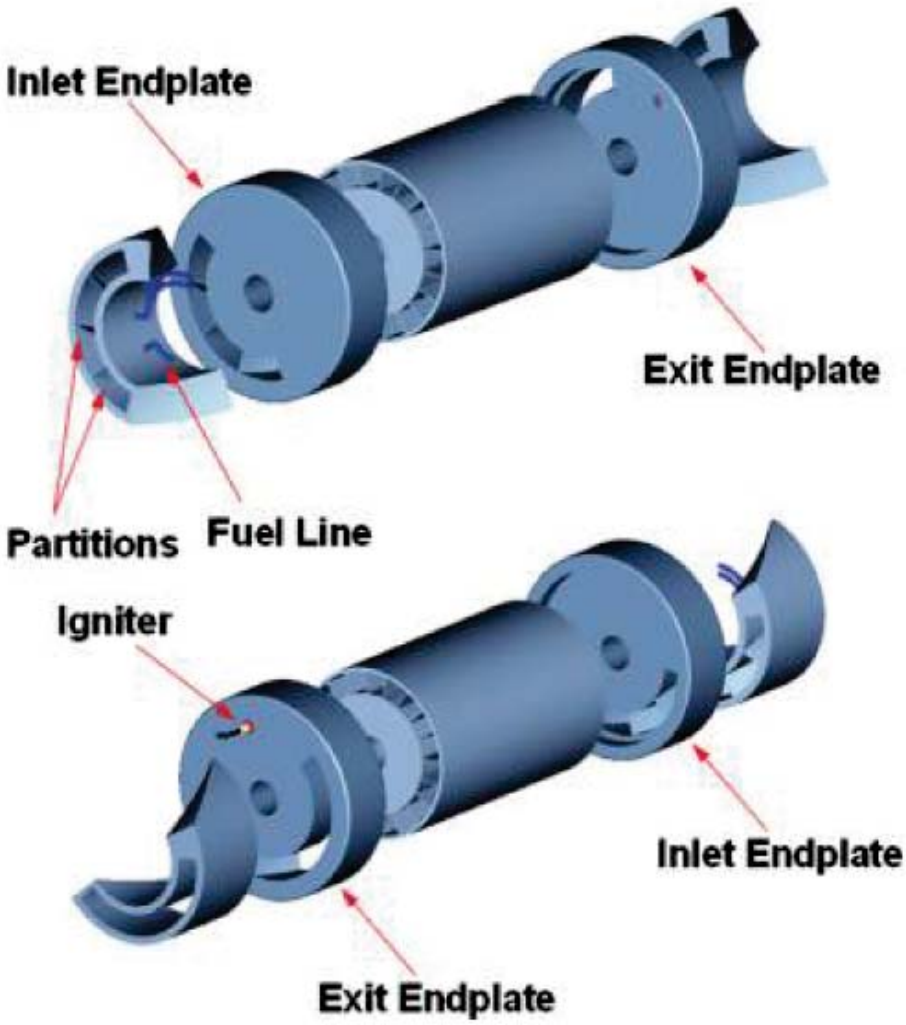


Fig. 1.6.: Wave rotor design showing rotor, seal plates, and manifolds along with the igniter. [6]

Another successful wave rotor that demonstrates a different ignition method was developed in a joint effort between Rolls Royce, Purdue University and IUPUI. Fig. 1.6 shows a drawing of a wave rotor drum, with two seal plates and an inlet and outlet manifold. The WR constant volume channels are positioned on the periphery of a drum that rotates between the fixed inlet and exit endplate. Each

channel is charged and discharged with each rotation cycle. The inlet and exit plates have partial annular slots which acts as timing valves ensuring the synchronization of the fueling process with premixed fuel and air, the combustion process and the discharge process. The premixed air-fuel entering the channel as it aligns with the inlet endplate port, causes a compression shockwave to travel in the channel before the combustion initiation. As the rotor rotation progresses, both end closes and the channel undergoes combustion after beeing ignited by a hot jet igniter. Combustion must be completed before the channel reaches the exit endplate opening. With a large number of channels, the combustion cycle operation can be achieved in a relatively steady state flow. [8].In addition an external igniter is used to ignite the channel mixtures. More details about the igniter can be found in [9]. In both these two wave rotor combustor demonstrators, hot jet ignition is being used as the primary igniter of the constant volume combustor.

The question of why a hot gas jet is predominantly used as the ignition mode for wave rotor combustors needs to be explored. Broadly speaking any combustion process consists of a fuel and an oxidizer that undergoes a chemical reaction through their exposure to a heat source. A fuel and oxidizer mixture within its flammability limit will ignite when the activation energy of the mixture chemical reaction has been reached through heat addition. In a spark ignited gasoline engine, the spark provides the heat addition. Similar to electrical sparks, using transient plasma ignition [10, 11], multiple volume distributed array of streamers can be deposited in a combustion chamber with potential ignition delay and peak pressure benefits compared to spark ignition. In a diesel engine, the fuel air mixture is compressed raising the internal mixture temperature, providing the necessary heat addition for combustion. Lasers targeting multiple points inside the constant volume chamber [12–14] are another approach for ignition which has been difficult to implement on real world combustion system. The challenge in igniting a wave rotor constant volume channel consists of the high operating speeds of up to 8000 RPM, and the elongated channel profile which means ignition needs to happen

successfully in a short window of time, and the flame needs to propagates burning all fuels before the next combustion cycle. Spark, plasma, and lasers are all local method to raise temperature at local points in the mixture. In comparison a hot jet of gas interact with the fuel/oxidizer mixture in the channel creating multiple hot spots for ignition along with mixing vortexes that considerably increase the chances of successful ignition and improves complete fuel combustion. The next section discuss hot jet ignition in constant volume combustor applications.

### 1.3 Hot Jet Ignition

Fundamental studies into ignition and the complex shock flame interaction are necessary to improve practical wave rotor design. It is important to define ignition delay and hot jet ignition both terms used frequently in this work. Ignition delay time is an important parameter used to understand the chemical reaction process and the physical mixing process leading to combustion. There is multiple definition of ignition delay depending on the experimental context. Ignition Delay (ID) in a diesel engine takes into consideration the atomization, vaporization and mixing of air fuel in addition to a chemical delay time. In other cases like shock tubes experiments ignition delay is purely a chemical ignition delay and is measured using pressure transducer as the time interval between the arrival of the primary shock wave at the end of the wall and the arrival of the ignition spike. In a wave rotor, ignition is achieved through a hot jet traversing the channel opening from top to bottom. The traversing transient jet penetrating the channel causes a complex turbulent vortex, a turbulent mixing shear layer, and transverse pressure waves which all impact ignition. It follows that ignition delay is composed of a physical delay consisting of the hot jet mixing with the stagnant fuel air mixtures generating vortexes and turbulence, as well as the chemical delay time consisting of reaction kinetics rates to initiate ignition. This report defines ignition delay as the time interval between the rupture of the diaphragm separating the pre-chamber from the

main chamber and the ignition pressure spike as illustrated in Fig. 1.8. The rupture of the diaphragm in this experiment is measured by calculating the shock speed and deducing its initial start time (assuming a constant shock speed) by knowing its distance from a pressure sensor. The ignition moment is located visually using Schlieren imaging techniques. Fig. 1.7 shows an illustration of the ignition process from the pre-chamber combustion, diaphragm rupture and hot jet penetrating into the main chamber.

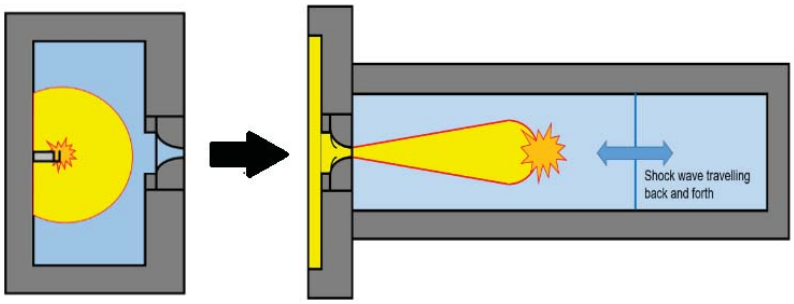


Fig. 1.7.: Illustration showing pre-chamber ignition, diaphragm rupture and hot jet penetrating in the main chamber before ignition. Adapted from Paik [15]

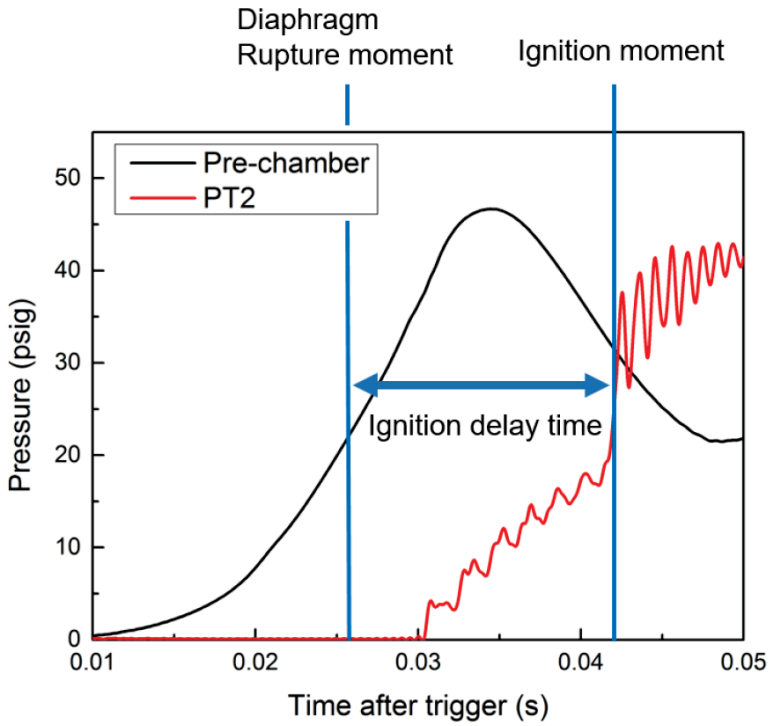


Fig. 1.8.: Ignition Delay definition as per Paik. [15]

With the ignition delay definition established it is important to understand the parameters affecting ignition delay in the experiment settings. Hot jet ignition is applied in internal combustion engines, pulse detonation engines, and wave rotor combustors [16]. Pre-chamber-initiated hot jet ignition has been utilized as early as 1918 with Ricardo's Dolphin internal combustion engines. [17] The main advantage of turbulent jet ignition is the production of distributed multiple ignition sites which leads to a faster burn rate, aided by the interaction of flames with strong pressure waves generated by the jet introduction and by the initial volume of ignition. Compared to spark plug ignition, turbulent jet ignition is a more effective ignition method due to creation of chemically reactive radicals and fast turbulent mixing of the jet. [16] This is particularly important in wave rotor application with operation speed generally much higher than internal-combustion piston engines.

Moreover hot jet products contain active radicals that can overcome the slow combustion velocity in lean mixtures. [18]. In the case of hot inert gas ignition into

hydrogen oxygen mixtures, Elhsnawi [19] reported that ignition occurs at the circumference of the jet. While Sadanandan [20] reported ignition occurs at the tip of jet. Iglesias [21] found that ignition is more dependent on the diffusivity of the reactant rather than the jet Reynolds number. Bilgin [22] developed a test rig consisting of a rotating pre-chamber with a fixed long aspect ratio main chamber. He proposed a correlation between ignition delay and the Damkohler number (ratio of flow time scale and chemical time scale). In summary, radicals in the hot jet, jet temperature, jet Reynolds number and jet diffusivity, all play a role in determining ignition in a constant volume combustor. This work is focused on determining if initial air fuel mixture temperature plays a role in ignition delay.

The Combustion and Propulsion Research Lab (CPRL) at IUPUI took ownership of the ignition wave rotor rig of Bilgin from the University of Washington, and continued ignition delay researched after performing several upgrades. Perrera [7] used flame luminosity images to investigate ignition delay in a constant-volume combustor supplied with a transient jet of hot gas from a stationary pre-chamber. Chinnathambi [23] investigated ignition in a constant-volume combustor by a puff of hot gas injected by a traversing jet supplied from a rotating pre-chamber. Last, Paik [15] used flame luminosity images and high-speed pressure sensors for more accurate ignition delay measurements for methane/hydrogen mixtures.

## 1.4 Scope Of Research

The present research main goals in order of priority are to:

1. Build a new optically accessible combustion chamber with minimal leakage (less than 1 mpsig/s)
2. Integrate a heater for high temperature experiments (up to 500 K)
3. Develop a fast fuel delivery system (less than 15s)

4. Perform high temperature ignition delay experiments on methane, and methane/hydrogen blends

Initial pressure in the pre-chamber was increased from 1 atm to 1.5 atm and 2 atm. Operating test points of equivalence ratio included 0.4, 0.7, 1, and 1.5. Three temperatures test points used are 297K, 400K, and 500K. The wide range of operation provides data for further development of an ignition delay model in the future. Pure hydrogen tests performed are included in the research but not analyzed due to their small ignition delay time, which can not be captured accurately in the existing rig set up. Detailed Schlieren imaging of ignition and combustion is used to analyze the combustion process. Pressure profiles of ignition are analyzed and correlated to Schlieren images. Ignition delay data is reported for methane, and methane/hydrogen mixtures. All the research defined goals mentioned above were completed in this report. Further studies would include a more detailed analysis of the generated experimental data, as this author established a preliminary analysis only. The present generated results can be used as guidelines for design of hot jet igniters for constant volume combustors.

# 2. EXPERIMENTAL METHODS AND PROCEDURES

The experimental apparatus presented in this report was originally built by Bilgin [22] and was later transferred to CPRL. Each group of graduate researchers made modifications and improvements to current system. A total of three combustion chambers have been built so far at CPRL. Each one of the previous chambers had limitations that motivated this author to build the 3rd generation combustion chamber. Previous chambers had leakages, glass cracking issues, or were not completely optically accessible. A new combustion chamber has been built to address those issues, in addition to installing an electric air heater system to have the capability to do high temperature experiments. In order to perform repeatable high temperature experiment, quick fueling of the chamber was needed, so automatic fueling using a mass flow controller was implemented. In addition, previous combustion chambers were manually ignited by pressing repetitively on an ignition button which was not repeatable so the 3rd generation combustion chamber implemented computer controlled ignition. Moreover a new mixing station was built to have a tank storage of fuel mixture ready to be delivered to the mass flow controller and the pre-chamber.

It should be noted that current combustion design is inspired from a single channel of a complete wave rotor. The experiments described in this report are an scaled version of a combustion event happening in each of the wave rotor channels.

## 2.1 Combustion Chamber

### 2.1.1 Improvements

A new combustion chamber has been designed and built for this project. The combustion chamber is made out of stainless steel 304 and has two side quartz windows for optical access. It also has four pressure transducers ports and two ports for preheating air inlet and outlet. The chamber sits on an X and Y positioning table controlled by two stepper motors driving linear actuators. The whole assembly is sitting on a table made of aluminum extrusion with adjustable height. Compared to the previous generation of chambers at CPRL, the current chamber has at least 50 % less parts (4 compared to more than 8) and is made of stainless steel instead of aluminum. These features help achieve two primary design goals: minimize leakage rate under pressure and under vacuum condition, and minimize chamber heat loss. A secondary design goal was to insure long term survival of the quartz glass which is subjected to repeated heating and cooling cycle by the combustion chamber pre-heater as well as repeated dismantling operation for residue cleaning purposes. In the past generation chambers these two issues have damaged the quartz glass repeatedly incurring costs to CPRL. A simple solution has been found by holding the face of the glass with O-rings acting as a cushion with the metal while leaving 0.005" as clearance between the glass edges and its seat in the metal block. This solution has proven to be adequate as the chamber has been subjected to an air inlet temperature of 1000 F, with a temperature gradient along its length without any damage. As for the repeated dismantling of the chamber for cleaning purposes, the new design made it easy by minimizing the number of parts to 4, and the number of screws to 12 including the face seal plate.

### 2.1.2 Description

The main combustion chamber is sitting on an X and Y positioning table made by Velmex (MN10-0100-M02-13) which features a 2 mm/revolution lead screw linear slide combined with a stepper motor capable of 400 steps per revolution. This yields a linear resolution of 0.0005 mm. Fig. 2.1 and 2.2 show the combustion chamber and its auxiliary systems.


Fig. 2.1.: Combustion chamber (1) sitting on XY positioning table (3) while facing the pre-chamber (2).A C-clamp (6) holds it firmly in place. Also shown are air inlet (6) and outlet (7) for main chamber heating and mass flow controller (5) for fuel delivery and a High speed camera (4).

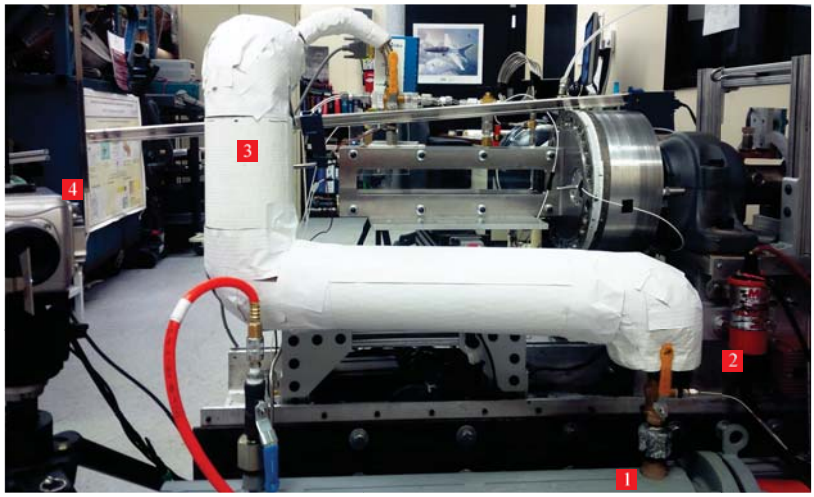


Fig. 2.2.: Back view of the combustion chamber showing the heater (1), ignition coil (2), insulated piping (3) and the high speed camera alongside the knife edge for Schlieren imaging (4).

The schematic in Fig.2.3 shows the pre-chamber on the left with a nozzle and an aluminum diaphragm. The pre-chamber has a cylindrical internal volume which houses the spark plug at its center, and two openings of 1.58" on diametrically opposed side holding the nozzle and pressure transducer. The 1010 aluminum diaphragm has a thickness of 0.003" and is scored in a + shape to form the weak point for controlled burst. A new converging nozzle has been machined and used throughout this experiment with the following dimensions which refers to the diaphragm as a starting measuring point moving towards the nozzle throat; exit throat diameter of 0.270", 10 ° taper and a length of 1" between diaphragm and nozzle exit. This gives the nozzle an $L/D$ ratio of 3.73. More details about the nozzle dimensions can be found in the appendix. The main reason behind machining a new nozzle and not using the nozzle of Paik [15] is that the nozzle face needed to sit flush with the pre-chamber face. A new pre-chamber face insert made of A2 tool steel was machined and surface finished to 16 microns average roughness in order to provide a smooth sealing surface contact while rotating. The design of the main chamber seal for the rotating case is not addressed in this report, however the main

idea was to have a hard smooth surface made out of A2 tool steel mated with an oil filled bronze seal. The bronze seal will house an O-ring at 10-20% surface protrusion that acts as a cushion while also having bronze to steel metal contact. The whole assembly would be clamped to develop the necessary sealing pressure.

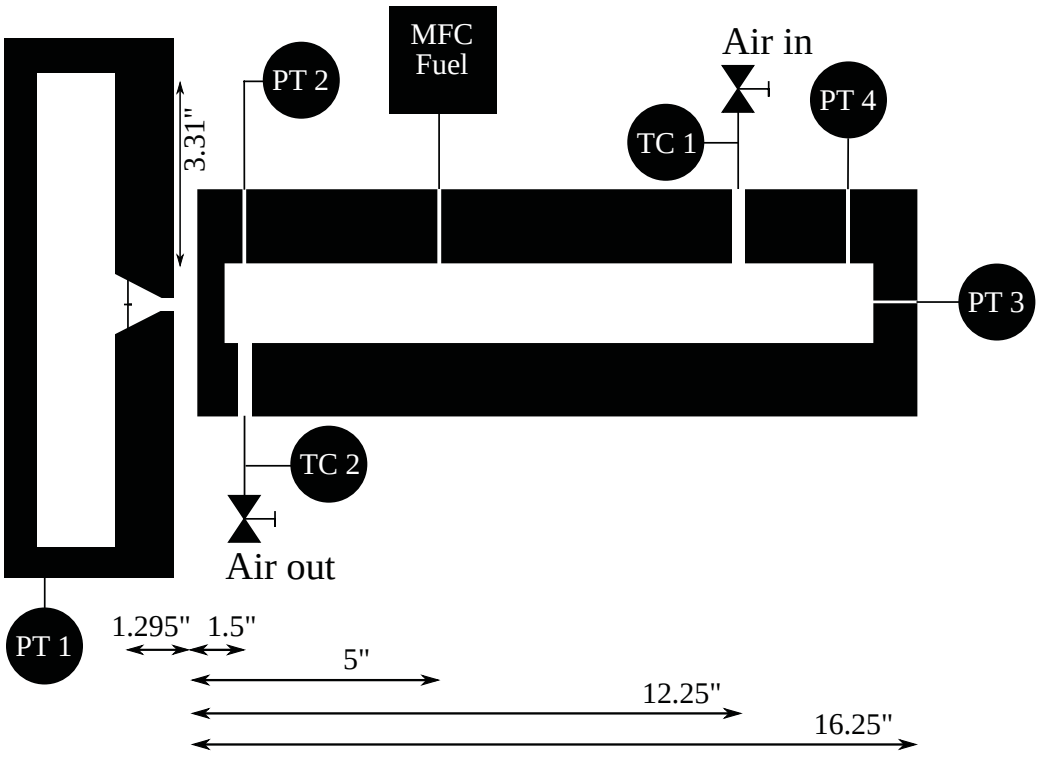


Fig. 2.3.: Schematic of pre-chamber and main chamber with instrumentation

In Fig.2.3, the main combustion chamber on the right has a length of 16.5" including the seal plate interface, a width of 4.425" and a height of 4.990". The optically accessible window consists of two identical clear fused quartz (TSC-3) rectangular blocks with dimensions of 15" × 2.77" × 1" made by Technical Glass Products. The optical observation window area is 14" × 1.85".The glass windows are sandwiched between two O-rings facing the middle block and the external block providing an adequate cushioning of the glass against the metal. The seal plate has

two O-rings one on the front side facing the pre-chamber and one on the back side facing the main chamber thus effectively sealing any leakages from both sides. Seal plate thickness was minimized to 0.25" reducing the covered portion of the jet that cannot be seen to 1.25". See figure (2.4) for details.

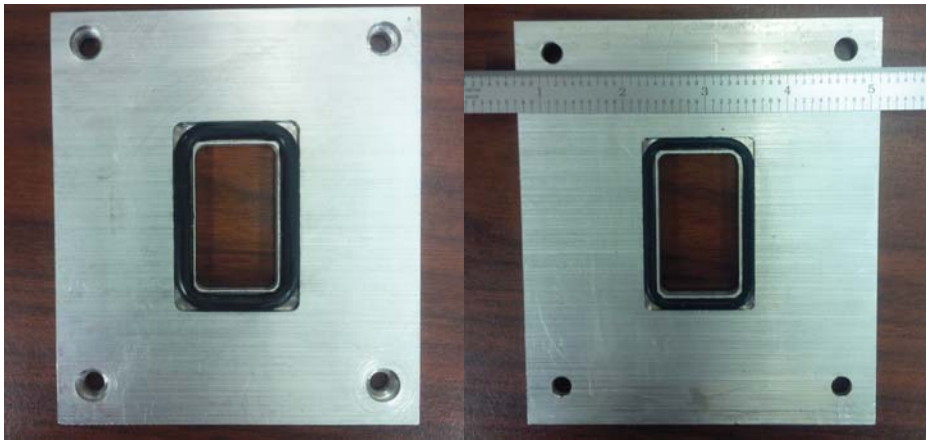

Fig. 2.4.: Seal plate showing the front O-ring on the left, and the back O-ring on the right.

The main combustion chamber was designed to have 3 pressure transducer ports, PT 2, PT 3 and PT 4. It has one port for fueling, and two ports used for air preheating and purging purposes as shown in Fig.2.3. In this report, PT 2 and PT 3 are known as "Near" and "Far" respectively, as a relation to the pre-chamber nozzle (near and far from the discharge nozzle). Its dimensions are designed to be comparable to a wave rotor channel with a high aspect ratio. With a cross sectional area of 1.43" $\times$ 1.84" and a length of 14" for the observable section, the aspect ratio of the channel is $AR = 0.77$. And the length to hydraulic diameter ratio is $L/D_H$= 8.69. The total internal combustion volume of the main chamber including the ports and open instrumentation tubing is estimated to be 43.1 in$^3$. The total combustion volume of the pre-chamber is estimated to be 49.3 in$^3$. This yields a ratio of $V_{pre}/V_{main} = 1.14$. Combustion chamber blocks are separated by an Aramide/Buna-N gasket which is rated up to 1,400 psig and 750 °F. Two gasket are

cut to size and provide the primary sealing surface between the three chamber blocks.

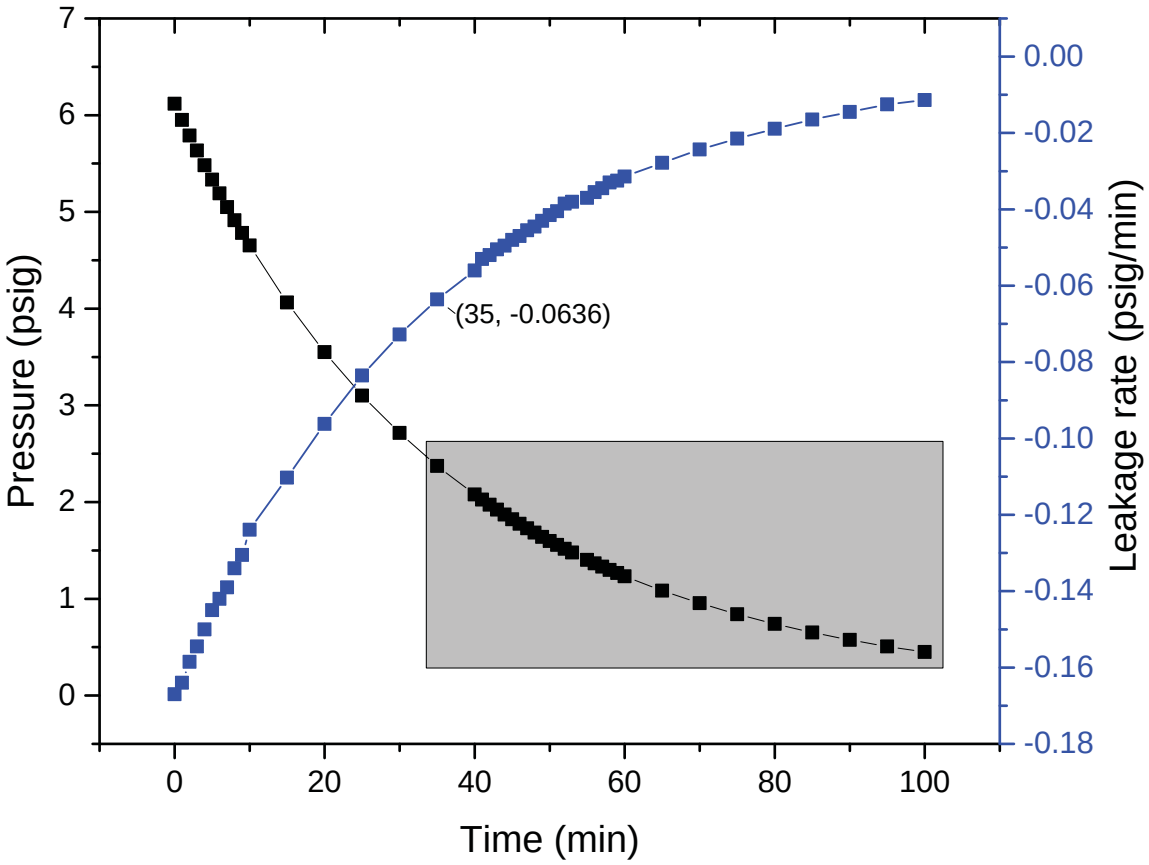


Fig. 2.5.: Exponential decay of pressurized main chamber with pure methane in 100 min.

Testing of the combustion chamber for leakage was done with methane by compressing the chamber to approximately 6 psig and recording the pressure log with time. There is no need to go to a higher pressure since leakage rate is critical to quantify only for the fueling operation which will not exceed a 6 psig of fuel added to the main chamber volume. Fig.2.5 shows an exponential decay of pressure with time which is expected. Leakage rate for the operational region in grey is a maximum of 0.0636 psig/min, which is equivalent to 0.00106 psig/sec. The fueling operation takes 5 to 15s, assuming a 20s which is the maximum time between

closing the valve, fueling and initiation of ignition we conclude that the maximum leakage in 20s would be 0.0212 psig which is negligible. Also in 20s we estimate that adequate mixing would have occurred between fuel and air that even if a leakage occurs, it would be the homogeneous mixture leakage which would not alter the targeted equivalence ratio.

### 2.1.3 Cleaning

The combustion chamber can be easily opened for cleaning purposes. The author had to clean many times the stained glass combustion products. Fig.2.6 shows the dismantled combustion chamber as well as the Aramid/Buna seal and O-ring. A brief procedure is presented here:

1. Open up the 4 screws holding the seal plate.
2. Open in order the 8 bolts holding the chamber together.
3. Carefully remove one side making sure not to detach the gasket. Put the side on the table and clean the glass with alcohol.
4. Remove the other side and put it on the table for cleaning.
5. Use a blade knife carefully to remove any gluey spots. Do not remove the glass windows unless absolutely necessary.
6. Make sure to not pinch the O-rings and gasket while putting the bolts on and tightening.
7. Torque the bolts in opposite sides sequentially to 250 in-pounds

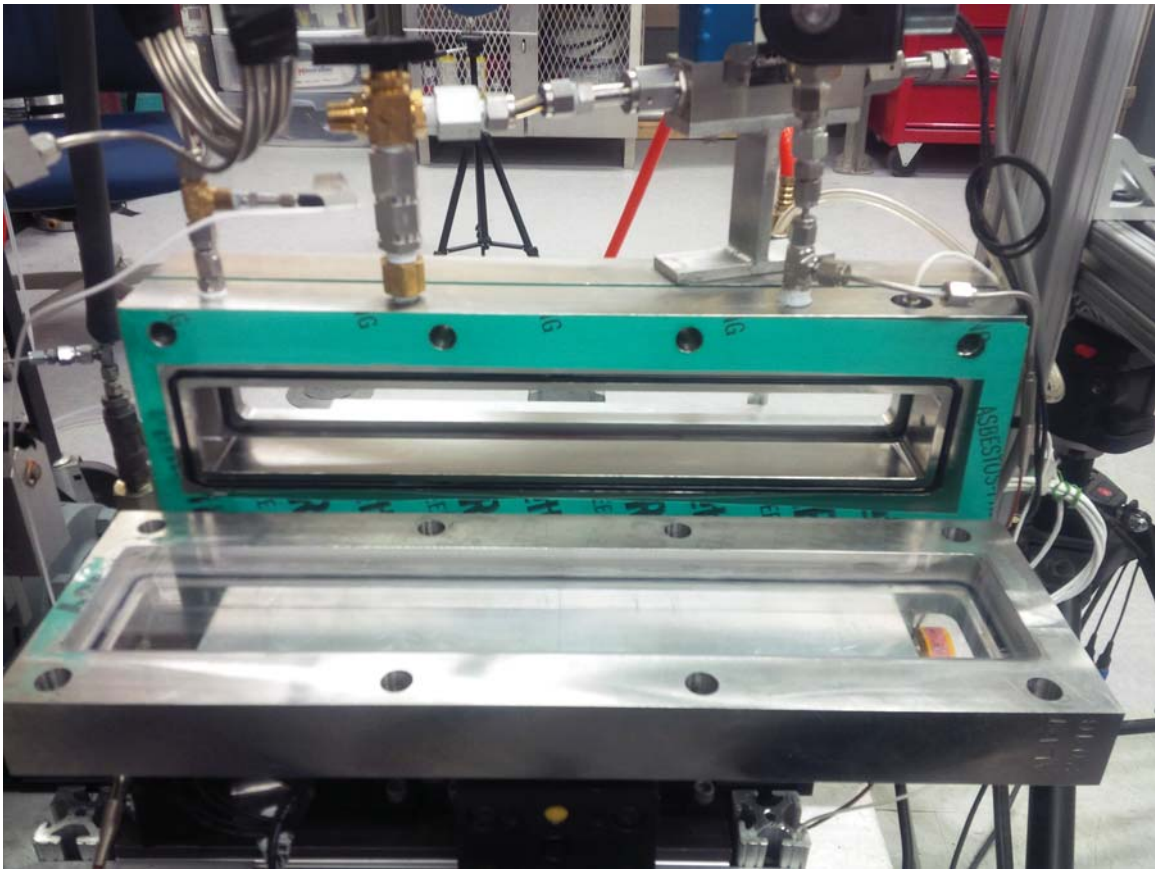

Fig. 2.6.: Chamber dismantled on one side for cleaning the glass from combustion residues.

## 2.2 Heating System

In order to heat the fuel air mixture before ignition, a two approaches have been considered. Heating the chamber metal blocks with electric cartridges, and heating with an electric circulation heater. Paik [15] experimented with electric cartridges on the 2nd generation combustion chamber made of Aluminum alloy but found out that the high conductivity of aluminum contributes to a high heat loss rate and subsequently could not raise the air fuel mixture to the desired temperatures. The chamber was made in stainless steel 304 in an effort to take advantage of its lower thermal conductivity of 16.2 W/m-K compared to 167

W/m-K for Aluminum 6061 at room temperatures. A circulation heater model CFMN720J12S made by Watlow with 2.5 kW input power, rated for 3 phase voltage at 240 V was selected to heat the air going into the main chamber. However the current electrical supply installation in CPRL can supply an average of 208 V 3 phase voltage. This de-rated the heater power to 1.875 kW, negatively affecting the heating time of the system. The maximum temperature of the heating element is 1250 °F. A thermocouple sheath at the center of the heater has to be always monitored to stay well below that temperature because the heating element temperature is always higher than the air temperature measured by the thermocouple. The recommended operating maximum temperature is 1000 °F.

The heater is controlled by a Novus N1020 temperature controller which can perform an auto-adaptive PID control for improving system performance. The PID controller actuates the coil of a 3 phase E-Safe II Hybrid Power Switch ES23-2HV-0000 made by Watlow. This power switch has a long life because it is a combination of a solid state and an electromechanical relay well suited for resistive heating applications. [24, 25] The heater is fed compressed air regulated by a pressure filter from Norgreen. Different setting pressures have been tried to optimize the mass flow rate and the maximum heating air temperature that can be achieved. The PID controller has been given a set temperature of 950 °F throughout this experiment. The output of the heater is a 1/2" stainless steel 304 schedule 40 pipe 36" long, insulated by a 2" fiberglass insulation. At the end of the pipe is an 18" flexible braided metal hose which is rated up to 1200 °F temperature. This flexible hose allows the chamber to move on the XY positioning table while still connected to the piping of hot air.

The mass flow rate of air into the heater is determined by the upstream pressure set by the regulator. In order to find the optimum operating conditions of the heater a test have been set up where temperature is recorded at the heater outlet and, at the inlet, front (near nozzle) and outlet of the main chamber while

varying the upstream cold air pressure supplied to the heater. The thermocouples configuration is shown in Fig.2.7.

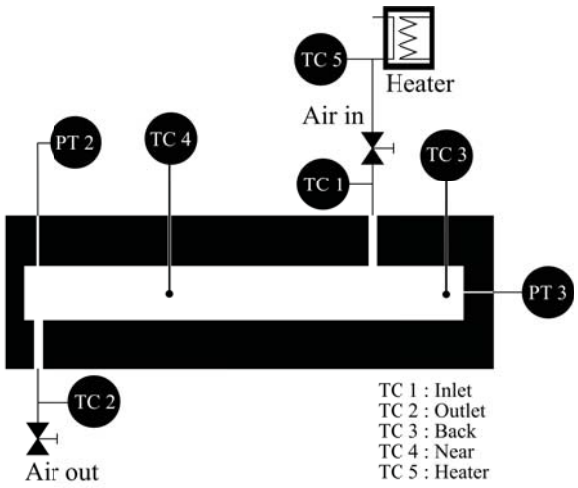


Fig. 2.7.: Thermocouple configuration for heater test at different upstream pressure. Note TC4-Near and TC-3 Back are positioned in the middle of the chamber height wise.

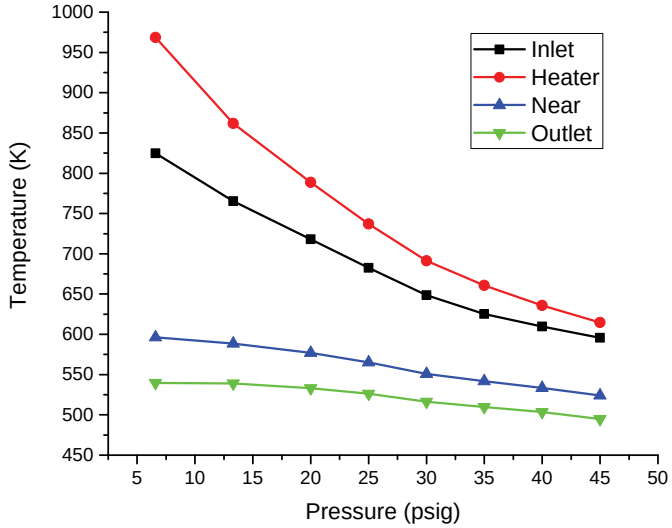


Fig. 2.8.: Steady state temperatures variation with upstream pressure variation into the heater.

Each recording point has been made after 10 min of steady state operations. The graph in Fig.2.8 shows an inverse dependence between pressure and temperature. As the pressure increases, the mass flow rate increases, and the heater constant power output is divided onto a bigger quantity of air, which drops the overall temperature. The 20 psig upstream pressure was selected as the operating point because the front temperature 576 K is close enough to target temperatures of the experiment tests within a flexible margin. An inconvenience to the lower mass flow rate is an increase in the time to heat the metal blocks to sustain the target temperature. A more thorough analysis could have been done to optimize the upstream pressure with the time it takes to heat the chamber to the target temperature.

However, the current settings were acceptable to this author, after one hour of heating the system (heater, piping, and chamber) the target temperature is attained and it takes about 10 min of heating after each testing set up ( cleaning and replacing diaphragm) to reach the target temperature of 500K, and about 5 min for

lower target temperatures as 400K. It should be noted that the set up time plays a big part in the time values given before. The longer the set up time is, the cooler the chamber will get and the longer the heating time will be.

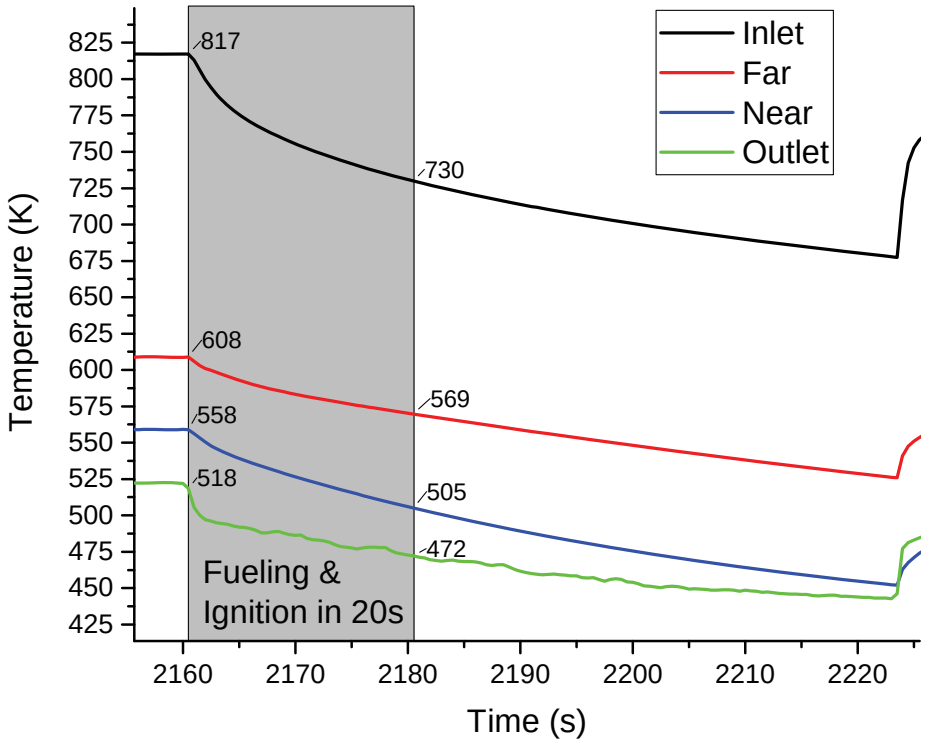


Fig. 2.9.: Temperature decay due to heat loss after closing the hot air inlet and outlet valve of the chamber

Two elevated temperatures have been used as test points in the experiments, 400 K and 500 K. Since no active temperature measurement is being made inside the combustion chamber during the experiment, a test has been done by using 4 thermocouples to map the temperature distribution from inlet, back, front, and outlet of the main combustion chamber. Fig.2.7 shows the placement of the thermocouples. The goal of this test is to determine a suitable outlet temperature that will be used as an indicator that the main chamber air temperature inside has

reached the desired 500K average value. A plot of the temperature decay after the outlet temperature reaches 525 K is shown in Fig.2.9. The time it takes from closing the inlet and outlet valve to launching the experiment varies from 12 to 20s. The graph shows a 20s range (colored in gray) after closing the valves and the temperatures changes before and after. Initially hot air enters the main chamber at 817 K where it is cooled abruptly by the contact with the cold metal and the sudden expansion. A temperature of 608 K is measured at the far of the chamber while the near temperature is 558 K. Finally the air exit the chamber at 518 K.

Two important observations can be made from the temperature decay profile:

1. There is 50 K difference between the near and the far of the chamber. This difference grows to 64 K after 20s.

2. After 20s, the near temperature drops to 505 K which is close the target temperature of 500K.

The 50 K difference between near and far of the chamber leads to inaccuracy in estimating the mass of air inside the chamber, and thus the equivalence ratio under study. An error analysis in another section will give more details about the percentage error. However ignition happens in the front region where the temperature is measured by the near thermocouple. This temperature is reported as the base main chamber temperature. Since this study is primarily interested in studying ignition delay, the important criteria is to record temperature around the ignition region. This criteria is satisfied by the near thermocouple measurement.

A similar test has been conducted for the 400K base chamber temperature, which showed that an outlet temperature of 425 K corresponds to an average temperature of 400K for the near location after 20s. A summary of the values can be seen in Table 2.1.

It is important to note that these values are determined at a fixed heating profile with a fixed mass flow rate through the system. Changing the mass flow rate

Table 2.1: Summary of outlet temperatures corresponding to a main chamber base test temperature after 20s

| $T_{base}$(K) | $T_{outlet}$(K) |
|---|---|
| 400 | 425 |
| 500 | 525 |

would change the temperature differences in the system and the number indicated in the table would not be valid anymore.

## 2.3 Ignition And Control System

The experiment procedure can be summarized by the following sequential steps:

1. Filling the pre-chamber manually
2. Filling the main chamber
3. Initiating ignition of the spark plug
4. Recording simultaneously visual camera images and pressure data.

From a control system perspective three essential improvements were implemented in this project on the procedure explained above in order to perform elevated temperature experiments. The filling of the main chamber used to be done with the partial pressure method by manually opening a needle valve which takes 1 to 2 min to be completed. This procedure would not be feasible with a chamber at high temperature because of heat loss. The fastest method would be to automate the filling of fuel and the heating of the chamber using a mass flow controller and solenoid valves respectively.

The second improvement solved the unreliable push button spark ignition method. Pushing a manual butting is not repeatable and consistent. Previous

experiments had multiple firing issue due to the spark not responding to the low and inconsistent frequency of manually pushing a button. The new solution initiates the sparks by sending a predetermined pulse to the electronic spark ignition module.

The last improvement eliminated the high voltage loop between the sensitive electronics (camera, and DAQ) and the high voltage ignition coil. This caused problems in the past that damaged the camera synchronization circuit. The new solution for the synchronization circuit for the camera and pressure sensors consists of triggering directly from the 5V signal going from the DAQ to the spark plug ignition module instead of the approximately 500 V which is delivered from the ignition module to the ignition coil. At first glance this solution seems to suffer from an electrical delay since the trigger is taken from the DAQ and not from the ignition coil. But tests performed in section 2.3.2 shows that any spark delay is dependent on the frequency of the pulse sent to the ignition spark plug, and thus for this experiment purpose the electrical signal transmission delay between DAQ and spark can be considered infinitely fast.

### 2.3.1 Control Box

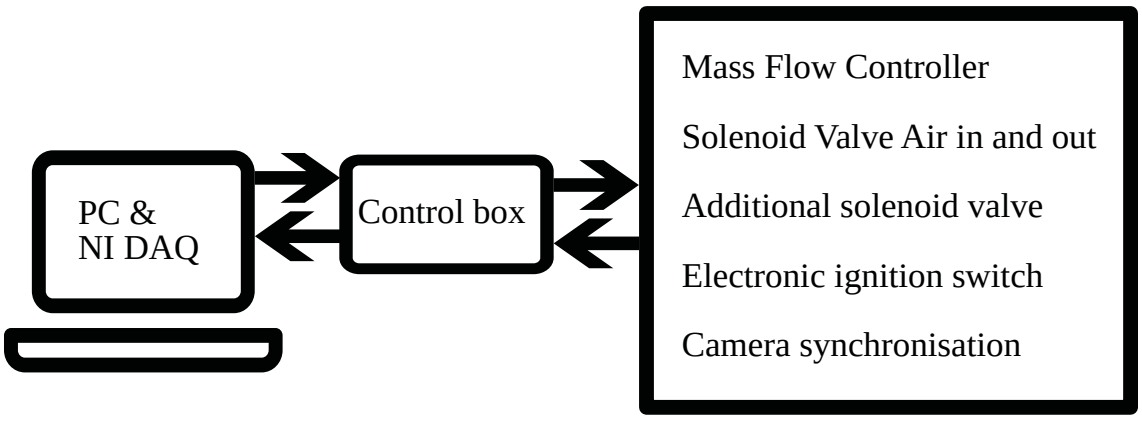


Fig. 2.10.: Schematic of actuators controlled by the control box and the DAQ system

In order to incorporate all the new feature a control box has been built to link the DAQ and computer to the control actuators. Fig.2.10 shows a general view of the system and its elements. The control box elements are soldered on a perforated board with 10 positions plug in connectors on each side one for the link to the DAQ and another for the link to the solenoid valves, ignition switch, and camera trigger. In addition a DB15 plug is on the front side to connect to the mass flow controller. A simple on/off switch turns off the power to the mass flow controller.

Three simple circuits make up the control box inner working shown in Fig.2.11. Two of them are composed of opto-isolator TPL222A which is being driven by a 5V digital output signal from the DAQ after a voltage divider steps it down to 1.2V. The first opto-isolator is used to control a solenoid valve, while the second one is used to deliver the spark trigger signal. The 3rd circuit is the trigger circuit made up from a simple NPN 2222A transistor in a common emitter configuration. The resistor at the base of the transistor is tied to the digital output pulse driving the spark plug opto-isolator. On the collector side the 5V voltage from the camera internal trigger circuit is connected. A resistor is used at the emitter to limit the current once the circuit is active. As soon as the digital output pulse is initiated by the DAQ the base current will rise, activating the transistor which will act as a switch that will lower the camera internal trigger voltage from 5V to below 2V going through the emitter resistor an through the ground. This will trigger the camera circuit. At the same time the DAQ internal trigger digital input APFI0 is wired in parallel to the camera voltage, and a rising edge can be detected through Labview software that will trigger the pressure transducer.

The control box also houses the internal connection from the mass flow controller to the DAQ through a DB15 plug. To control the mass flow controller an analog output signal from 0-5V is needed. The flow signal from the MFC is being read as an analog input signal. The mass flow controller is powered by 15V power adapter that is being delivered through the control box. The mass flow controller internal settings can be altered to change the gas selection through a network cable

RJ45 connection. In order to do that the IP address of the computer should be changed to match the MFC IP address with exception to the last number.

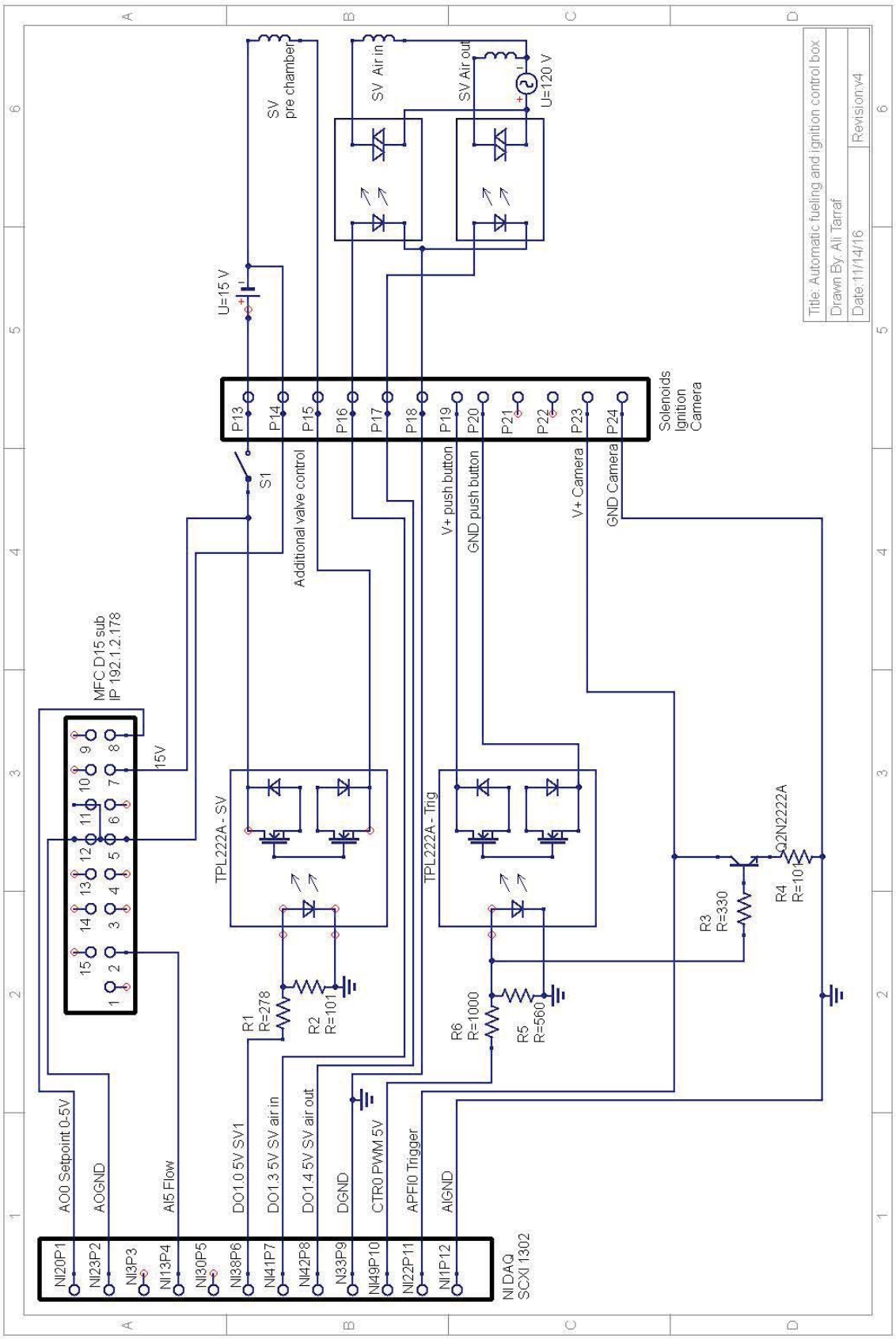


Fig. 2.11.: Control box circuit diagram

The main chamber air heating inlet and outlet 120 VAC solenoid valve are controlled individually by two isolated DC actuated electromechanical relay made by PowerSwitch Tail. Each unit responds to a 5V digital output relayed from the DAQ through the control box. This was found to be a safe and effective way to control line voltage AC solenoid valves.

### 2.3.2 Spark Plug Timing

It is important to note that a hardware generated counter pulse is used to create accurate pulsed square wave driving the ignition spark switch module. The question then arise to what is the best square pulse frequency, duty cycle and what effects does that have on the spark ignition timing. The more important question is whether there will be an additional delay due to moving the trigger circuit signal from the ignition coil input (where it was in previous generation combustion chamber) to the counter square pulse digital output of the DAQ.

A simple experiment was designed to answer those questions. A high speed camera recorded at 51,282 fps the spark plug discharge and multiple tests were initiated from Labview at different frequency ranging from 5Hz to 200Hz. The duty cycle was kept at 50% the whole time. The result of the test can be seen in Fig.2.12 and offers a simple explanation. The delay between sending a pulse from the DAQ to seeing the first visually generated spark is inversely proportional to the frequency of the square pulse. This can be seen by a plot of 1/f which shows a good agreement with the data point. It should be noted that as the last point at a 200Hz frequency which corresponds to a 12,000 RPM is slightly above the 1/f curve. This might be due the limitations of the ignition module circuit which is exceeding its high speed limit of 11,000 RPM. Throughout this experiment a square pulse of 50Hz with a 50% duty cycle was driving the spark ignition module.

We conclude from this test that the spark delay is solely a function of the square signal frequency driving the spark ignition module.

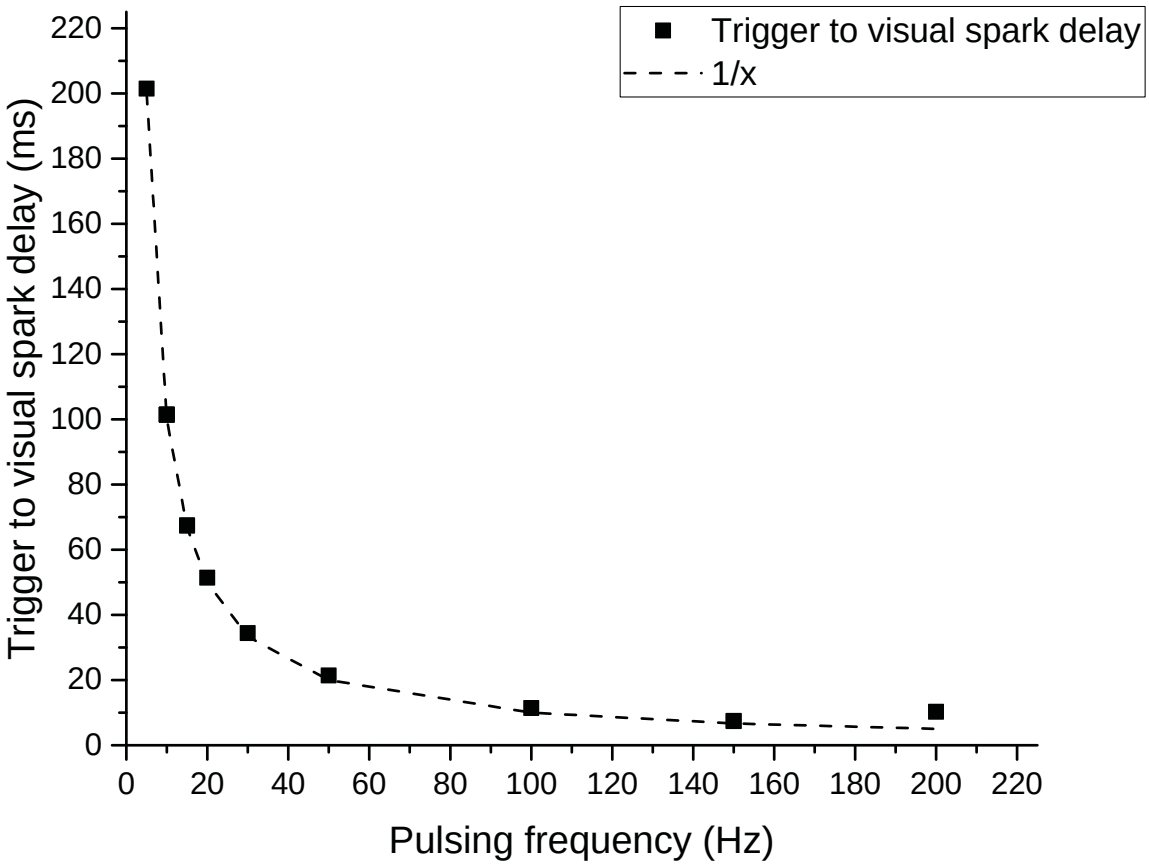


Fig. 2.12.: Visual spark event as a function of frequency of the driving pulse

### 2.3.3 Power box

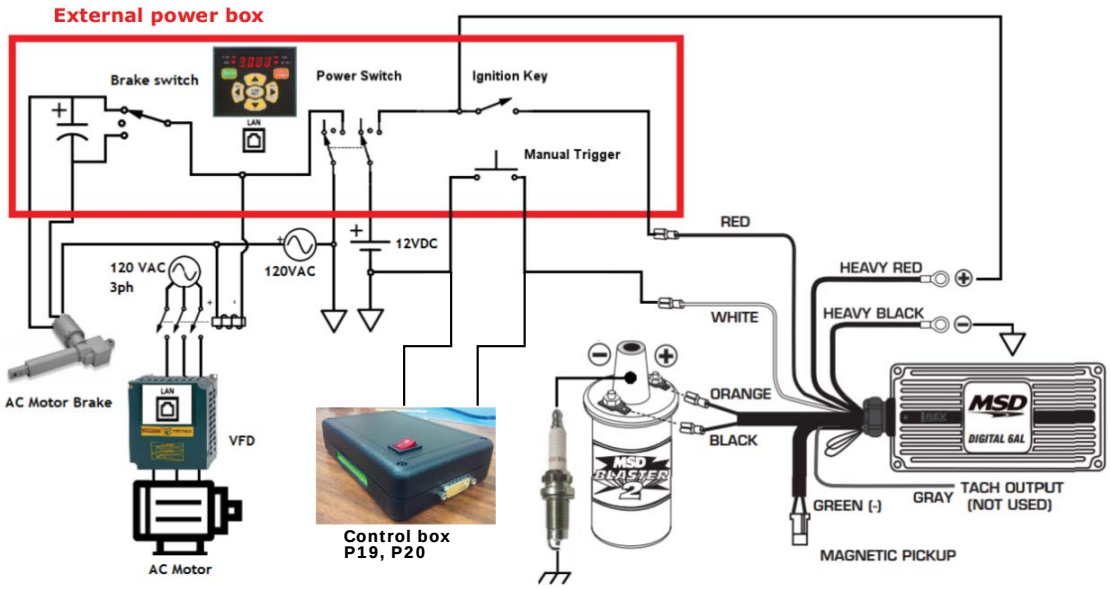


Fig. 2.13.: Power box for controlling motor, brakes, and ignition module

The electrical system controlling the rig consists of the electric motor, brake, ignition module and the control box. The external power box in Fig.2.13 houses the brake switch controlling a linear geared motor that opens and closes the brake pad to bring it in contact with the rotating pre-chamber. The VFD drive is remotely controlled by a panel mounted on the external power box. There is an option to manually push a button to initiate spark ignition, as well as ignition through the control box. The ignition control module made by MSD receives the spark ignition square pulse signal and output 500 V into the ignition coil which steps up the voltage to tens of kilo-volt to initiate the spark breakdown.

## 2.4 Fueling System

Three different fuels are used in this experiment. A pure methane fuel, a pure hydrogen fuel, and a 50% mixture of hydrogen methane. The fuel cylinders are filled

from Praxair with 99.97% purity for methane, and 99.999% purity for hydrogen. For consistency with previous experiments of Paik [15] the same 50% CH4/H2 mixture was used in the pre chamber. However, 3 test fuels were used in the main chamber: pure hydrogen, pure methane, and 50% CH4/H2.

The fueling system goal is to deliver the exact amount of fuel repeatedly to the main chamber and pre-chamber. The ideal fueling process should be automated with minimum human intervention. In this project, the fueling of the pre-chamber was improved by simplifying the process from two fuels discharge operation of hydrogen and methane to only one fuel discharge operation by preparing batches of 50% CH4/H2 mixed in a tank. And the main chamber was fueled through a mass flow controller which was calibrated for the 3 different fuels.

### 2.4.1 Piping

A fuel delivery piping set up was developed to enable repeated fast experiment. The piping and instrumentation diagram is shown in detail in Fig.2.14. The left grey rectangle shows the methane and hydrogen connected fuel valves along with a vacuum pump and all connected to a main header with an Ashcroft VAC/30psig digital pressure indicator of 0.25% accuracy. An air supply is also connected through a needle valve and is used to pressurize the pre-chamber before the addition of fuel to achieve 1.5 and 2 atm pre-chamber initial pressure. The vacuum pump is used to vacuum the pre-chamber in order to add the right amount of fuel to reach the prescribed equivalence ratio of 1.1 at 1 atm. The right grey rectangle shows a 1000 $cm^3$ batch preparation tank, a smaller buffer tank of 50 $cm^3$, a mass flow rate controller and a digital pressure indicator made by CECOMP with a 300 psig and 0.25% accuracy.

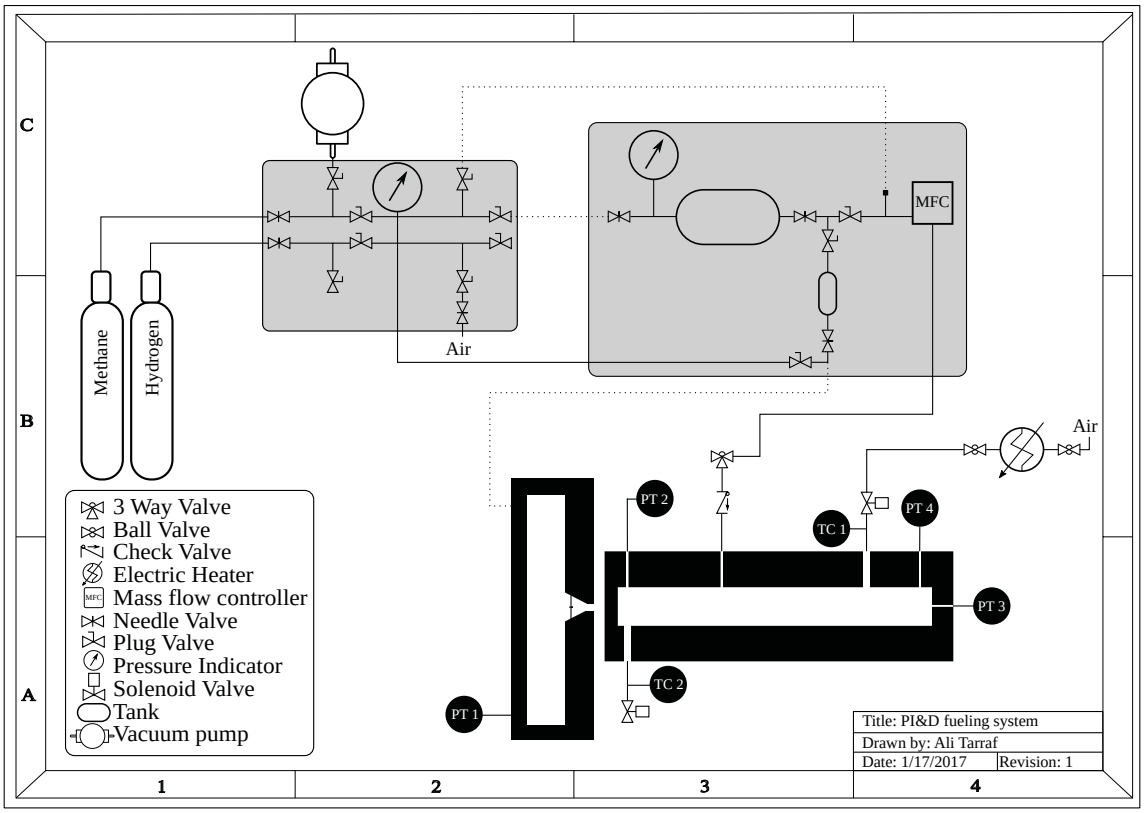


Fig. 2.14.: Piping and instrumentation diagram

The dotted lines represent non-permanent connection made out of 1/4" plastic tubing that can be removed with quick disconnects. The batch preparation tank fills the buffer tank and piping system with enough fuel to deliver to the pre chamber through a needle valve. The pre chamber pressure is monitored by the Ashcroft digital pressure indicator. The CECOMP is only used for batch preparation partial pressure fueling. The mass flow controller is pressure insensitive and capable of operating multiple fuels with different in built calibration. The MFC used is the PFC-60 made by MKS instruments with a 1000 SCCM maximum mass flow rate.

On the main chamber side, the fuel out of the MFC passes through a 3 way valve and a check valve before going into the main chamber channel. The check valve is made by Swagelok and has a 1/3 psia pressure drop. It prevents any back flow into the MFC from the combustion pressure. The 3-way valve allows a second

fueling pathway to the main chamber without dismantling the MFC piping circuit. The two solenoid valves are made by Parker model 71215SN2MN00 with an orifice of 1/8" and a maximum pressure of 200 psia. However the solenoids orifice size limited the mass flow rate delivered along with the 1/4" tubing between the heater and the main chamber inlet. So a further upgrade replaced the tubing with 1/2" stainless steel 304 pipe along with 1/2" brass valve which were used for all the elevated temperature experiments. These valves were chosen for their economical price. Further upgrades to the rig may select 1/2" solenoid controlled valve to improve fueling time performance.

### 2.4.2 Batch Preparation

Air is vacuumed to minimize the amount of air in the batch preparation tank shown in the right gray box of Fig.2.14. And then equal portion of methane and hydrogen are filled in by the partial pressure method. The first batch made contained about 5% of air, and was emptied. A second and third batch were made and used for practice testing of different valves. With every batch being made the concentration of air with respect to the whole mixture is decreasing. This is assuming a homogeneous fully mixed tank for each batch. A waiting time of 30 min was allowed for the mixture to sit still to insure homogeneity. Each test in this experiment can be tracked by a fueling batch number so that any issues with the data can be traced back to a bad batch if the need arise. The concentration of residual air, hydrogen and methane have been calculated for each batch and is summarized in Table 2.2.

It should be noted that this reports tests used batch number 9 to batch number 20. While air percentage is practically null, there is some differences in the mixture concentration between $H_2$ and $CH_4$ with a maximum of 0.76% for batch 11. However, these differences are not expected to influence the pre-chamber overall combustion pressure. Mixing air and hydrogen or methane requires careful

Table 2.2: Batch concentration of mixture used for all pre-chamber fueling, and for 50% $CH_4/H_2$ tests

| *Batch#* | *Air* (%) | $H_2$ (%) | $CH_4$ (%) |
|---|---|---|---|
| 4 | 0.141 | 50.338 | 49.521 |
| 5 | 0.048 | 50.258 | 49.694 |
| 6 | 0.019 | 50.102 | 49.879 |
| 7 | 0.008 | 50.041 | 49.951 |
| 8 | 0.003 | 50.019 | 49.978 |
| 9 | 0.001 | 50.004 | 49.995 |
| 10 | 0.000 | 49.862 | 50.138 |
| 11 | 0.000 | 49.617 | 50.383 |
| 12 | 0.000 | 49.747 | 50.253 |
| 13 | 0.000 | 49.951 | 50.049 |
| 14 | 0.000 | 50.058 | 49.942 |
| 15 | 0.000 | 49.948 | 50.052 |
| 16 | 0.000 | 49.795 | 50.205 |
| 17 | 0.000 | 50.096 | 49.904 |
| 18 | 0.000 | 50.031 | 49.969 |
| 19 | 0.000 | 50.146 | 49.854 |
| 20 | 0.000 | 49.827 | 50.173 |

consideration to avoid creating flammable mixtures. The flammability limits of hydrogen is 4 -75% content of hydrogen in air at 1 atm. And methane flammability is from 5- 15% content of methane in air [26]. Thus the above batches concentration are non-flammable mixtures.

### 2.4.3 Mass Flow Controller

Fuel delivery to the main combustion chamber is done through a mass flow controller for two reasons:

1. To decrease the fueling procedure time which is critical for the high temperature case because of heat loss.

2. To increase repeatability and accuracy of the fueling process for the three different fuels.

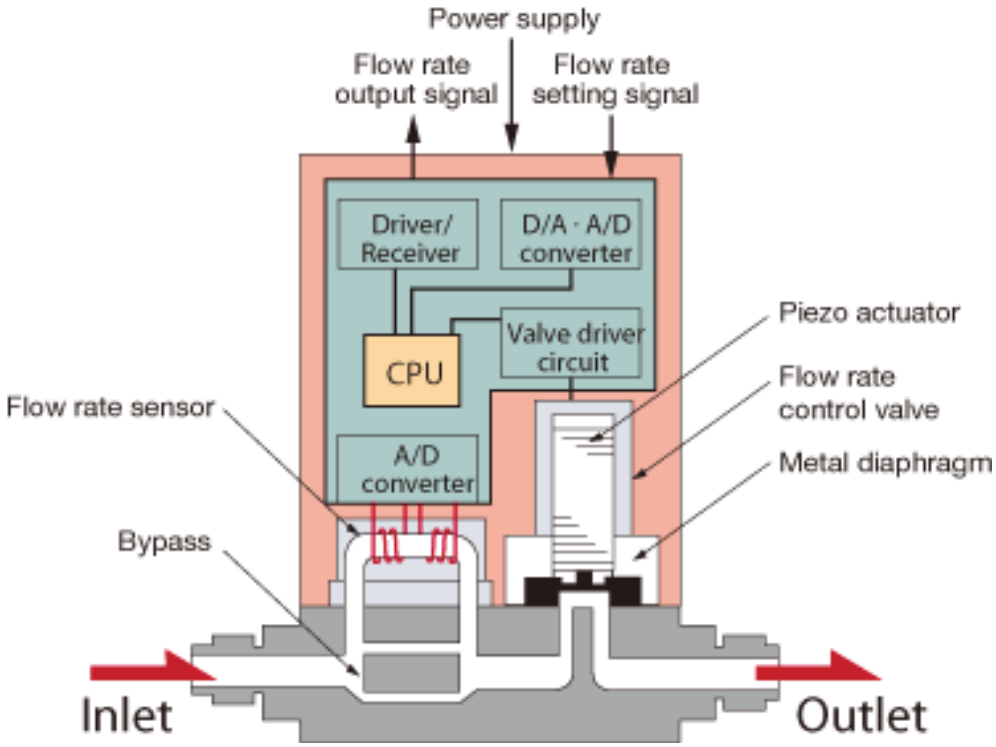


Fig. 2.15.: Internal structure of MFC [27]

A mass flow controller is composed of two main internal devices: a flow measuring device, and a flow rate control valve. The principle of operation [28] of the MFC rests on a closed loop control system between the flow rate sensor and the

solenoid flow control valve. The flow rate sensor measures the actual mass flow rate through monitoring the temperature difference between the upstream and downstream of the resistive heated winding. The higher the mass flow rate the greater the temperature difference between windings. The solenoid valve will open to allow the mass flow rate required by the setting signal of the user. The flow sensor is constantly monitoring the mass flow to make the necessary changes to the valve voltage signal to keep the mass flow rate constant.

The MFC used in this experiment is model PFC-60 made by MKS. It has a maximum mass flow rate of 1000 SCCM. It is pressure insensitive and has multiple fuel calibration settings. Pressure insensitive means that it will adjust the flow as the upstream pressure changes. This is important in our case since the fueling operation is made from a small buffer tank which will drop with time. A test has been done to validate that the mass flow rate is insensitive to the upstream pressure by varying the voltage set point signal and reading the mass flow rate data. Two different pressure points are reported at 53 psig and 85 psig, the reported mass flow rate is in good agreement as shown in in Fig.2.16.

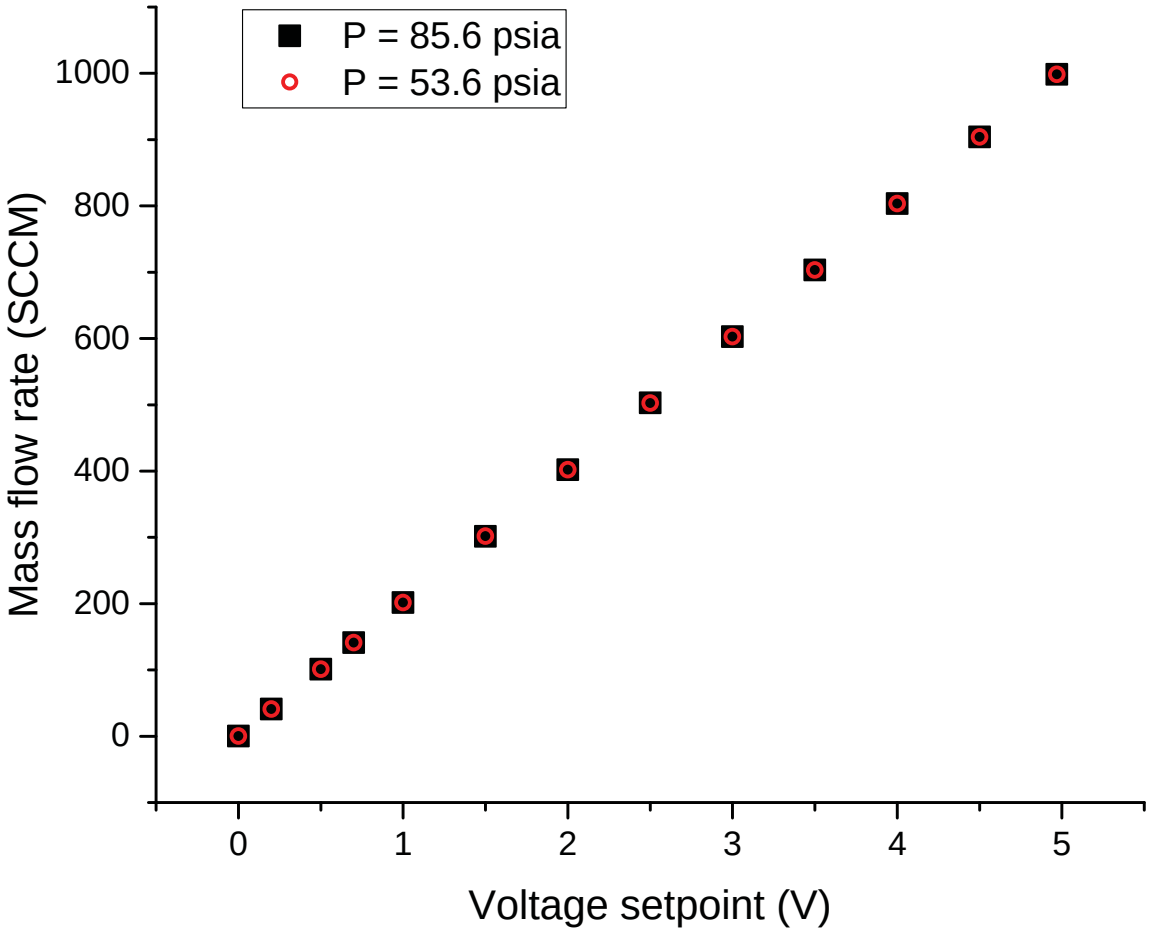


Fig. 2.16.: Tests showing that MFC is insensitive to upstream pressure variation

MFC are typically used in steady state operations with constant gas flow. However the fueling process requires a precise amount of fuel and is not a steady state process. The uncertainty of using the MFC for a non-steady state application prompted the validation of the calibration curves. In addition the PFC-60 has in built calibration curves (by the manufacturer) for methane, and for hydrogen, but not for a 50% mixture of methane hydrogen. A volume displacement method calibration was used to calibrate the MFC. A picture of the set up can be seen in Fig.2.17.

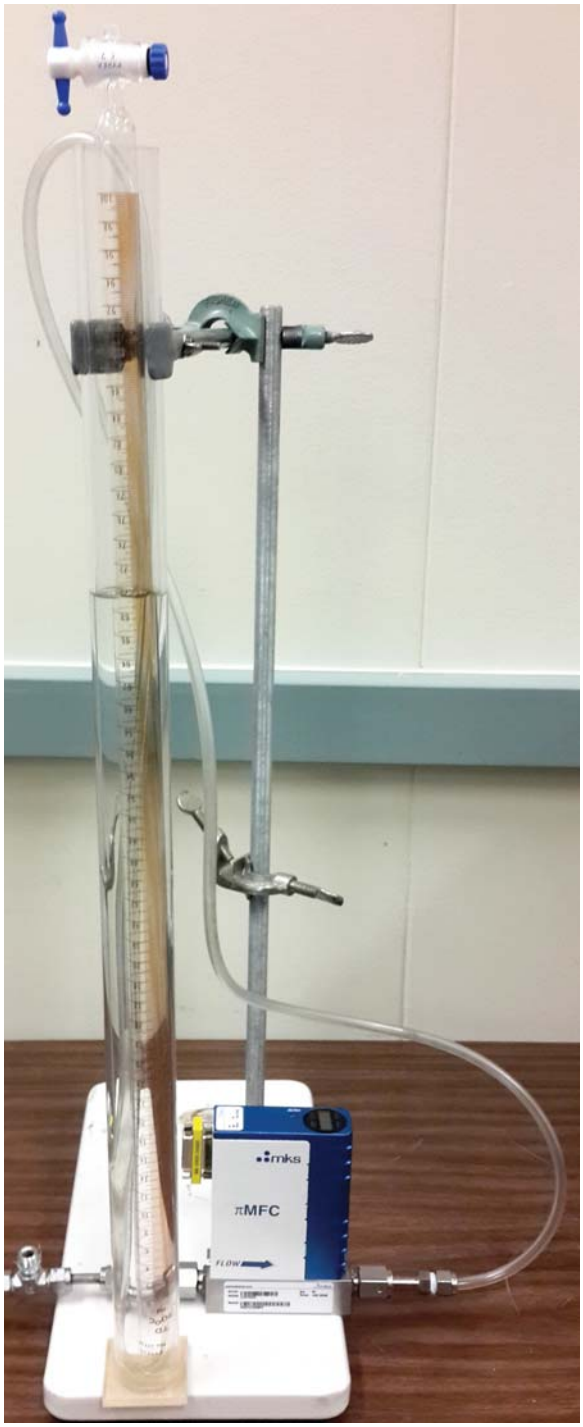


Fig. 2.17.: Volume displacement set up used for calibrating the MFC

A 100ml burette with 0.1ml graduation was immersed in an acrylic made container. The MFC output was piped through a plastic tube to the lower entrance

of the pipette and the top exit was closed with its valve. Once the gas is discharged from the MFC it passes through the water in the acrylic container and in the burette. Buoyancy pushes the gas to the top of the pipette where it is trapped. The trapped gas pushes the water back to a lower level. The difference in level is read and the volume measured is converted to mass using the ideal gas law with local atmospheric temperature and pressure. The PFC-60 reports a voltage from 0-5V which corresponds to the mass flow rate depending on which full scale output is selected through the settings.

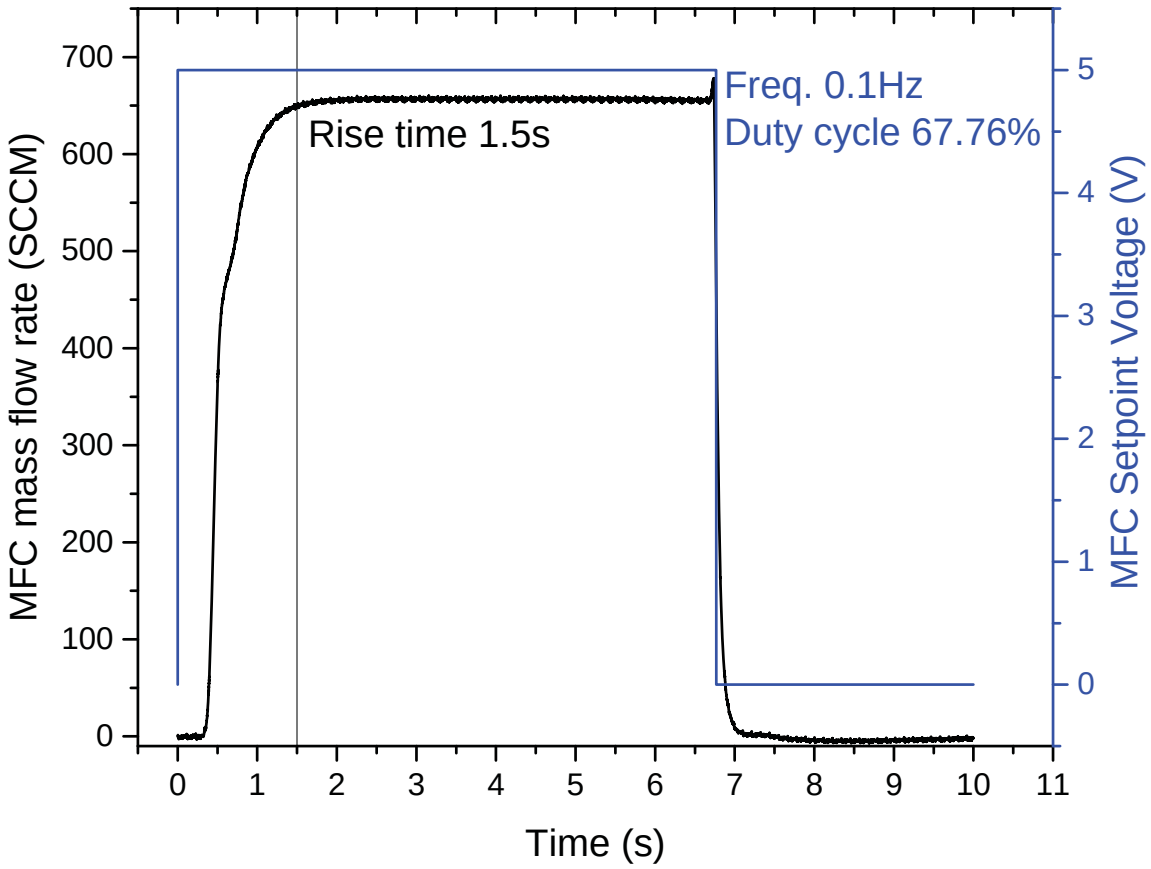


Fig. 2.18.: Sample square pulse setpoint signal and flow rate in SCCM

For example if a methane gas is selected the full scale output is 720 SCCM corresponding to 5V and 1000 SCCM for hydrogen. This output is read as an analog input in the DAQ. For the calibration curves used in this report a single

pulse square wave of 5V was used as a set point signal and the on time was varied. A sample square pulse signal and flow rate is show in Fig.2.18 corresponding to 50% methane hydrogen mixture. An initial delay less than 0.5s, followed by the rise of the flow rate gives a total rise time to 1.5s. The fall time of the signal is much quicker. This means that set point signals which have a short on time are going to be less accurate than signals with a longer on time due to the uncertainty around the rise time. This corresponds to the manufacturer datasheet settling time of 1-2s. In the actual experiments, the minimum on time selected was 3s, minimizing the difference between the calibrated flow rate and the reported flow rate by the MFC.

Three calibration tests were performed for the three different fuels. The internal setting selected were methane, and hydrogen fuel. The methane setting was used for both the methane, and the 50% methane hydrogen mixture. Hydrogen settings were used for the hydrogen calibration. Table 2.3 shows a comparison of the factory settings and the lab calibrated settings. The factors are used to transform the voltage flow rate signal to a mass flow rate signal with SCCM as a unit.

Table 2.3: MFC flow rate Voltage to SCCM calibration factors. Units: SCCM/V

| **Fuel** | **Factory constants** | **Lab measured constants** |
|---|---|---|
| $CH_4$ | 144 | 115 |
| 50 % $CH_4/H_2$ | NA | 131 |
| $H_2$ | 200 | 200 |

An unexplained difference was found in calculating the methane factor between the lab and the factory setting while an excellent agreement was found with hydrogen. The lab factors were found by minimizing the error between the reported MFC flow rate, and the volume displacement flow rate. A factor of 200 SCCM/V for methane gave differences as high as 23% in mass delivered, thus the factor used for methane for the rest of the experiment was 115 SCCM/V. Plot of the calibration

curve of methane, methane/hydrogen, and hydrogen are shown in Fig.2.19, Fig.2.20 and Fig.2.21.

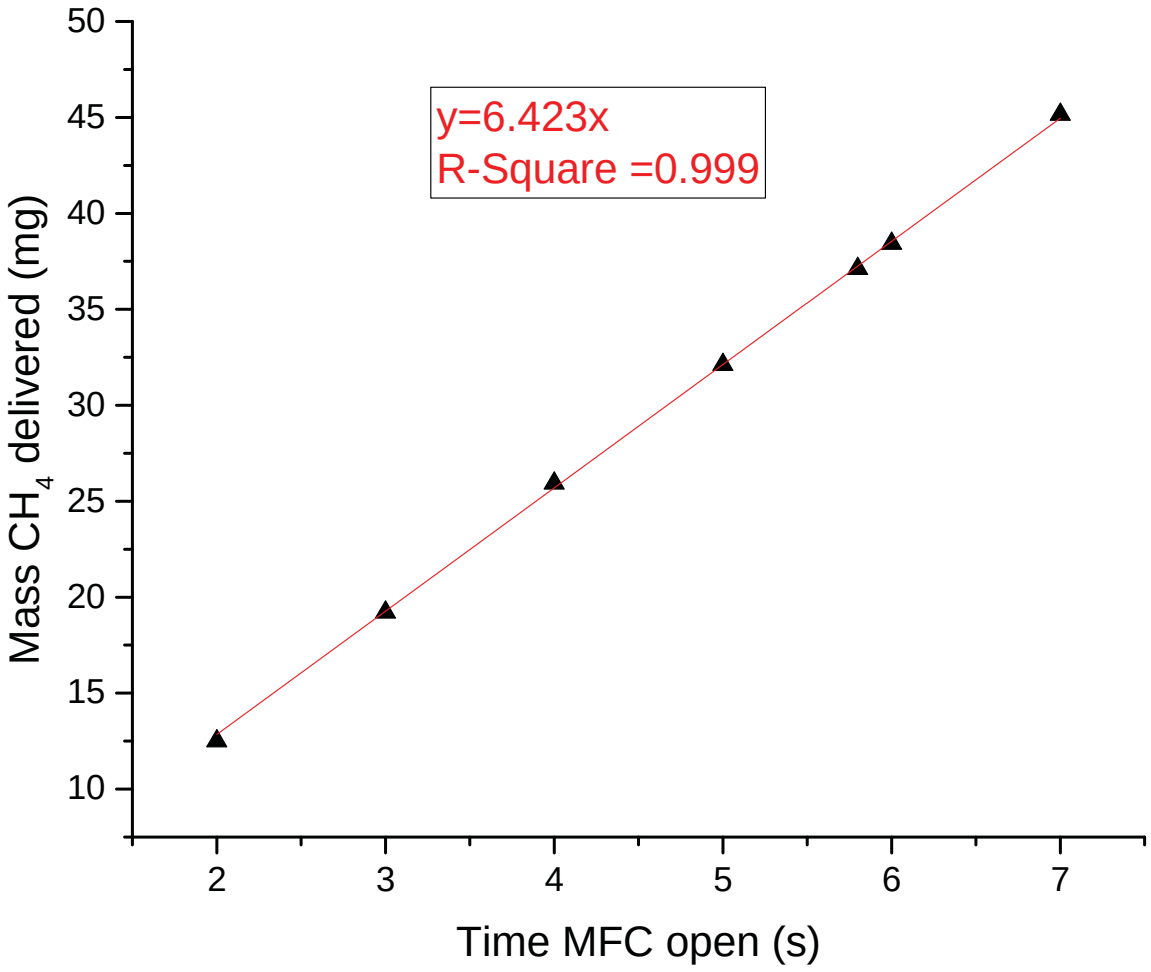


Fig. 2.19.: Methane calibration curve

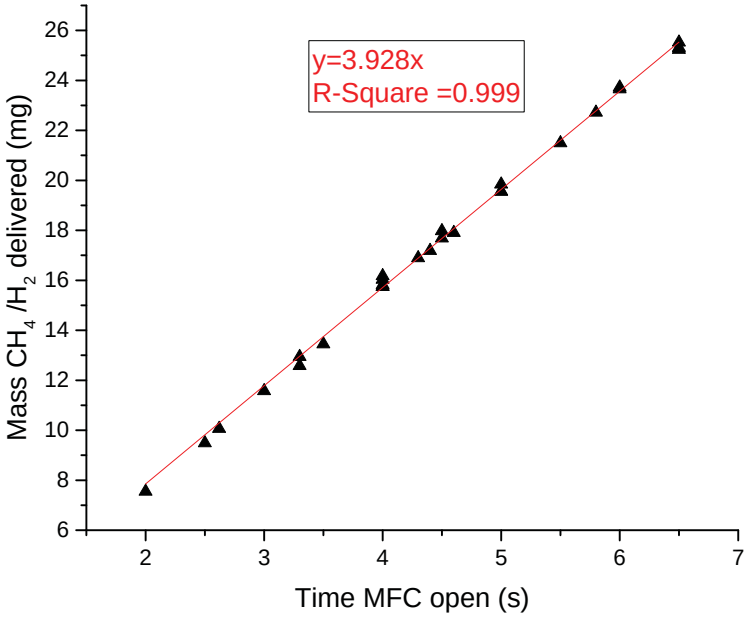


Fig. 2.20.: 50% Methane/Hydrogen calibration curve

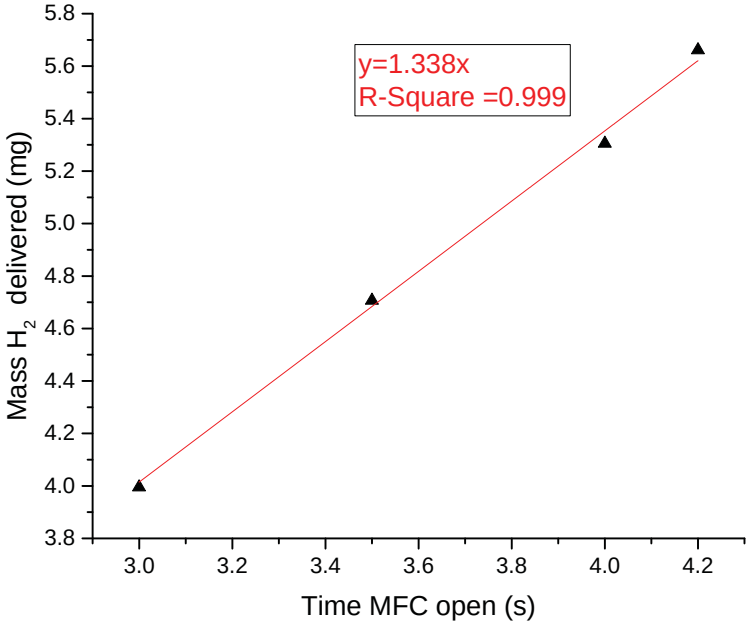


Fig. 2.21.: Hydrogen calibration curve

The MFC shows a linear behavior in the three different fuels, and a linear relationship with a zero intercept is derived for the three fuels. The mass of fuel

delivered shown in the three calibration plots is calculated from the volume displacement readings adjusted for local atmospheric pressure and temperature. It is important to mention that the relationship between time MFC is open and mass delivered is independent of small atmospheric pressure variation, because the mass flow rate controller as its name indicates is actually measuring and controlling the mass delivered. So the relationship is valid for other near atmospheric conditions at which the volume displacement measurements were made. It should be noted that the fewer number of points in the hydrogen calibration compared to the other two fuels is due to the limitation of the acrylic cylinder volume and burette length. Hydrogen density is very low and takes much more volume to deliver the same amount of mass. A comparison of the mass flow rate reported value with the adjusted lab factors and the volume displacement method is studied in Fig.2.22, Fig.2.23 and Fig.2.24.

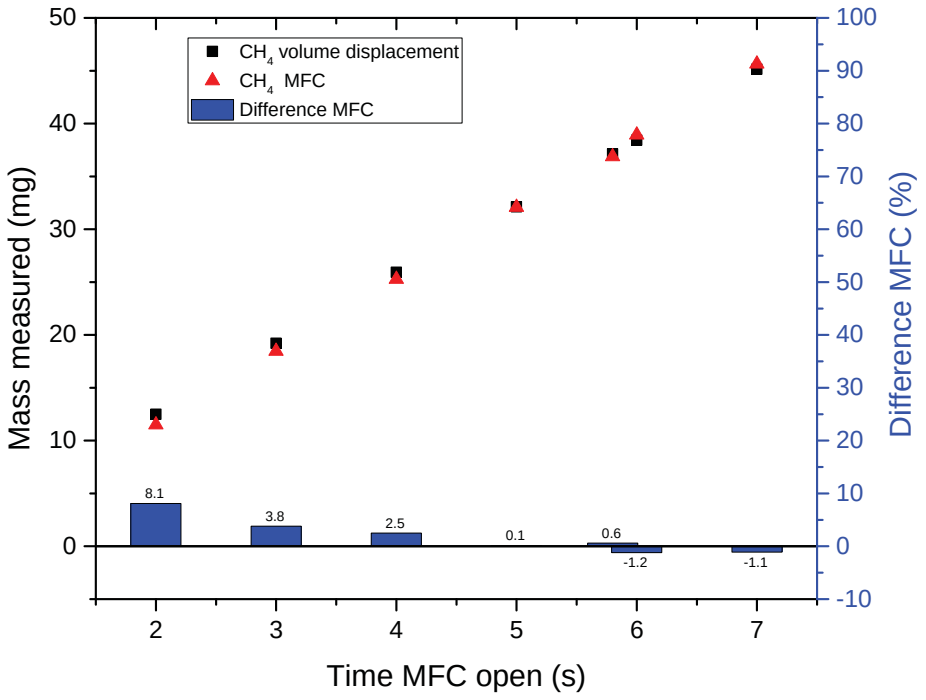


Fig. 2.22.: MFC to volume displacement difference in % for methane

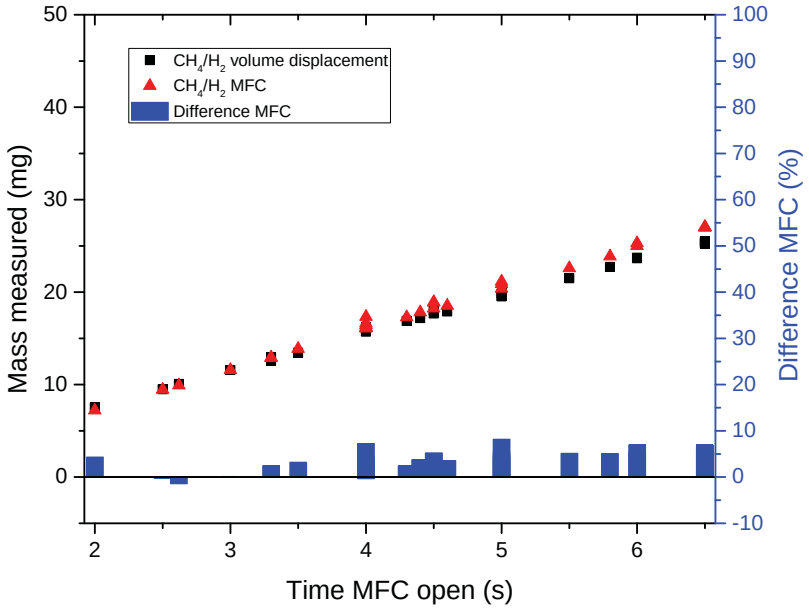


Fig. 2.23.: MFC to volume displacement difference in % for Methane/Hydrogen

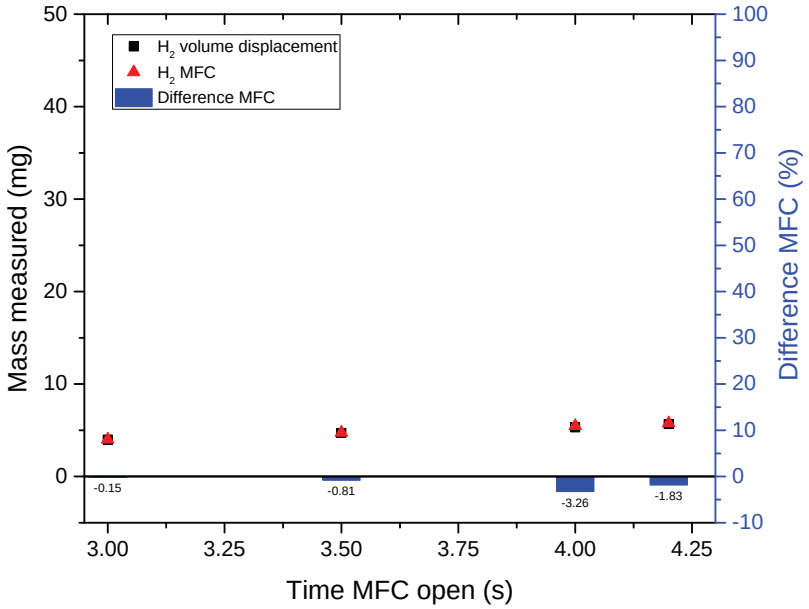


Fig. 2.24.: MFC to volume displacement difference in % for Hydrogen

The MFC mass measured is shown in the red triangles and the volume displacement in the black boxes. The MFC percentage difference is shown in the

column bars with respect to the volume displacement method. For $CH_4$, the calibrated conversion factor of 115 SCCM/V gives an MFC to volume displacement measurement difference of 8% for 2s on time of the valve, but a much closer 1.5% average absolute difference for the 6 other points. The 8 % error is expected to be due to the very short pulse time which is very close to the actual rise time of 1.5s of the MFC. The $CH_4/H_2$ mixture has a calibrated factor of 131 SCCM/V which gives an average absolute difference of 3.7% between MFC and the volume displacement method. The $H_2$ mixture has a calibrated factor of 200 SCCM/V which is matching the factory calibration and gives an average absolute difference of 1.5%. These differences are deemed to be acceptable since in the experimental procedure the MFC measured mass is only used to make sure that no big deviation from the volume displacement predicted mass. In the experiment fueling calculation the linear fit equations in Fig.2.19, Fig.2.21 and Fig.2.20 are used to calculate the required opening time, to deliver the necessary amount of mass to match the target equivalence ratio.

### 2.4.4 Fueling Calculations

Balancing the chemical reaction of methane hydrogen as a fuel with air, and expressing the ratios of elements in terms of equivalence ratio we can write using the ideal gas law

$$\frac{P_{Air}}{P_{Fuel}} = \frac{2.38(3X_i + 1)}{\phi} \quad with \quad X_i = X_{CH_4}, \quad X_{CH_4} + X_{H_2} = 1 \tag{2.1}$$

The fuel mixture batched prepared in the mixing tank contains residual air which we have to account for in our fueling calculations.

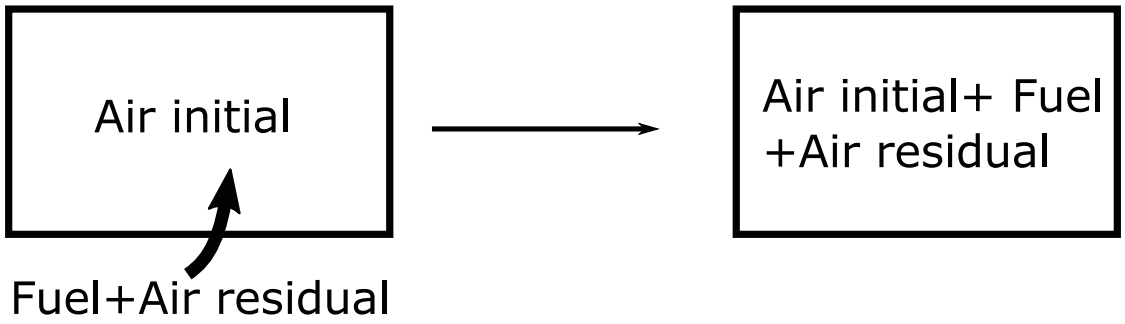


Fig. 2.25.: Diagram of pre-chamber fueling from the batch mixing tank

The diagram in Fig.2.25 shows the initial state of the pre-chamber containing initial air either at atmospheric pressure or at 1.5 and 2 atmosphere. The batch fueling operation will bring fuel and residual air in the pre-chamber to make the total pressure

$$P_{Tot} = P_{Fuel} + P_{AirResidual} + P_{AirInitial} = \Delta P + P_{AirInitial} \tag{2.2}$$

With the addition of the residual air the total air present in the pre chamber becomes

$$P_{air} = P_{AirInitial} + \Delta P X_{AirResidual} \tag{2.3}$$

With

$$X_{AirResidual} = \frac{P_{AirResidual}}{P_{AirResidual} + P_{CH_4} + P_{H_2}} \tag{2.4}$$

Replacing eq (2.3) into (2.1.) and adjusting we can write

$$\Delta P = \frac{Z}{1+Z} P_{Tot} \tag{2.5}$$

With

$$Z = \frac{\phi}{2.38(3X_i + 1)(1 - X_{AirResidual}) - \phi X_{AirResidual}} \tag{2.6}$$

For the batches used in the testing $X_{AirResidual}$ was assumed to be zero which simplifies the $Z$ factor to a form close to eq (2.1).

Fueling the main chamber is done through the mass flow controller. The required mass to be delivered by the mass flow controller is calculated by finding the

mass of air present in the chamber at the specified temperature. Assuming ideal gas behavior, we can write

$$m_{Fuel} = \frac{P_{air} V_{main} M_{air} \phi}{(A/F) R T_{air}} \tag{2.7}$$

The MFC on time regulates the amount of mass delivered according the to calibration equation derived for mass versus time shown in Table 2.4. The on time can be calculated from $m_{Fuel}$:

$$t_{on} = \frac{m_{fuel}}{k} \tag{2.8}$$

with $k$ defined as the MFC calibration constants derived from Fig.2.19, Fig.2.20 and Fig.2.21.

Table 2.4: MFC mass to time calibration constants

| **Fuel** | **Constant** $k$ |
|---|---|
| $CH_4$ | 6.423 |
| 50 % $CH_4/H_2$ | 3.928 |
| $H_2$ | 1.3383 |

Table 2.5: Mass of fuel in milligrams for an atmospheric pressure of 101.3 kPa and ambient temperature of 297 K and for different main chamber temperature and equivalent ratio

| | $CH_4$ | | $H_2$ | | $CH_4/H_2$ | | |
|---|---|---|---|---|---|---|---|
| $\phi$ | 297 K | 500 K | 297 K | 500 K | 297 K | 400 K | 500 K |
| 0.4 | 19.42 | 11.54 | 9.74 | 5.79 | 17.53 | 13.02 | 10.41 |
| 0.7 | 33.98 | 20.19 | 17.05 | 10.13 | 30.68 | 22.78 | 18.22 |
| 1 | 48.55 | 28.84 | 24.35 | 14.47 | 43.83 | 32.54 | 26.04 |
| 1.5 | 72.82 | 43.26 | 36.53 | 21.7 | 65.75 | 48.82 | 39.05 |

Using mass versus time relationship just derived, we can calculate the mass and time the MFC needs to supply fuel. A sample calculation is shown in Table 2.5. The highest delivery time is for hydrogen at 297K amounting to 27.29s. The lowest delivery time is for methane at 500 K amounting to 1.8s. The highest delivery time for high temperature cases of 500K is for hydrogen at an equivalence ratio of 1.5, amounting to 16.21s. For the high temperature cases, a long delivery time means that the chamber has more time to cool. In the heating section we accounted for 20s of cooling before ignition. So in the particular case of hydrogen at 1.5 equivalence ratio the experimenter has 4s after shutting off the heating air until ignition. This was found hard to achieve, the average time between shutting off the air heating and ignition was 8s. So in order to account for that the chamber was left to heat more until the outlet temperature reached 530 K.

## 2.5 Instrumentation And Data Recording

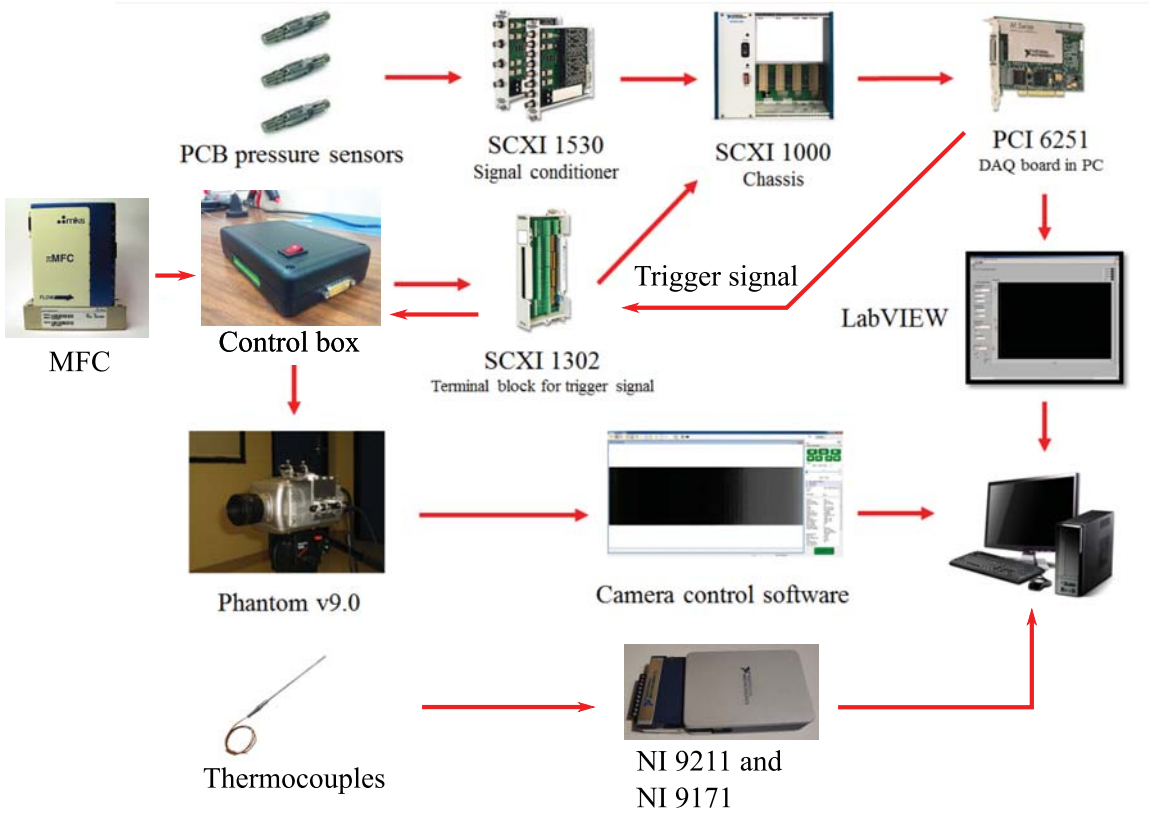


Fig. 2.26.: Schematic showing all the elements of the data acquisition system

The recorded data in the experiment consists of pressure, Schlieren videos, temperature, and flow rate. A schematic showing all the data acquisition components can be seen in Fig.2.26. Four main data path can be outlined from Fig.2.26. The first data path is the pressure information being amplified in the SCXI 1530 and routed to the DAQ in the PC. The second data path is from the DAQ to the MFC through the terminal block and control box. The third data path is from the camera video output connected by LAN to the PC. The fourth data path is the temperature data from the thermocouple to the NI9211 and NI9171 compact USB DAQ to the computer. As explained in the control section, the trigger signal is coupled to the spark plug pulse signal through the control box. This proved

to be an effective solution that eliminated the previous coupling with the noisy inductive coil signal.

Fig.2.27 shows a snapshot of the user interface made in Labview. On the left pressure traces, and mass flow controller settings. On the top right temperature traces. On the bottom right schlieren images.

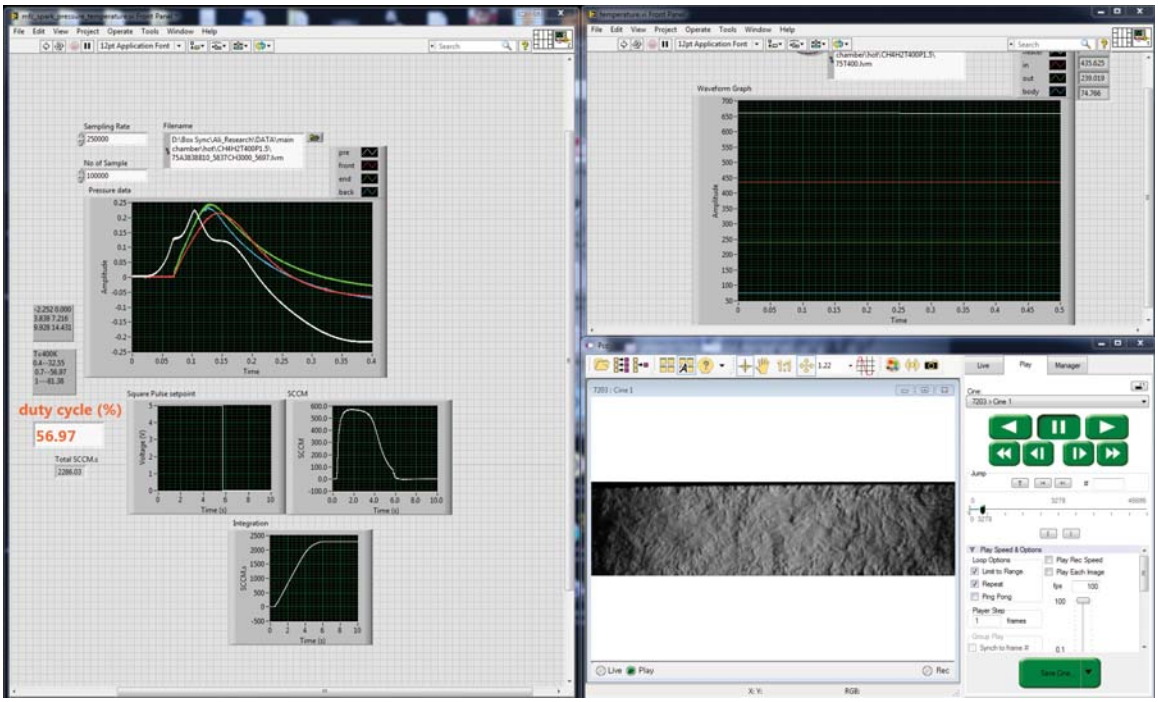


Fig. 2.27.: Snapshot of the user interface

### 2.5.1 Pressure Transducers

Paik [15] described in details the pressure transducers so only a summary will be given here. The pressure transducers used are dynamic AC coupled pressure transducer that can measure events in the order of several hundred kilohertz. The fast response rate of the pressure sensors allows the detection of shock waves pressure rise, and narrows down the ignition pressure rise time range. Typical shockwave speeds measured are from 350m/s to 470 m/s. A 470m/s shockwave passing under a pressure probe orifice of 1/8" would need pressure transducer

response rate of 148 kHz in order to capture at least one point of the shock traversing event. All pressure data collected in this experiment were acquired at a minimum of 250 kHz. The pressure sensor were calibrated at the PCB factory before the experiment. Table 2.6 below shows the calibration data and the pressure sensors used as well as the installation description.

Table 2.6: Factory calibration of pressure sensors

| PT# | Model | Serial number | Calibration (mv/psig) | Installation |
|---|---|---|---|---|
| PT1 | 111A26 | 14462 | 9.906 | Cylindrical cavity |
| PT2 | 113B26 | 28580 | 9.861 | Infinite probe |
| PT3 | 113B26 | 28466 | 9.725 | Flush |
| PT4 | 113B26 | 28465 | 9.992 | Chamber cavity |

PT 3 is installed flush at the end of the chamber and is the main indicator of the main chamber pressure in the analysis section. A cylindrical hole separates PT1 from the pre chamber. PT2 probe was designed by Paik [15] and is used in the same configuration. This author was interested in comparing the effect of a different probe configuration on the pressure response and designed a new mounting configuration for PT4. The pressure sensors face has an associated volume and a tubing that connects it to the main chamber. The estimated dimensions are shown in Fig.2.28. This tubing and volume connection cavity can be modeled as a Helmholtz resonator.

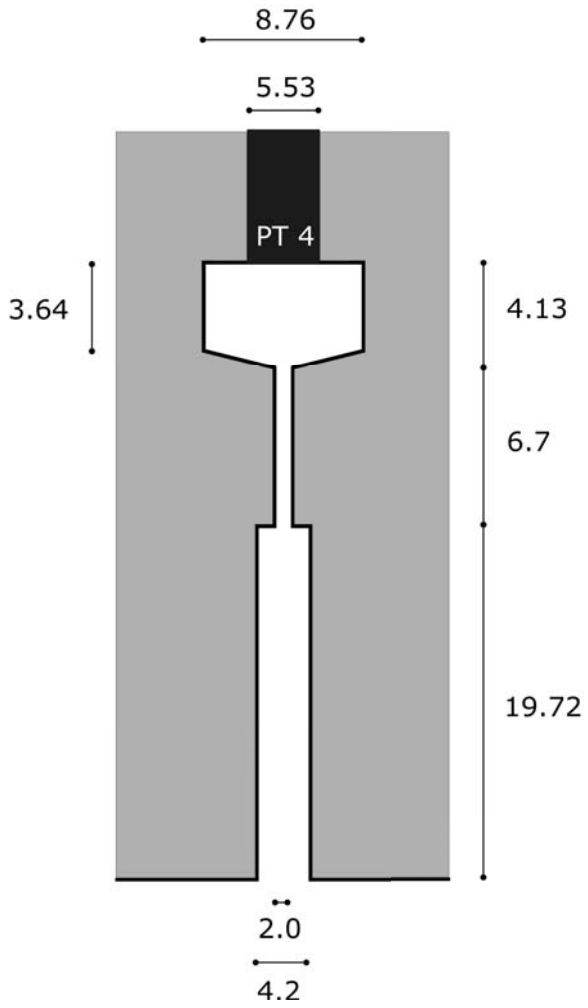


Fig. 2.28.: Dimensions of PT4 associated chamber and tube interconnection to the main chamber. Dimensions are in mm.

### 2.5.2 Thermocouple

Four K type thermocouples model number TJ250-CXIN made by Omega were utilized in 5 positions as shown in Fig.2.7. K type thermocouples can measure temperatures up to 1500 K which is adequate for this experiment because the maximum process temperature at the output of the heater is 1200 K. The NI 9211 thermocouple input module is used to collect temperature readings housed in the NI 9171 compactDAQ USB 2.0 chassis. The module has a maximum sampling rate of

14 samples per second, however in this experiment the sampling rate was fixed at 3 samples per seconds.

### 2.5.3 Mass Flow Controller

The mass flow controller has two connections to the DAQ. An analog input is required to read the 0-5V flow rate voltage from the MFC. Also an analog output is required to send the square pulse voltage from the DAQ to the MFC. The square wave voltage is from 0 to 5V and its duration and frequency can be modified. The duration can be set by varying the number of samples and the sampling rate along with the frequency in order to always obtain one cycle of the square pulse wave.

$$Duration = \frac{samples}{samples/s} \quad and \quad Frequency = \frac{1}{Duration} \tag{2.9}$$

The number of samples and samples per second is the same for the analog input flow rate data, and the analog output set point voltage. The flow rate voltage signal is multiplied by its SCCM conversion factor to have the flow rate signal in SCCM. This signal is integrated to yield the volume at standard condition.

### 2.5.4 Schlieren Visualization

Schlieren visualization technique was used to qualitatively analyze the ignition event, and determine the ignition point. The ignition point is determined by a sudden expansion of the combustion products which can be observed by the Schlieren method. For further details of the current Schlieren set up for this experiment refer to Paik [15]. Due to limitation of the size of the mirror used in the Schlieren set up, all of the 14.5" window length cannot be observed in a single frame. Two observation frames are used: the first frame looks at the front side of the chamber covering an estimated 7", and the second frame looks at the back side of the chamber covering another 7". Different resolutions and different frames speeds were used as the tests were being conducted in an effort to increase them.

Heating the chamber with hot air caused a lot of density gradient which clouded some part of the images requiring adjustment from time to time. Table2.7 shows the different resolution and frame speeds used for all the tests.

Table 2.7: Schlieren camera resolution

| Set up# | Resolution | FPS | Test# |
|---|---|---|---|
| S1 | 560x144 | 17021 | 1-41 |
| S2 | 496x144 | 18691 | 42-59 |
| S3 | 496x128 | 20833 | 60-147 |
| S1 | 528x128 | 20833 | 148-235 |

## 2.6 Experimental Procedure

A step-by-step description of the experiment procedure is outlined below. The starting point assumes the Schlieren is set up, the chamber and pre chamber are empty and clamped to each other using a C-clamp. The procedure described applies for high temperature experiment. However the procedure can be applied for atmospheric temperature experiments by skipping the steps dealing with the heater.

### 2.6.1 Procedure

1. Score the aluminum diaphragm and insert the nozzle in the pre-chamber. For the 1atm and 1.5 atm case one scoring pass was used. A scoring pass is composed of two stroke, one in the forward direction, and one in the return backward direction. For the 2 atm case half a score was used, meaning that only one forward stroke pass was performed. The reason is pressurizing to 2 atm was breaking the aluminum diaphragm with a full score.

2. Record atmospheric pressure and temperature. Calculate pre-chamber air and fuel pressure. Enter main chamber duty cycle in Labview GUI.

3. The heater start up procedure is done before the start of the testing. The heater set at 950F should be left to operate for at least 1 hour. Keep the inlet and outlet valve on until the exit temperature reaches 525 K for the 500 K case, and 425 K for the 400 K case.

4. 5-10 K before outlet temperature reaches its target temperature proceed to fuel the pre chamber. Either add air to the required pressure, or vacuum to the previously calculated pressure. Then using the needle valve located after the buffer tank precisely meter the required amount of fuel.

5. When the outlet temperature reaches the target temperature close the heater valve, inlet valve and output valve in that order. Directly proceed to start the Labview program which will initiate the MFC fueling procedure and the spark. This operation should take on average 5-8s.

6. Upon successful combustion, open the outlet valve first, and then the inlet valve and heater valve to purge the combustion products with hot air. Use the linear XY positioning table to move the chamber backward after removing the C-clamps.

7. Remove the nozzle and replace the diaphragm. Purge the pre-chamber with compressed air to push out the remaining combustion products. Do the same for the main chamber.

A typical successful combustion event in the main chamber is shown in Fig. 2.29.

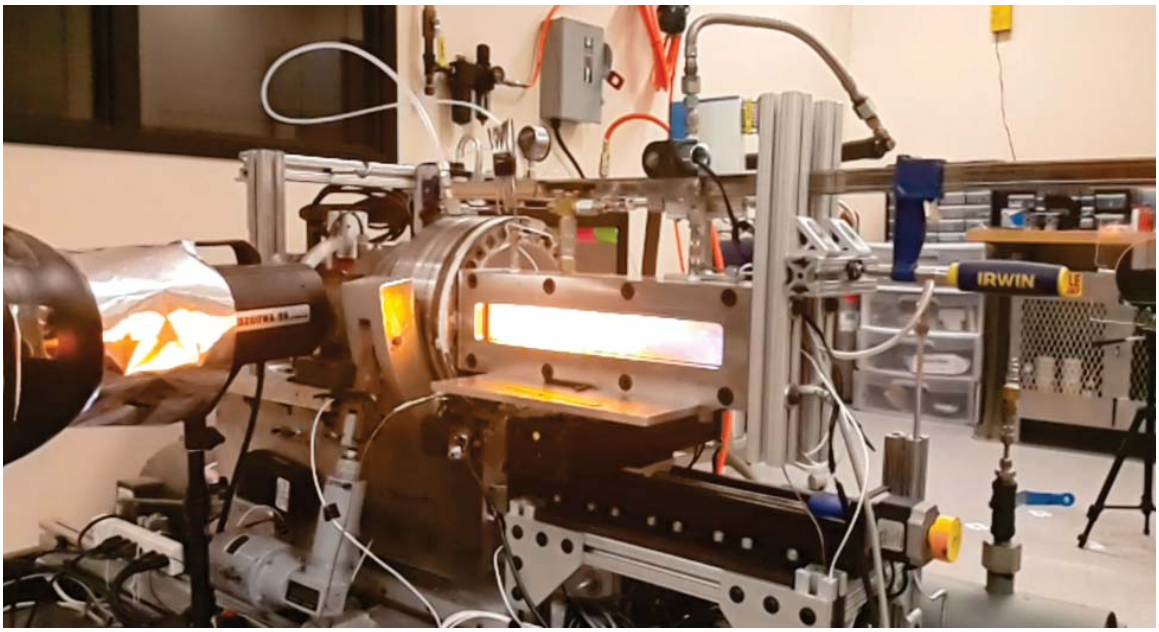


Fig. 2.29.: Combustion event in the main chamber photographed with a commercial camera

### 2.6.2 Test Space And Methodology

Table 2.8: Testing space variables

| Fuel | $\phi$ | P (atm) | T (K) |
|---|---|---|---|
| $CH_4$ | | | 297,500 |
| $H_2$ | 0.4,0.7,1,1.5 | 1,1.5,2 | 297,500 |
| $50\%CH_4/H_2$ | | | 297,400,500 |
| $50\%CH_4/H_2 - E$ | | | 297 |

A total of 263 tests were performed using a factorial methodology to cover the design space. 3 different fuels, 4 equivalence ratios, 3 initial pressure, and 2 temperatures (except for the 50% $CH_4/H_2$, an additional 400K temperature was added). This brings the total minimum experiment number to $3 \times 4 \times 3 \times 2$ to 72. In addition each experiment was repeated at least 2 times, and each testing case point had a front window observation and a back window observation.

A full list of the experiment of Methane and Methane/Hydrogen mixtures, along with preliminary analysis results is attached in the appendix. Partial list of Hydrogen experiments is included.

The $50\%CH_4/H_2 - E$ experiments were added at a later stage to study the difference between methane/hydrogen mixture at high temperature 500K and at low temperature 297K with equivalent densities. That is what the "E" stand for in the name of the fuel.

### 2.6.3 Notes

1. The SCXI 1000 should be on as well as the camera for the trigger system to work properly. The camera supply the 5V voltage required to trigger the pressure data acquisition as well as the camera recording.

2. The SCXI 1000 should be on for the MFC to work properly. Set point voltage analog output and flow rate analog input go through the SCXI 1302 which needs the SCXI 1000 chassis to function properly.

3. Atmospheric pressure changes were taken into factor when cumulative changes amounted to 5 mbar.

4. When configuring the MFC to change the operation gas, the IP address should be changed. After that, the IP address of the camera should be set up in order to detect the camera in its software application.

# 3. RESULTS

## 3.1 Pre-chamber

### 3.1.1 Benchmark Pressure Trace

A benchmark test was performed with a 50% methane hydrogen fuel in the pre-chamber and no fuel in the main chamber. The test recorded pressure traces and Schlieren images which are used as a reference benchmark to compare with test cases with fuel in the main chamber. This would enable the observer to distinguish between ignition and non ignition event. The critical data point to look for is the pressure rise in the near pressure values which indicates positive ignition. For example in the case of methane a low reactive fuel at a low equivalence ratio of 0.4, a modest pressure rise is observed in the event of ignition. Hence it is important to have a benchmark pressure trace to compare the modest pressure rise cases with main fuel in the chamber. Three tests repetitions were performed at different pre-chamber initial pressure. Plots in Fig 3.1, 3.2, 3.3 show the pre-chamber, front, and back pressure traces respectively with the main chamber and pre-chamber coupled similar to an actual test with main chamber fuel.

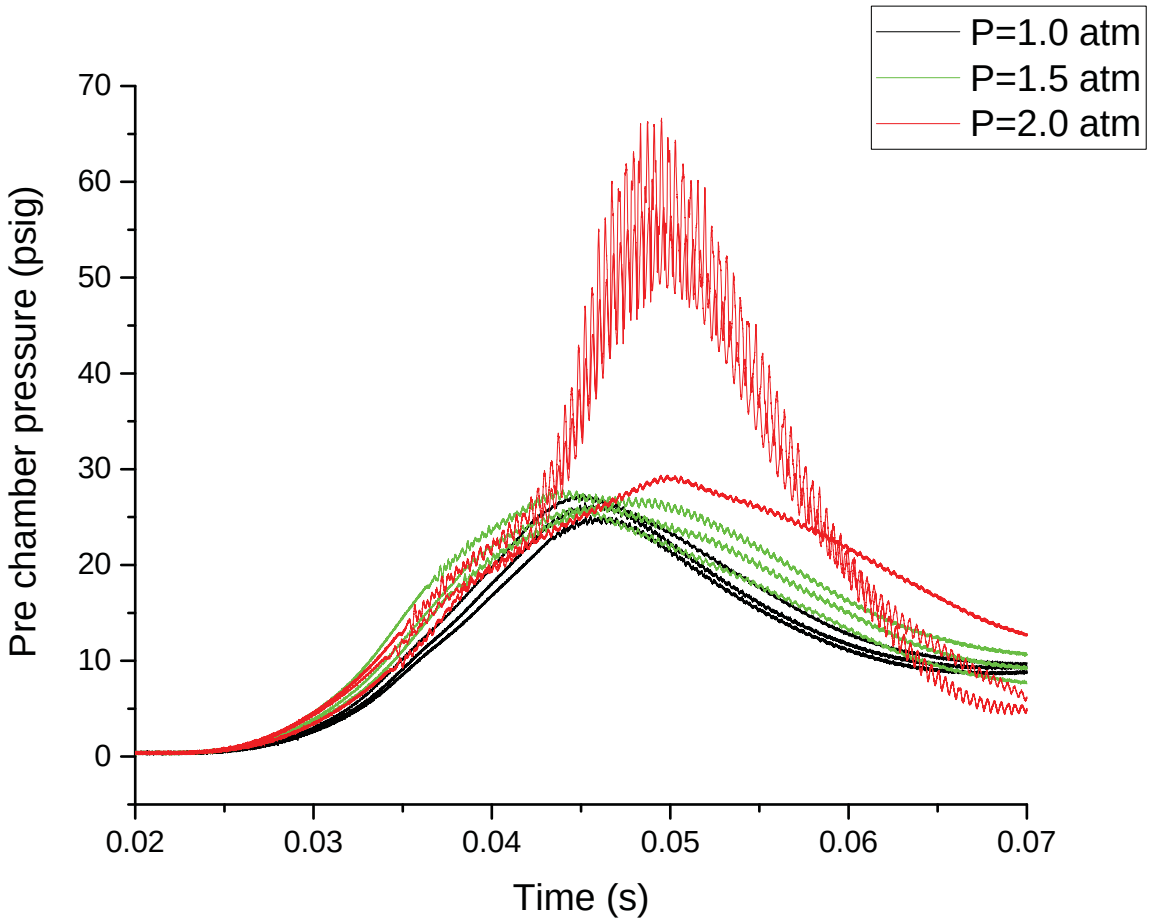


Fig. 3.1.: Pre-chamber pressure with 50% $CH_4/H_2$ at $\phi$ =1.1, and P= 1,1.5 and 2 atm. Three different repetition, total 9 cases.

Looking at pre-chamber pressure plots in Fig.3.1, we notice that the pressure traces is repeatable for the different initial pressures, except in one of the tests of the 2 atm cases. Two out of three cases of 2 atm has a maximum that oscillates between 50 and 65 psig, while the maximum of case 3 is close to 28 psig without any oscillations. Although the majority of test cases are repeatable, this indicates that the pre-chamber process can still exhibit different behavior in term of combustion, and pressure rise.

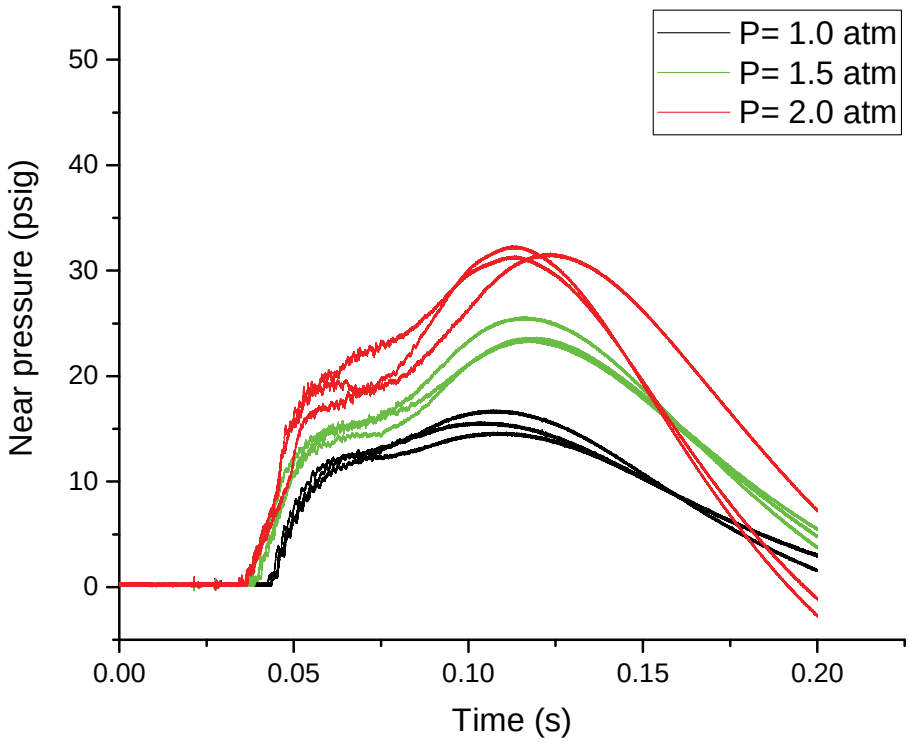


Fig. 3.2.: Front pressure in main chamber with pre-chamber 50% $CH_4/H_2$ at $\phi$ =1.1, and P= 1,1.5 and 2 atm. Three different repetition, total 9 cases. Main chamber without fuel, pressure rise due to hot jet exhaust from pre-chamber

The near pressure sensor is the closest to the ignition zone. Thus it is the first sensors to capture the rise in pressure due to the ignition event. Looking at the near pressure sensor trace we notice a gradual increase in pressure. This is in contrast to the pressure traces with ignition which exhibits a sharp increase. It might be possible to calculate a rise in pressure gradient number that is associated with ignition, but this would be a variable dependent on different fuel and pre-chamber settings. Over all , the near pressure sensors exhibit good repeatability. In Fig. 3.2 Test case 3 which had a lower pre-chamber pressure as explained in the previous paragraph is not affecting the near sensor. This is due to the mounting installation

of the sensor on an infinite tube which dampens the actual pressure. Although the absolute values reported by the near pressure sensor have lower amplitude, its timing information can be used accurately.

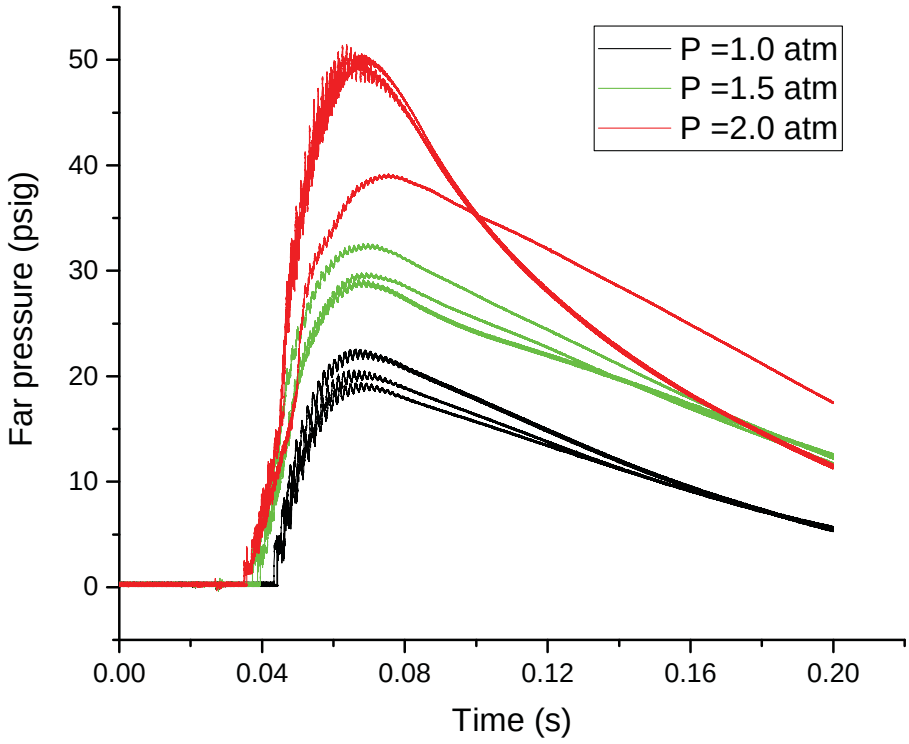


Fig. 3.3.: Far pressure in main chamber with pre-chamber 50% $CH_4/H_2$ at $\phi$ =1.1, and P= 1,1.5 and 2 atm. Three different repetition, total 9 cases. Main chamber without fuel, pressure rise due to hot jet exhaust from pre-chamber

In Fig 3.3 The far pressure sensor which is flush mounted shows an accurate total pressure of the main chamber, and thus shows the lower pressure associated with test case number 3 previously discussed in the pre-chamber trace paragraph. Again the pressure traces show good repeatability and agreement overall.

### 3.1.2 Comparison Of Different Pre-chamber Fuels

Perera [7] determined that the quickest to rupture fuel combination was 50% methane hydrogen at 1.1 equivalence ratio. It was of interest to study the different peak pressure that can be achieved by varying the fuel used inside the pre-chamber. In addition during experiments it was observed that the coupling of the main chamber to the pre-chamber has a dampening effect on the overall pressure inside the pre-chamber. Three tests have been performed for the normal case of both main chamber and pre-chamber coupled, and for the main chamber uncoupled from the pre chamber. Uncoupled is defined as the pre-chamber discharging its jet after diaphragm break up into the ambient atmosphere and not inside the main chamber. At the same time three different fuels were tested in both configurations.

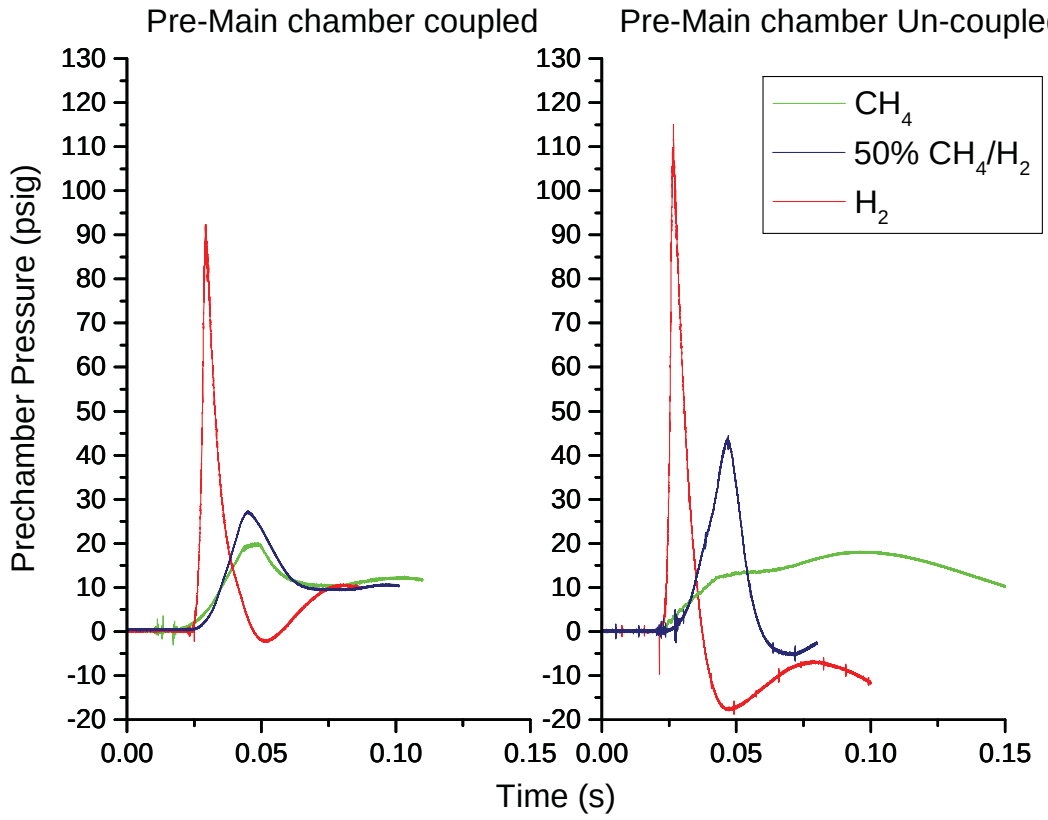


Fig. 3.4.: Pre-chamber pressure in main chamber with 50% $CH_4/H_2$, $H_2$, and $CH_4$ at $\phi$ =1.1, and P= 1 atm. Graph of the left shows pre chamber pressure for a coupled main/pre-chamber and on the graph on the right shows the uncoupled configuration. In all cases main chamber is without fuel.

The pressure traces in Fig. 3.4 shows expected results that pressure increases with fuel reactivity. The peak pressure is highest in the hydrogen case, followed by the methane hydrogen mixtures, and lowest in the methane case. And the coupling of both chambers affects the peak pressures negatively. Hydrogen is about 16% (18psig) smaller than the case with ambient atmospheric discharge. Similar reduction in pressures can be inferred for the methane hydrogen case with a 16 psig difference amounting to 35 %. However the methane case is different with the pressure build up is slower in the open ambient atmospheric discharge case. The

coupled chamber pressure is higher and has a quick rise profile. A possible explanation for having lower pressures in the coupled assembly is that the combustion products in the pre-chamber tend to stay longer inside due to the back-pressure exerted from the gas in the main chamber. This causes an internal dilution and lowers the reaction rate and hence the peak pressure.

### 3.1.3 Pre-chamber Jet Discharge

A time frame of Schlieren images of a pre-chamber case with 50% methane hydrogen mixture at an initial pressure of 1 atm and with the main chamber coupled shows clearly the shock waves generated upon the diaphragm rupture in Fig.C.7. This test is conducted at atmospheric pressure and temperature without any fuel in the main chamber.

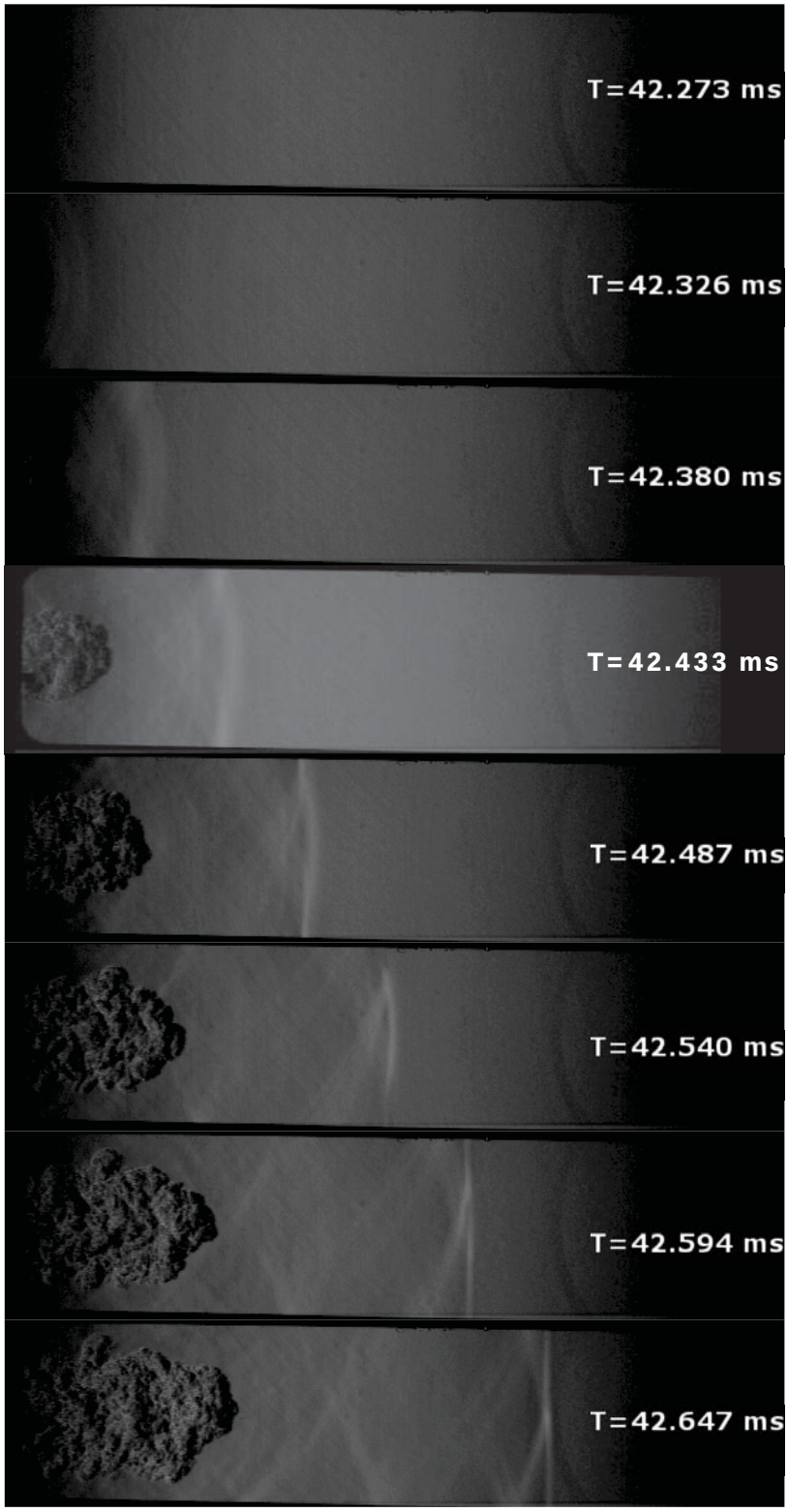


Fig. 3.5.: Pre-chamber jet penetration into the main chamber.Initial pressure is 1 atm, and $\phi$ =1. Time between each frame is 53 $\mu$s.

Upon diaphragm rupture a bow shock initially forms and transitions into a flat normal shockwave. At T=42.487ms the shock meets the front pressure sensor orifice and an oblique shock is formed which merges with the flat shockwave in the following frames. Looking at the gas discharge formation at the entrance of the channel, it is characterized by both radial and forward expansion into the channel. In order to estimate the jet velocity discharged from the nozzle, a transparent acrylic channel has been built that increases our observation view to the nozzle tip. Unlike the metallic chamber housing the quartz windows, the acrylic channel is fully transparent. Taking Schlieren images and analyzing the jet position through time for the same test conditions we can infer the jet velocity through time as it is discharged from the nozzle shown in Fig.3.6. The jet starts with a near sound velocity and slows down with time to less than 50 m/s after 1 ms.

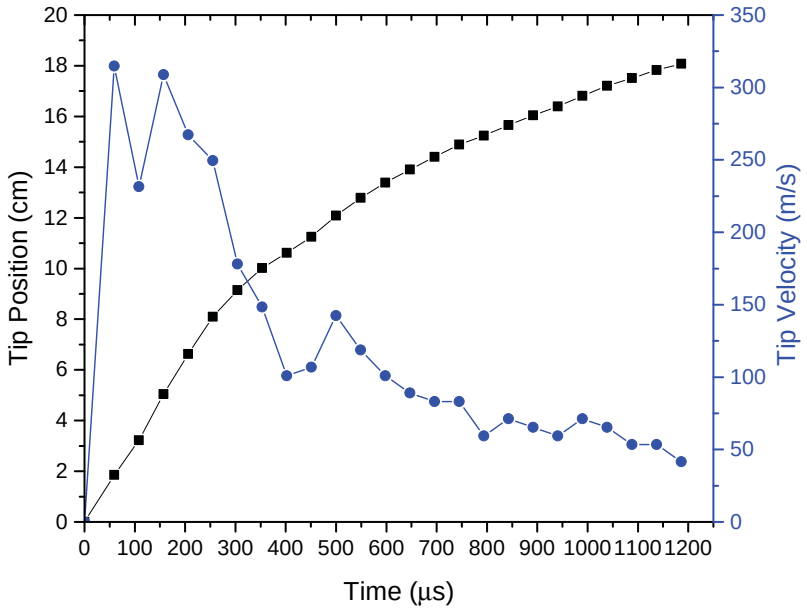


Fig. 3.6.: Pre-chamber jet gas speed into the main chamber.Initial pressure is 1 atm, and $\phi$ =1. Data collected from visual tip point propagation with time and distance.

## 3.2 Main Chamber

### 3.2.1 Main Chamber Schlieren

Schlieren images are used to understand the ignition process inside the main chamber for the three fuel mixtures cases. The images reveal the qualitative behavior of ignition, the development of the ignition kernel, the flame propagation, and combustion process. In addition, a visual ignition starting frame can be identified to be used in ignition delay calculations. A sequence of consecutive image frames starting from the ignition frame is shown in Fig.3.7 for Hydrogen, methane/hydrogen, and methane mixtures from left to right, respectively. All three test cases are for a 297K chamber temperature, a 1.5 atm pre-chamber pressure, and a 0.7 equivalence ratio in the main chamber.

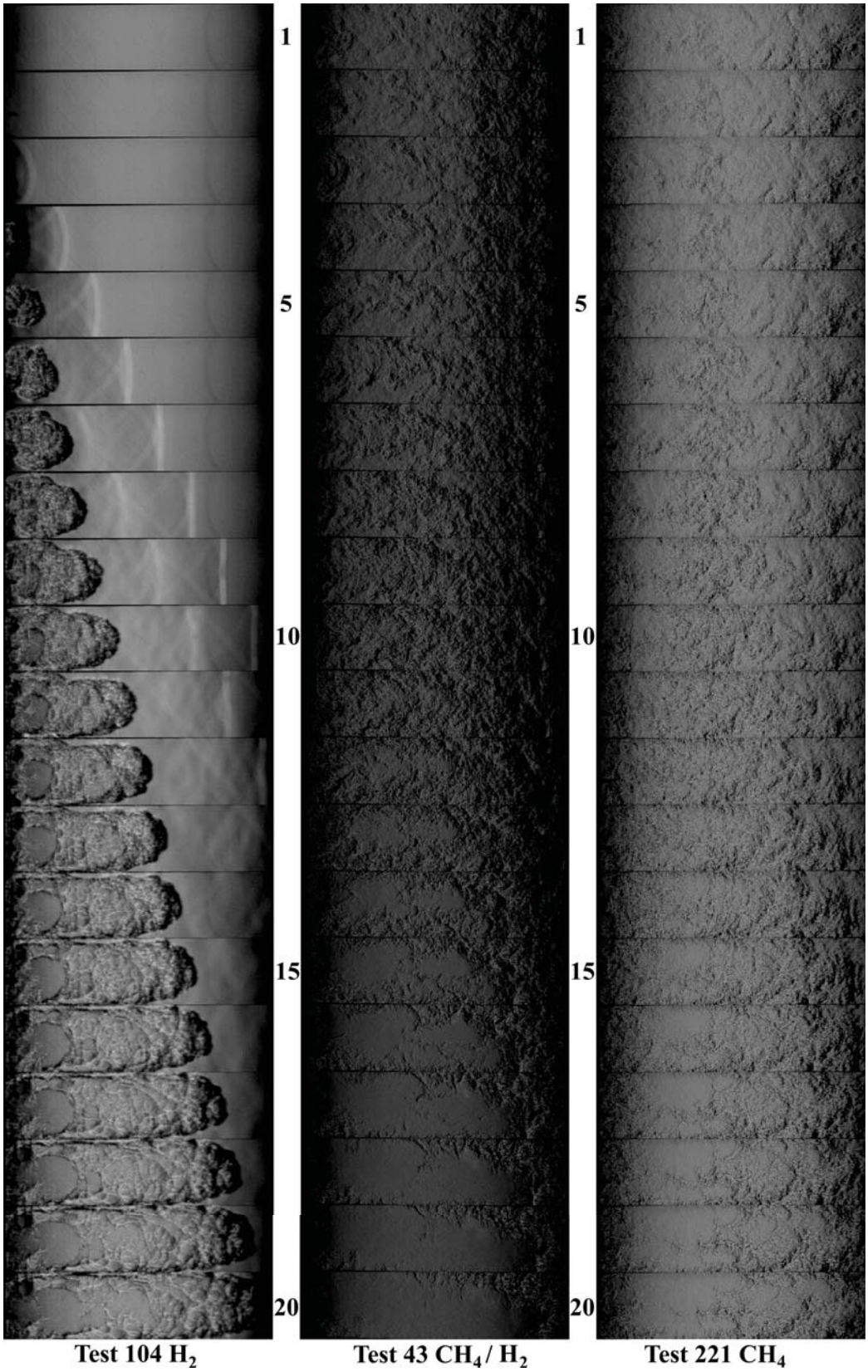


Fig. 3.7.: Capturing ignition moments; from left to right: $H_2$, 50% $CH_4/H_2$ and $CH_4$ at $\phi$ =0.7, P=1.5 atm and T =297 K. For $H_2$ and $CH_4$ time between each frame is 48 $\mu$s and total time of each image strip is 1.008 ms. For $CH_4/H_2$ time interval between frame is 54$\mu$s and total time of image strip is 1.080 ms.

The first observation is ignition occurs very early in the case of hydrogen as soon as the jet penetrates the main chamber while ignition happens at a later stage when the jet is fully expanded in the main chamber for the methane/hydrogen, and methane mixture cases. Hence methane/hydrogen behavior is similar to methane behavior in ignition. The second observation relates specifically to the hydrogen case. Not only do we observe a shock wave generated by the diaphragm rupture, but a combustion generated shockwave follows behind the rupture shock wave as can be seen in frame 7, 8 and 9. (with frame 1 being the top frame) The third observation describes the similar flame propagation process in the methane/hydrogen and methane mixture cases. Looking at the methane/hydrogen frames in the middle: an ignition kernel is developing from frame one, expanding slowly, reaching a critical size at frame 11, and suddenly pushing away the surrounding gases, leaving a relatively empty area behind. This is defined as a successful ignition for the experiment. A fourth observation can be made about how fast the gases are expanding upon ignition comparing methane/hydrogen with methane alone. Quickly looking at the last frame for both test cases, we notice a greater amount of residual gases in the methane cases on the right, compared to the methane/hydrogen channel which is relatively empty. Hence we can infer that methane combustion and flame propagation is slower than methane/hydrogen mixtures.

The same set of images was compiled for the high temperature case of 500 K, with a prechamber pressure of 1 atm and an equivalence ratio of 1. Hydrogen, methane/hydrogen, and methane are shown from left to right respectively in Fig.3.8.

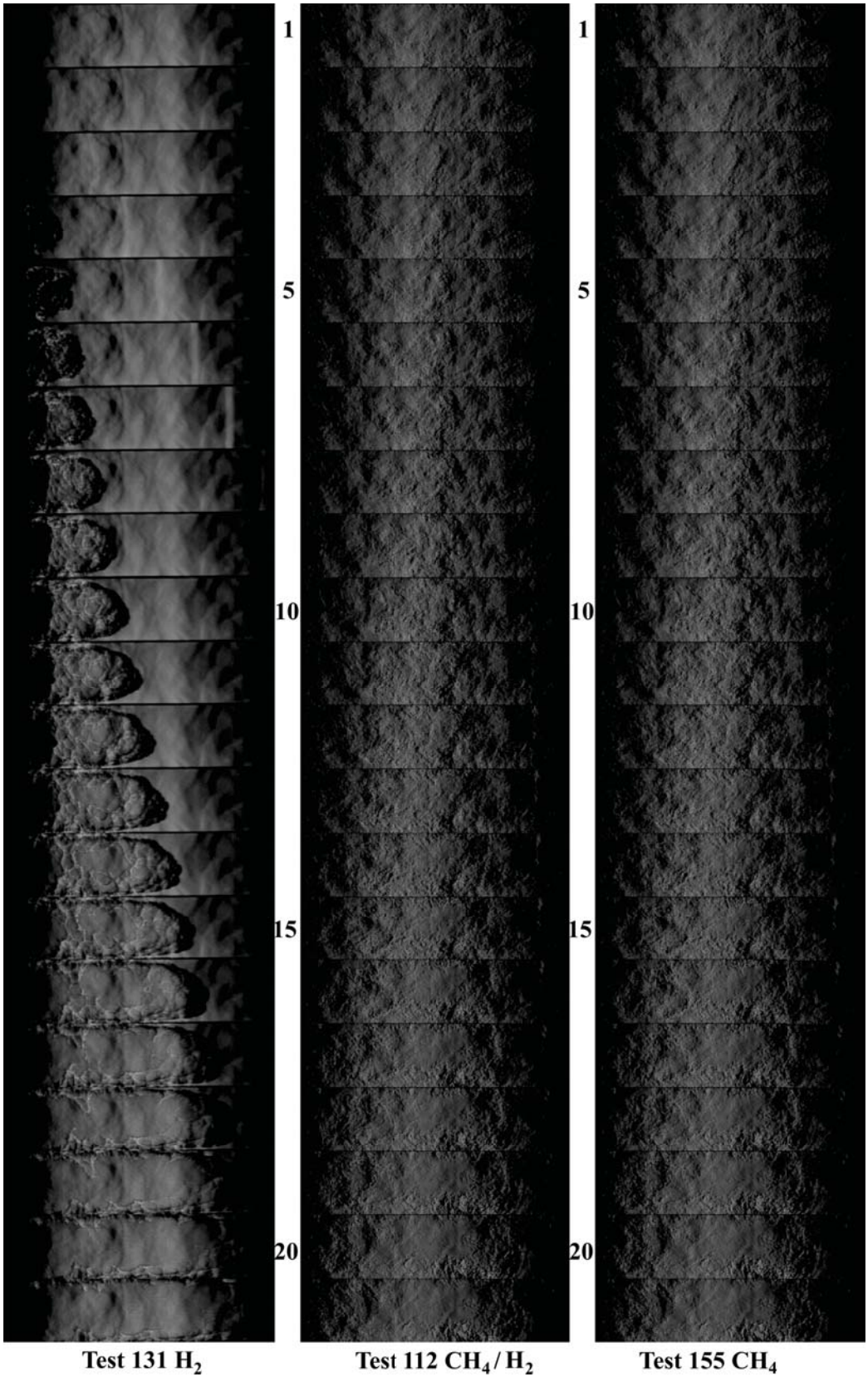


Fig. 3.8.: Capturing ignition moments; from left to right: $H_2$, 50% $CH_4/H_2$ and $CH_4$ at $\phi$ =1, P=1atm and T =500 K. Time between each frame is 48 $\mu$s and total time of each image strip is 1.008 ms.

The same observations can be made about the hydrogen case, except that the shock waves are less visible. Obtaining clear crisp Schlieren images is more challenging at high temperature because of the natural heat convection effect of the ambient 500 K channel which can be seen in the background. Also the same observations can be made for the hydrogen/methane and methane cases in terms of general qualitative behavior.

In an effort to understand the combustion behavior in the complete channel a collage of two experiment images has been made. One set of images focusing on the front part of chamber from one experiment Test 107, and the second set of images on the right focusing on the back part of the chamber from a different experiment Test 94. Both tests are done under the same conditions with initial temperature of 297K, a pre-chamber pressure of 2 atm and an equivalence ratio of 0.7. The test fuel for both experiments is Hydrogen because it has a much higher flame speed which limits the number of frames in order to show significant behavior. If using methane as an example, the number of images would be much greater than the 23 images shown in Fig.3.9.

The frame interval between each picture is 48 microseconds. However the starting points of the images are different. The timing was chosen in order to provide the best continuity between the flame propagating after the end of the front window side, and entering the back window side. Care was taken into matching the shock wave traveling from the window from the left to the window on the right. The final total image product gives us an insight into what is occuring inside the whole channel length. Particularly counter intuitive is how little action happens in the front window after the bulk of the flame has propagated to the back of the channel. Many observations can be made about the hydrogen flame in the right window of Fig.3.9:

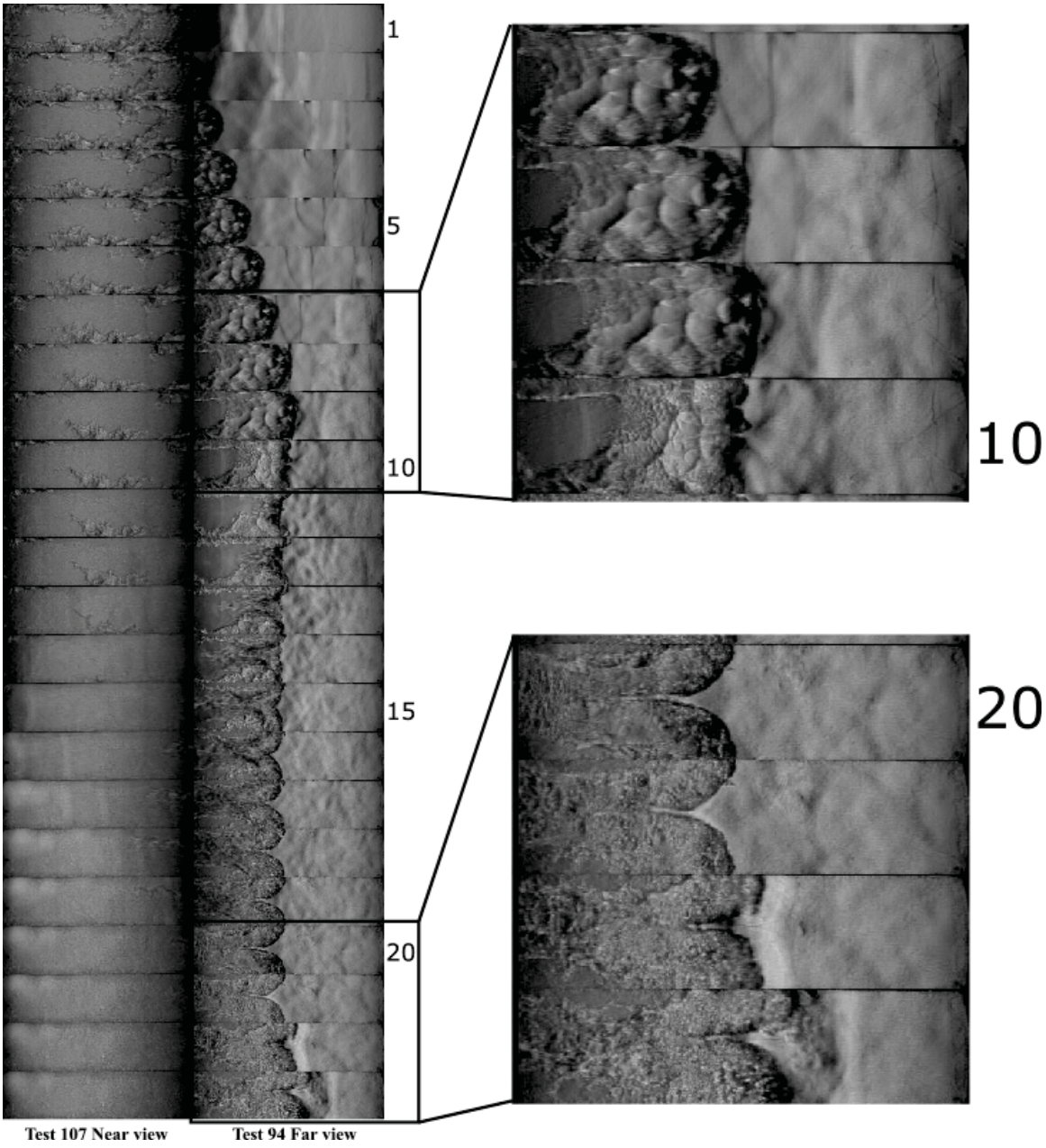


Fig. 3.9.: $H_2$ combustion in complete channel length. Left shows the front window and right shows the back of the chamber from two different tests run at the same conditions with front and back observation window.$\phi$ =0.7, P=2atm and T =297 K. 48$\mu$s interval.Total 1.104 ms.

1. First focusing our attention on shock wave behavior:

   (a) Two traveling shock waves one from the rupture diaphragm and followed by another from the initial ignition of hydrogen after the hot jet enters the channel, can be seen in frame 1 and 2.

   (b) The first shockwave gets reflected by the wall in frame 3. An oblique shockwave is generated at the hole location of the air inlet valve from the second shockwave.

   (c) When the second shockwave hits the end wall, the reflection is in the form of an X shape. This is due to machining imperfection at the corners of the channel which can be seen in frames 5 to 11.

2. When the reflected shockwave hits the flame in frame 9, it alters the combustion behavior considerably:

   (a) Looking at the combustion cell size before frame 10, they can be estimated at 0.5 inch. After the shock hits the flame front, it breaks up in multiple smaller cells, increasing the surface area of the flame, and increasing the heat release rate. The estimated smaller combustion cell size after the shock is smaller than 0.05 inch. This can be seen in frames 10 to 14.

   (b) What follows is a violent explosion which starts by the deformation of the flame front into a tulip shape flame as can be seen in frame 15 to 21.

   (c) At frame 22, the combustion accelerates into an explosion and generates a shockwave. Subsequent frames not shown in Fig.3.9 , show an abrupt consumption of all the remaining fuel, with rapid oscillation that can be seen with a traveling shockwave across the channel.

### 3.2.2 Fueling And Mixing

Methane and hydrogen are both lighter than air and thus tend to rise up in a container with air. A Schlieren image of the fueling process in the main chamber was captured in order to shed light on the fueling process. This was done after a set of experiments showed that ignition location tends to start in the top wall of the channel leading to concerns about adequate mixing of the fuel and air in the main chamber. Fig.3.10 shows three consecutive shots of methane being injected into the main chamber by the mass flow controller.

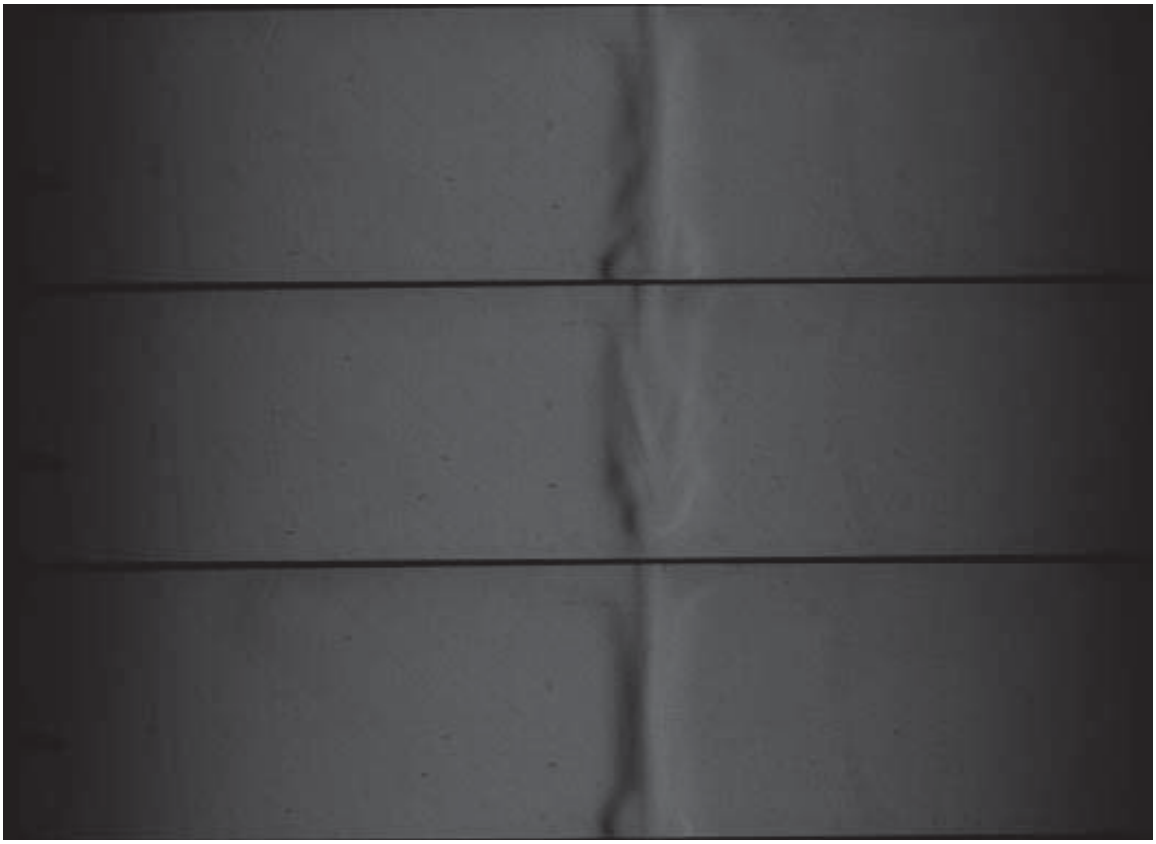

Fig. 3.10.: $CH_4$ fueling schlieren images showing buoyancy effect of the lighter methane gas going up towards channel top wall. 48$\mu$s interval.

The interval between each image is 48 micro seconds. The jet of fuel impinge on the bottom wall of the channel as can be seen in frame 1, and rise up from both

sides to the top of the channel as shown in frame 2. Upon reaching the top channel the two jets are diverged to the right and to the left of the channel staying close to the top wall.

The methane jet behavior is explained by the buoyancy effect due to different density of air and methane as expected. A question remains as to the adequate mixing of the fuel and air to initiate combustion. The molecular diffusion process controls the mixing process through binary diffusion between methane and air. Starting from the published binary diffusion coefficient by Marrero & Mason. [29] and Kestin et al. [30] and doing a dimensional analysis [31], we can write the Binary diffusion coefficient

$$\mathcal{D} \propto \frac{Area}{Time}$$

Note that in our case the area is composed of the height of the channel from top to bottom, times the length of the channel. An estimate of the time required for complete diffusion can be calculated:

Table 3.1: 1st order approximation of time needed for full diffusion in the above binary systems

| **Binary System** | $\mathcal{D}$ $(cm^2/s)$ | **Time (s)** |
|---|---|---|
| $CH_4/Air$ | 0.106 | 1426 |
| $H_2/Air$ | 0.773 | 195 |

The time required for complete diffusion calculated in the table above means that our experiment fuel air mixture is not homogeneous based on diffusion alone, since our mixing time varies from 10 to 20 seconds maximum. This analysis does not include any turbulent mixing behavior from the fuel jet into the stagnant air in the main chamber which will decrease the mixing time required for a complete homogeneous mixture. Taking a long time for mixing is not feasible in the current experiment configuration due to high temperature air that cools down quick. If

further high temperature experiments need to be performed in the future, a premixed mixture of fuel and air can be injected in the main chamber to ensure complete homogeneity.

### 3.2.3 Pressure Trace Analysis

Pressure data is recorded from 4 pressure sensors PT1, PT2, PT3 and PT4 as shown in Fig 2.3. Throughout this report PT1 is labeled Pre as the prechamber pressure, PT2 is labeled near as the pressure of the front side of the chamber, PT3 is labeled far as the pressure of the back of the chamber, and finally PT4 is labeled end as the end of the chamber pressure. The pressure data collected is used in predicting the rupture moment of the diaphragm, the initial shock speed, to confirm the visual ignition moment from the camera, calculating peak pressure and oscillation frequency in the main chamber.

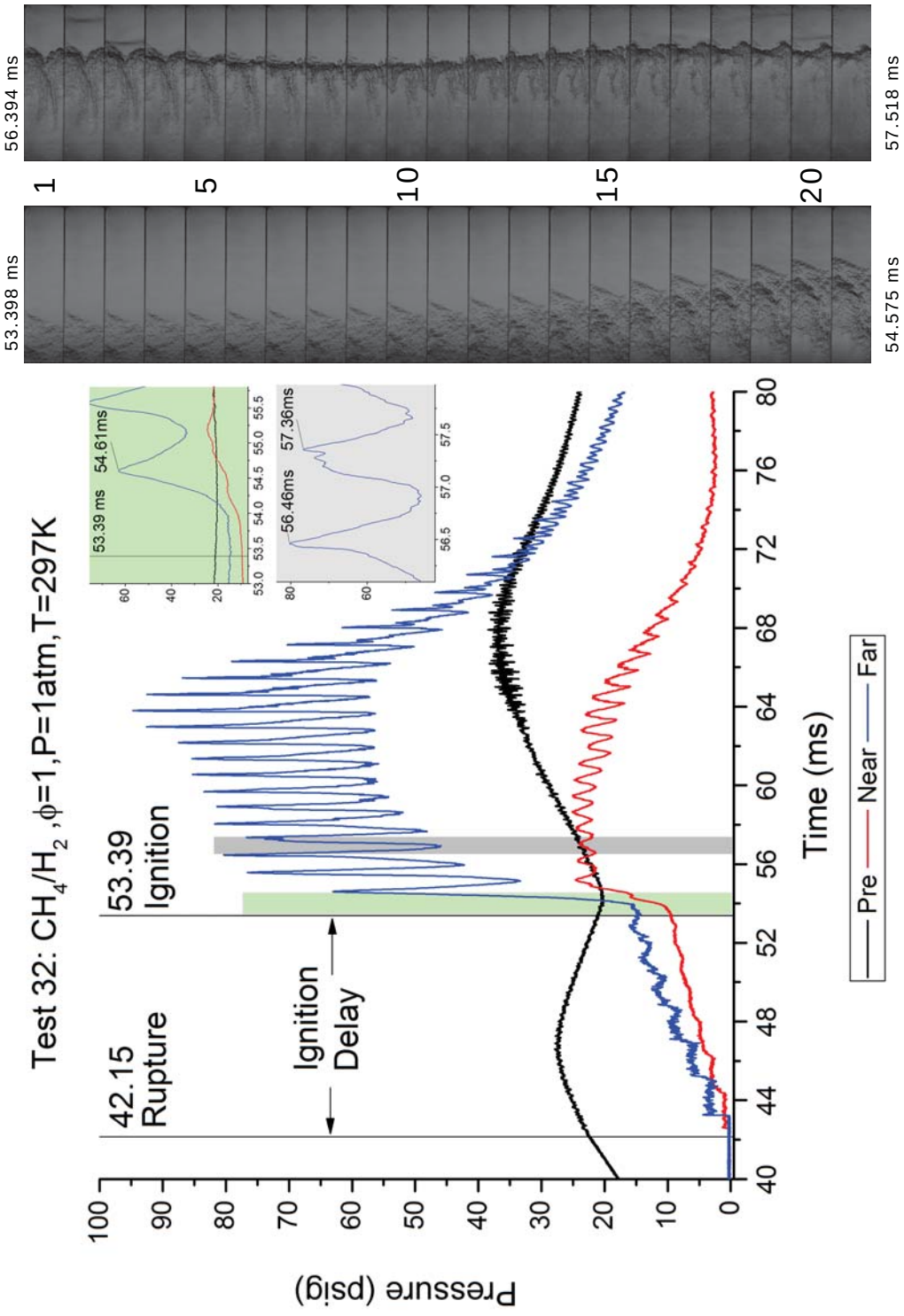


Fig. 3.11.: $CH_4/H_2$ Left shows rise in pressure associated with the green area and right shows the associated schlieren images for the green and grey area.$\phi$ =1, P=1atm and T =297 K. 54$\mu$s interval.

A typical pressure trace is shown in Fig.3.11 for Test 32 of Methane/Hydrogen at an equivalence ratio of 1, a temperature of 297K and a pre-chamber initial pressure of 1 atm.

A description of the pressure trace evolution through time can be generalized to the other experiments as follows:

1. Initial shock wave propagation phase:

   Looking at the far pressure trace from 42 ms to 53 ms, 6 successive shock waves raise the main chamber pressure to 15 psig before the onset of ignition. Looking at the near pressure trace we notice the same number of shockwave with smaller amplitude because of the dampening effect of the infinite tube mounting configuration. From the 1st shockwave rise of both the far and the near pressure trace we can calculate the shock wave speed since we know the distance between the sensors. At the same time, looking at the pre-chamber pressure trace we notice that small disturbances starts after 42.15 ms indicated by the vertical line. This increases the confidence in the rupture time calculations estimated from the initial shockwave speed.

2. Ignition development phase:

   From 53.398 to 54.575 ms ignition develops and expansion of the gas accelerates and pushes backs against the back end wall resulting in a rise in the far pressure sensor. To confirm that the rapid rise is related to ignition, a set of Schlieren images depicting the time frame highlighted in green on the graph. Left frames 1 to 21 shows a rapid expansion of the gas which is directly correlated to successful ignition and combustion as shown in the pressure trace rise in the green highlighted area.

3. Oscillation and completion phase:

   After the initial pressure build up from ignition, the combustion transitions to a rapid oscillation while continuing the upward overall pressure rise trend to

64ms before starting to decay. The oscillations are closely related to a traveling shockwave inside the combustion channel. This can be seen on the right set of schlieren images which represent the highlighted grey area including two pressure high peak and a low peak as a representative full period of oscillation. Right frame 2 shows a shock arriving at the back wall, and frame 3 shows the reflected shock. This corresponds to the maxima point of pressure on the far pressure trace in the grey highlighted area. The flame front retracts as the pressure is going down, from frame 4 to 10. And then the flame front advances to reach the next pressure peak at frame 19 which is accompanied by the return of the shockwave. Thus we conclude that the traveling shockwave is causing the oscillation inducing a corresponding bulk gas motion.

The general process outlined above is the same across the different fuel mixtures, pre-chamber pressure and initial temperature. The only variable would be amplitude of pressure and oscillation. More over looking at the pre-chamber trace between 52 and 56ms, the initial decay of the pressure is countered by the increase in pressure from ignition, which causes the pre-chamber pressure to rise up again. Without ignition the pre-chamber pressure would have continued its decay. This means that the two chambers are interconnected and leakage is minimal hence not affecting the transfer of gases in both direction. An additional observation is the change in the shape of the flame due to interactions with shock waves traversing in either direction. In the first five frames of the rightmost set of Schlieren images, a shock wave travels rightward from the hot side of the flame and emerges on the cold side. After reflection at the wall, it then travels leftward through the flame. Shock-flame interaction causes deposition of baroclinic vorticity on the flame and stretches it to produce a classic 'tulip' shape that can be seen in these frames. Generally, shock waves are not observed clearly in the hot and turbulent burned gas. The tulip flame shape is also observed in test cases using pure hydrogen fuel.

### 3.2.4 Initial Shock Speed

The initial shock speed is calculated by taking the time difference in the first shock rise between the near pressure trace, and the back pressure trace as explained in the previous section. The calculated theoretical isentropic discharge speed is in good agreement with the visual shock speed estimation from the Schlieren images. As a reminder the term initial shock speed, means the speed of the shock generated after diaphragm rupture. Subsequent shock reflection, or later shock oscillation may have significantly different shock speed.

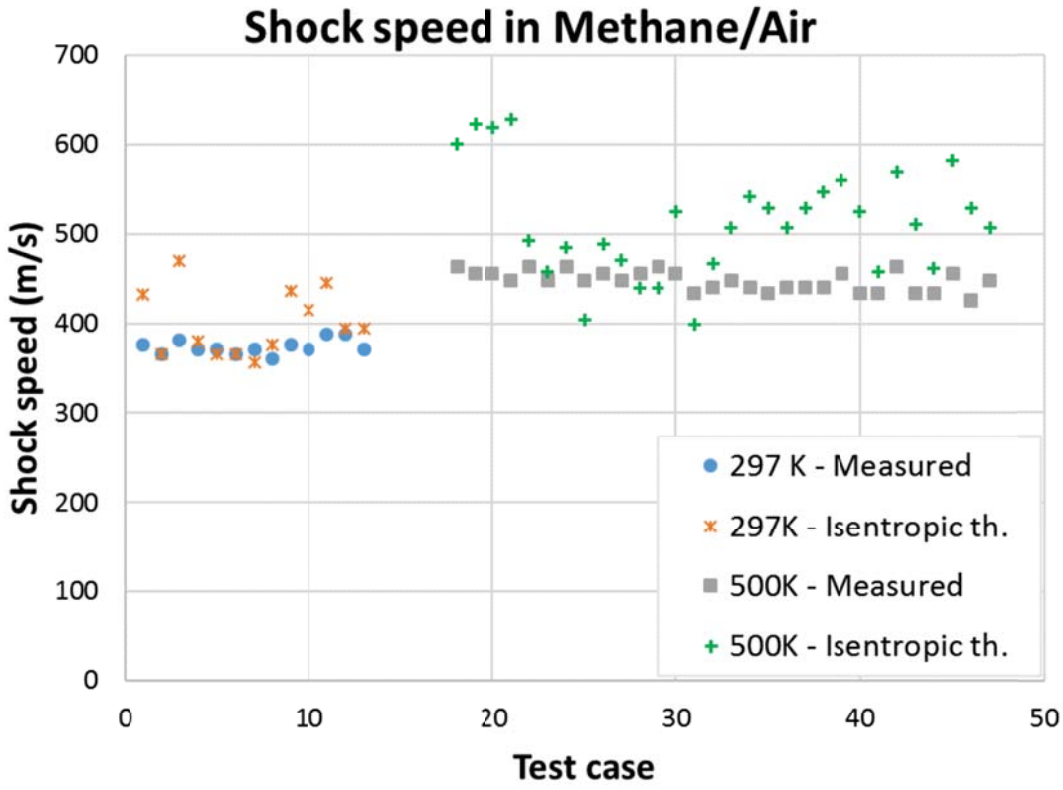


Fig. 3.12.: Initial shockwave speed after diaphragm rupture calculated from pressure sensors timing for $CH_4$ at 297K and 500K compared to isentropic theoretical shock speed calculated from pressure ratio (between rupture pressure and mixture initial pressure)

As expected the shock speed increases with temperature since the speed of sound is proportional to temperature. The graph in Fig.3.12 shows shock speed for methane test cases at two different temperatures. The average measured shock speed for test cases at 297K is 373 m/s and 446m/s for test cases at 500K. An isentropic speed based on the pressure ratio derived from the rupture pressure is also plotted for the 297K and the 500 K. Although there is an expected variation between the isentropic theoretical discharge speeds because actual conditions are not isentropic, the difference can be attributed to shock speed measurement errors, temperature drifts, and difference between actual discharge in the nozzle which is not isentropic.

### 3.2.5 Combustion Pressure Wave Frequency

The combustion generated pressure waves frequency has been calculated for each test cases when possible using the time interval between two consecutive peaks directly following the peak pressure point of the far pressure trace. The list of the combustion oscillation frequency can be found tabulated in the appendix. It was found that it varies between 700 Hz and 2700 Hz and correlates directly with a traveling acoustic wave through the channel.A more in depth analysis can be found in Paik [15].

## 3.3 Ignition Delay Results

Ignition delay is defined as the delay between the pre-chamber hot jet rupturing the aluminum diaphragm and the onset of ignition. The diaphragm rupture moment is calculated by the method outlined in Paik [15]. Using the initial shock speed and knowing the distance between the diaphragm and the back pressure sensor it is possible to deduce the time required for the shock wave to travel from the diaphragm to the back pressure sensor. Ignition delay is then defined as $T_{ID} = T_{ignition} - T_{rupture}$

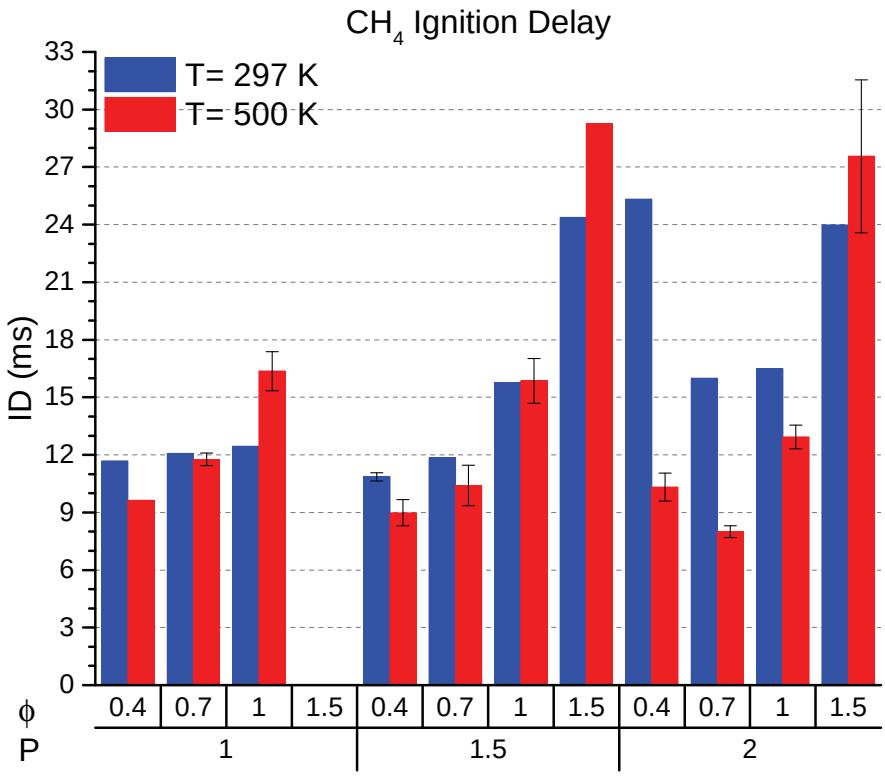


Fig. 3.13.: Average ignition delay for methane

An analysis of ignition delay is performed on methane, and methane/hydrogen fuels for both low and high temperature. Hydrogen ignition delay was challenging to quantify visually because of its fast ignition under 2ms. In most cases hydrogen was igniting as soon as the hot jet tip enters the main chamber, which made it difficult to point the precise ignition time. Also looking at pressure trace of hydrogen tests puts the ignition under 2ms and as low as 0.6 ms. The ignition delay results presented in the following figures are based on visual ignition identification using the Schlieren images. The results are in good agreement with pressure trace steep rise ignition region. Each column represents an average of the tests performed under the specified conditions. For example for Fig3.13 at a pre-chamber pressure of 1.5 atm, and equivalence ratio of 0.7, ignition delay is roughly 12ms at T=297K, and

roughly 10ms at T=500K. This number is an average of multiple tests performed under the same conditions. Standard error of the mean bars shows the variation of the sample points around the mean.If no error bar is included, this indicates that it was a single test.

Fig.3.13 shows methane fuel tests ignition delay for the 297K case, and the 500 K case at different pre-chamber pressure (1,1.5 and 2 atm) and different equivalence ratio (0.4,0.7,1,1.5). The first dominant trend is that ignition delay increases with equivalence ratio. The variation of ignition delay with equivalence ratio requires careful attention. In the process of jet formation, some unburned fuel might be transferred from the pre-chamber to the main chamber. Therefore, in the case of slightly lean mixture in the main chamber, the fuel originated from the jet would complement the mixture in main chamber and can produce locally stoichiometric regions. This process would explain having the minimum ignition delay at equivalence ratio other than 1.

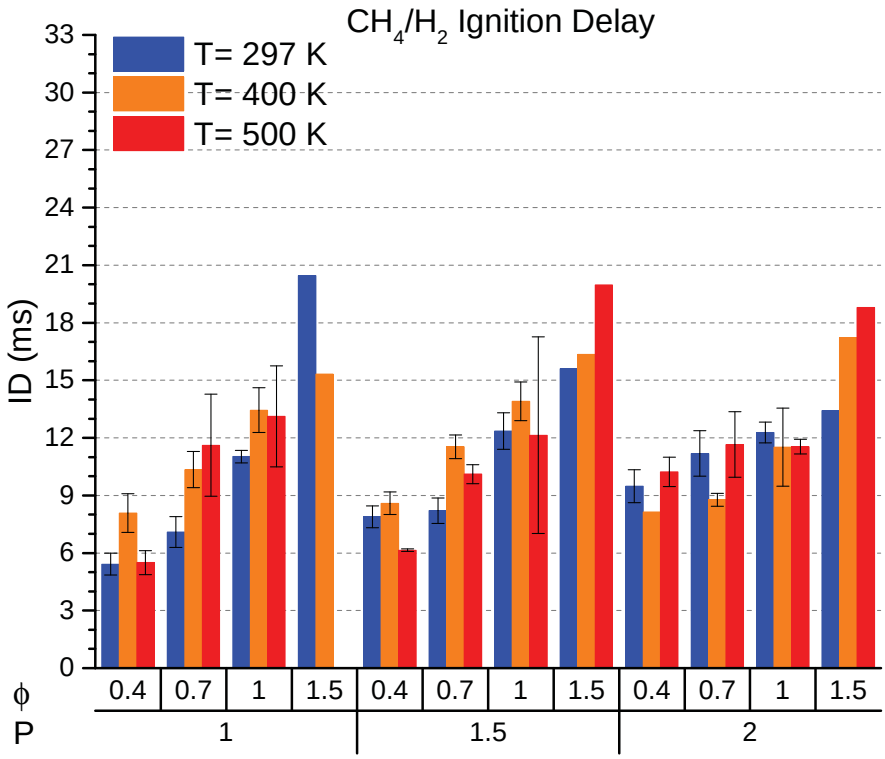


Fig. 3.14.: Average ignition delay for methane/hydrogen fuels

Plotting the same data in Fig.3.14 for the methane/hydrogen case shows a similar behavior in term of the trend of ignition delay increasing with equivalence ratio. However the effect of increasing temperature ignition delay is inconclusive.Some cases like P=2, $\phi = 1$ shows a decrease in ignition delay, and other cases like P =1.5, $\phi$ =0.7 show an increase in ignition delay. More data points are needed to determine possible correlations between temperature and hot jet ignition delay, preferably at a higher temperature. It appears that equivalence ratio effect, and the the physical mixing of the pre-chamber jet with main chamber mixture, is masking the effect of temperature.

Looking more closely at the fuel effect by plotting ignition delay for similar cases of the two fuels on the same graph we notice that for the 297 K Fig.3.15 temperature case, the methane/hydrogen mixture has a lower ignition delay compared to the pure methane mixtures across all cases.

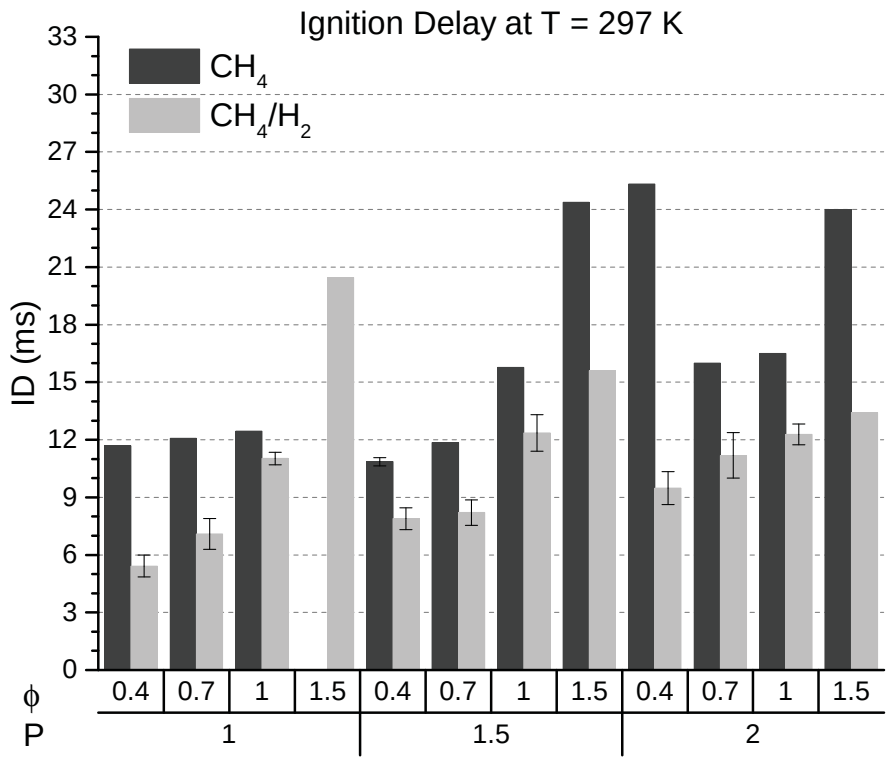


Fig. 3.15.: Average ignition delay for methane and methane/hydrogen fuels at T=297K

Looking at the 500K temperature case Fig3.16, methane/hydrogen mixture ignition delay is still smaller than methane ignition delay, but with a narrower difference. Ignition delay positive trend with increasing equivalence ratio still holds true.

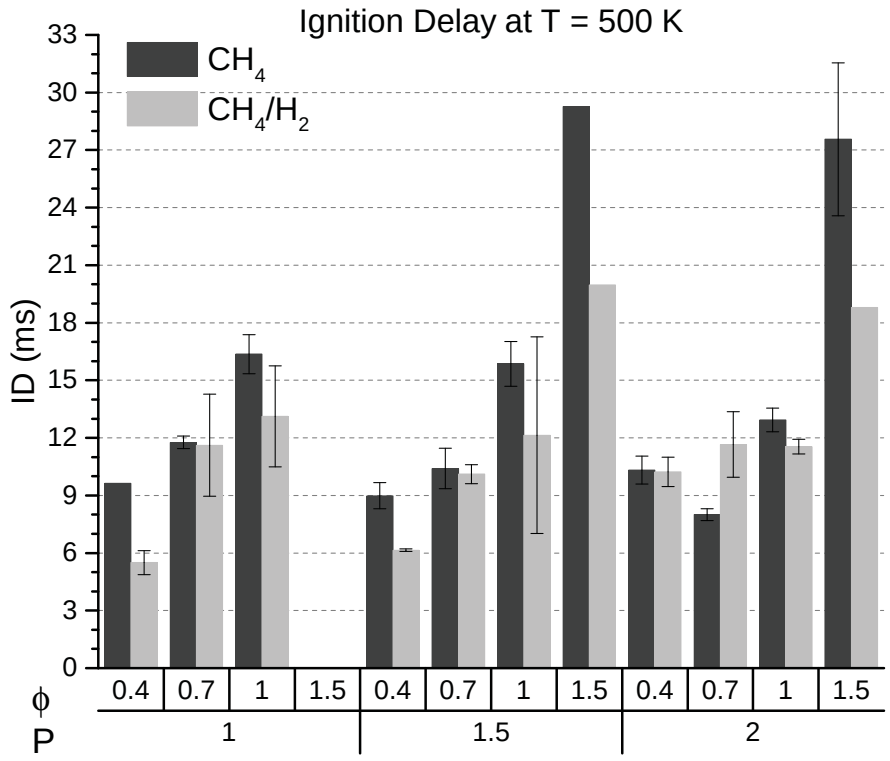


Fig. 3.16.: Average ignition delay for methane and methane/hydrogen fuels at T=500K

A few cases with a significant standard error of the mean like P=1.5, $\phi$ =1, should be retested to increase the sample size and establish more confidence in the data points.

## 3.4 Regression Analysis

Collecting many experimental data point creates the challenge of how best to interpret the data. As seen in the Fig.3.15 and Fig.3.16, it is hard to derive a general conclusion regarding the overall effect of raising the temperature to 500K on ignition delay of methane, and methane/hydrogen. In this section, a statistical analysis of the data aims to provide more insight to interpret the main effects of different variables (Pre-chamber pressure, initial temperature, equivalence ratio, and fuel)

In the previous section, we showed that the relationship between ignition delay and temperature was not obvious. An additional set of experiments have been performed at an initial temperature of 297 K with the main chamber initial blend at an equivalent density compared to the high temperature tests at 500 K. Results from same density experiments are reported as $CH_4/H_2 - E$ in the following graphs.

### 3.4.1 Introduction

A linear regression model assumes a linear relationship between a set of input variable $[x_1, x_2, x_3...x_i]$ and the output variable $y$. The relationship is modeled through the addition of a residual error term $\epsilon$ as shown in this equation [32] :

$$y = k_0 1 + k_1 x_1 + k_2 x_2 + ...k_n x_n + \epsilon \tag{3.1}$$

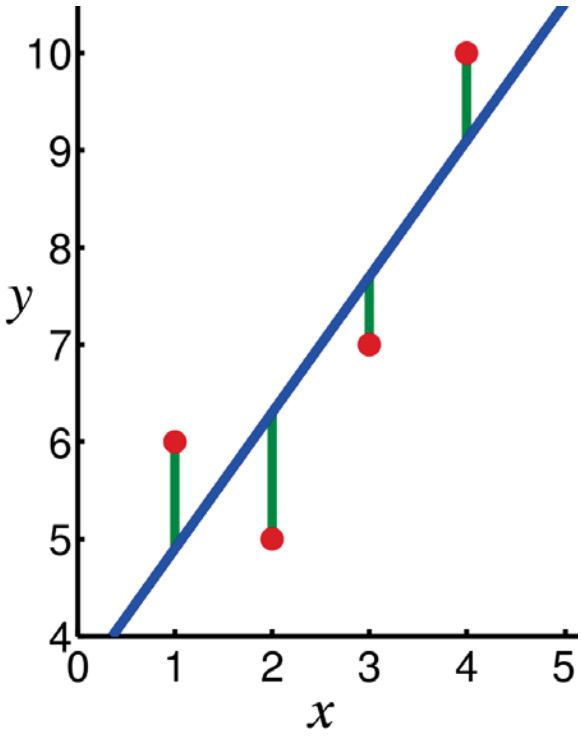


Fig. 3.17.: In linear regression, the observations (red) are assumed to be the result of random deviations (green) from a underlying relationship (blue) between the dependent variable (y) and independent variable (x). [32]

### 3.4.2 Regression Model

Minitab statistical analysis software was used throughout the regression analysis presented in section 3.4. A total of 144 tests is used to build the regression model. These tests included $CH_4$ at 297K and 500K; and $CH_4/H_2$ at 297K, 400K, and 500K; and $CH_4/H_2 - E$ at 297K. In all tests pre-chamber initial pressure was varied (1,1.5,2 atm) and equivalence ratio was varied (0.4,0.7,1).

Plotting the ignition delay data of the 144 samples in a probability plot in Fig. 3.18 shows a good fit with a Gaussian (Normal distribution). This can be confirmed by looking at the $P - Value < 0.005$ for the samples. The average ignition delay for all samples was 10.86ms, and the standard deviation was 4.6ms.

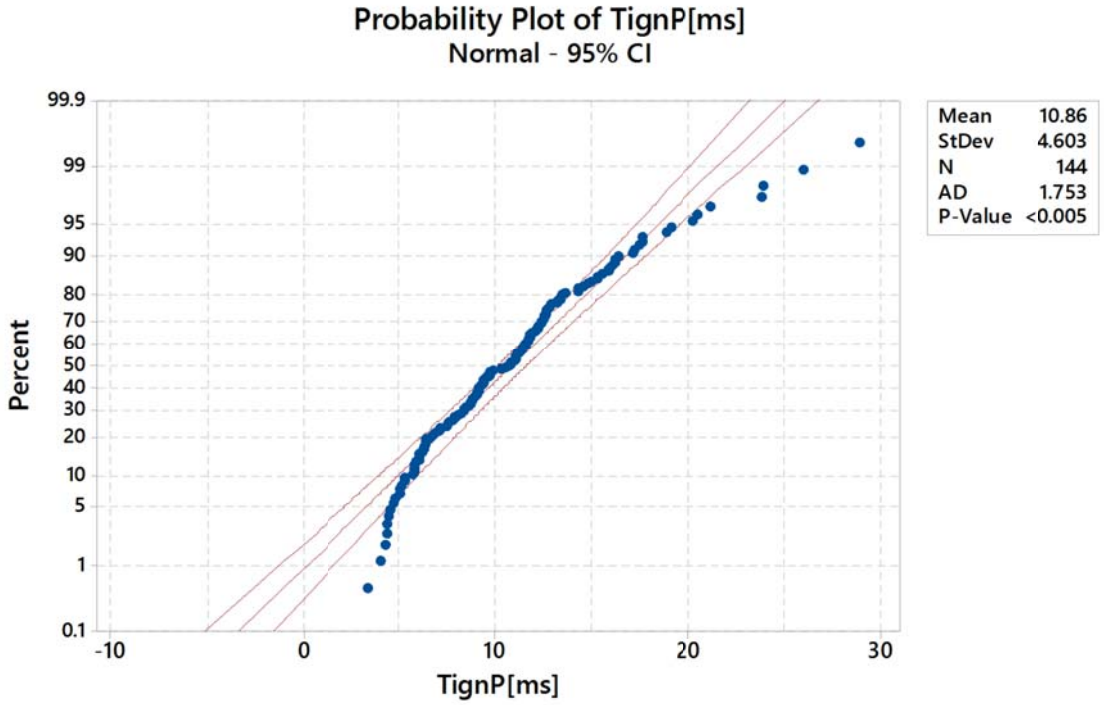


Fig. 3.18.: Ignition delay probability distribution for 144 tests. A P-Value $< 0.005$ indicates that the sampled data can be fitted as a Normal (or Gaussian) distribution

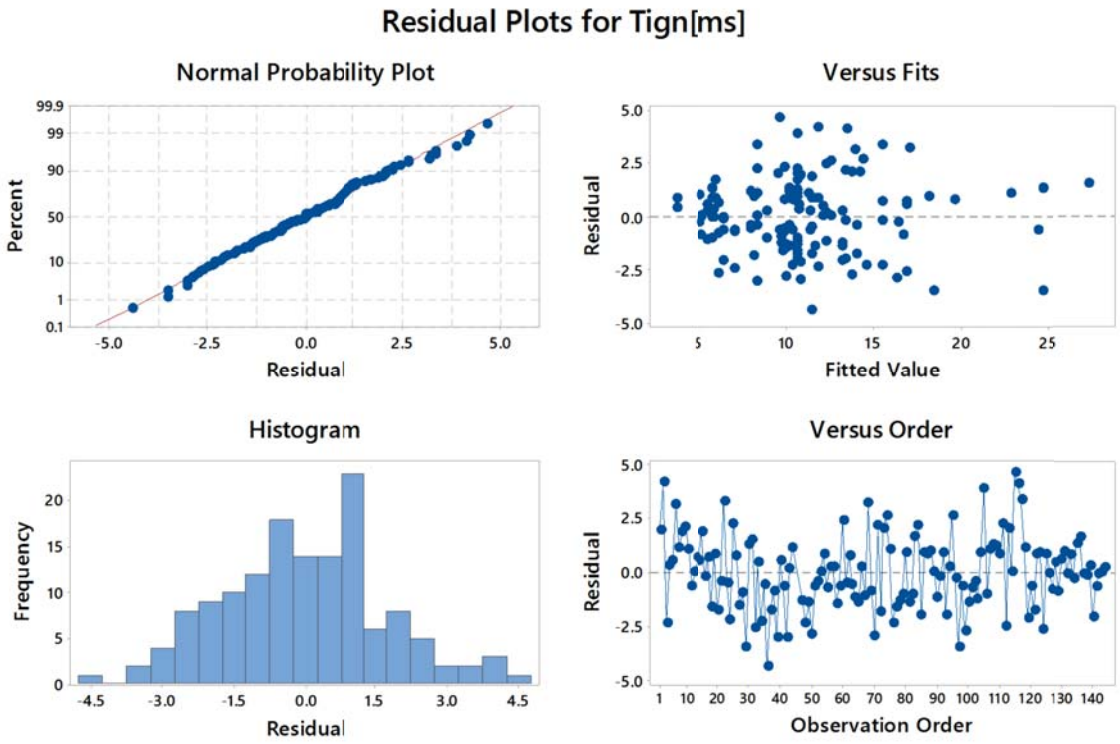


Fig. 3.19.: Residuals distribution from the regression analysis.All residuals are within plus or minus 4.5ms, with the majority between minus and plus 1.5ms.

The residual error term of the linear regression model is shown in Fig. 3.19. The residual error follows a normal distribution as can be seen in the top left and bottom left plots. The top right plot shows the fitted value and its corresponding residual error. The fitted value residual error is ranging from +5 to -5ms. The bottom right plot shows the residuals in function of the observation test number which helps identify any non ordinary residuals related to specific tests sequence.

An ANalysis Of VAriance (ANOVA) is performed on the regression model evaluating each of the model terms contribution and testing the null hypothesis through the P-value. The main take away from Table 3.2 is the list of model terms P-value testing. All the terms have a $P - value < 0.005$ (makes them statistically significant) except $Phi * Phi, Phi * T, P * T * T$. However the terms were included

in the model because they yielded a better R-Square value. More information can be found about how to interpret ANOVA table on the Minitab website.

Table 3.2: Analysis of variance - ANOVA on the regression model

| **Source** | **DF** | **Seq SS** | **Contribution** | **Adj SS** | **F-Value** | **P-Value** |
|---|---|---|---|---|---|---|
| ***Regression*** | 18 | 2577.35 | 86.07% | 2577.35 | 42.23 | 0.000 |
| P | 1 | 89.93 | 3.00% | 19.32 | 5.70 | 0.019 |
| Phi | 1 | 1441.87 | 48.15% | 15.33 | 4.52 | 0.035 |
| T | 1 | 198.42 | 6.63% | 31.53 | 9.30 | 0.003 |
| Fuel | 2 | 519.27 | 17.34% | 56.00 | 8.26 | 0.000 |
| Phi*Phi | 1 | 53.60 | 1.79% | 4.77 | 1.41 | 0.238 |
| T*T | 1 | 4.38 | 0.15% | 30.81 | 9.09 | 0.003 |
| P*Phi | 1 | 15.41 | 0.51% | 51.33 | 15.14 | 0.000 |
| P*T | 1 | 17.34 | 0.58% | 13.43 | 3.96 | 0.049 |
| Phi*T | 1 | 69.86 | 2.33% | 12.92 | 3.81 | 0.053 |
| P*Fuel | 2 | 3.89 | 0.13% | 21.45 | 3.16 | 0.046 |
| Phi*Fuel | 2 | 71.46 | 2.39% | 38.96 | 5.75 | 0.004 |
| P*T*T | 1 | 15.02 | 0.50% | 11.72 | 3.46 | 0.065 |
| Phi*T*T | 1 | 17.13 | 0.57% | 15.10 | 4.45 | 0.037 |
| Phi*Phi*Fuel | 2 | 59.78 | 2.00% | 59.78 | 8.81 | 0.000 |
| ***Error*** | 123 | 417.08 | 13.93% | 417.08 | | |
| Lack-of-Fit | 47 | 219.35 | 7.33% | 219.35 | 1.79 | 0.011 |
| Pure Error | 76 | 197.73 | 6.60% | 197.73 | | |
| ***Total*** | 141 | 2994.43 | 100.00% | | | |

Table 3.3 shows a summary of how well the linear regression model fit the observed data.The predicted R-squared indicates how well a regression model predicts responses for new observations.The adjusted R-squared compares the explanatory power of regression models that contain different numbers of

predictors.S is the standard error which represents the average distance that the observed values fall from the regression line.

Table 3.3: Model summary

| S | R-sq | R-sq(adj) | R-sq(pred) |
|---|---|---|---|
| 1.84143 | 86.07% | 84.03% | 80.53% |

Finally the regression equations based on the model terms in the ANOVA table can be summarized in Table 3.4. Three equations for 3 different fuels ($CH_4$,$CH_4/H_2$,$CH_4/H_2-E$ ) are expressed in function of Pre-chamber initial pressure $P$ (1,1.5,2), equivalence ratio $Phi$ (0.4,0.7,1,1.5), and initial main chamber mixture temperature $T$ (300,400,500K).

Table 3.4: Generalized Linear Model Regression equations for 144 tests spanning 3 different fuels in function of Pre-chamber initial pressure $P$ (1,1.5,2), equivalence ratio $Phi$ (0.4,0.7,1,1.5), and initial main chamber mixture temperature $T$ (300,400,500K)

| **Fuel** | **Equation for Ignition Delay time Tign [ms]** |
|---|---|
| $CH_4$ | $-77.6+38.4P+31.4Phi+0.450T+13.17Phi\times Phi-0.000558T\times T$ $-5.09P\times Phi-0.1749P\times T-0.205Phi\times T+0.000205P\times T\times T$ $+0.000280Phi\times T\times T$ |
| $CH_4/H_2$ | $-89.3+40.7P+49.3Phi+0.450T+1.39Phi\times Phi-0.000558T\times T$ $-5.09P*Phi-0.1749P\times T-0.205Phi\times T+0.000205P\times T\times T$ $+0.000280Phi\times T\times T$ |
| $CH_4/H_2-E$ | $-88.7+38.7P+49.9Phi+0.450T-3.11Phi\times Phi-0.000558T\times T$ $-5.09P\times Phi-0.1749P\times T-0.205Phi\times T+0.000205P\times T\times T$ $+0.000280Phi\times T\times T$ |

### 3.4.3 Main Effects And Interaction Effects

Minitab can be used to investigation the overall general relationship between the independent input variables and their effect on the dependent output variable through a main effect plot. In Fig.3.20, the average ignition delay is plotted on the vertical axis in function of the input variables initial pre-chamber pressure $P$, main chamber equivalence ratio $Phi$, main chamber initial temperature $T$, and type of fuel.Two general trends dominate these plots:

1. An increase of ignition delay with the increase in equivalence ratio;
2. A decrease of ignition delay from $CH_4$ a low reactive fuel, to $CH_4/H_2$ a more reactive fuel with the addition of hydrogen, to $CH_4/H_2 - E$ which is the same fuel blend as the previous methane/hydrogen blend but with a lower overall amount of fuel/air equivalent to the high temperature experiment.
3. A moderate decreasing effect of initial pre-chamber pressure on ignition delay.
4. A weak effect of initial main chamber temperature on average ignition delay time shown with an overall increase from 300K to 400K, and then a slight decrease at 500K.

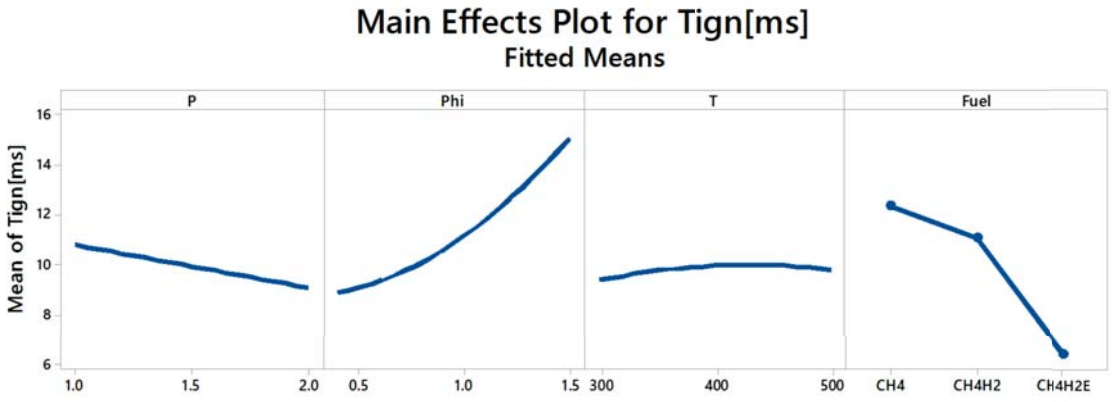


Fig. 3.20.: Variables Pre-chamber pressure P, main chamber equivalence ration $\phi$, and Fuel main relationship with mean ignition delay

An interaction plot can also be generated through Minitab showing the relationship between the interaction variables and their possible effect on the average ignition delay time. In Fig. 3.21, the first column of plots shows the terms containing a $P$ interaction with $P * Phi$ on the top, $P * T$ in the middle, and $P * Fuel$ at the bottom. The associated legend on the right shows the difference in ignition delay between the $Phi = 0.4$ (blue) and $Phi = 1.5$ (red dotted) line for the $P * Phi$ plot. Overall no major contribution for the interaction effect can be observed for ignition delay. The main driver of ignition delay is the equivalence ratio as previously seen in main effect plot.

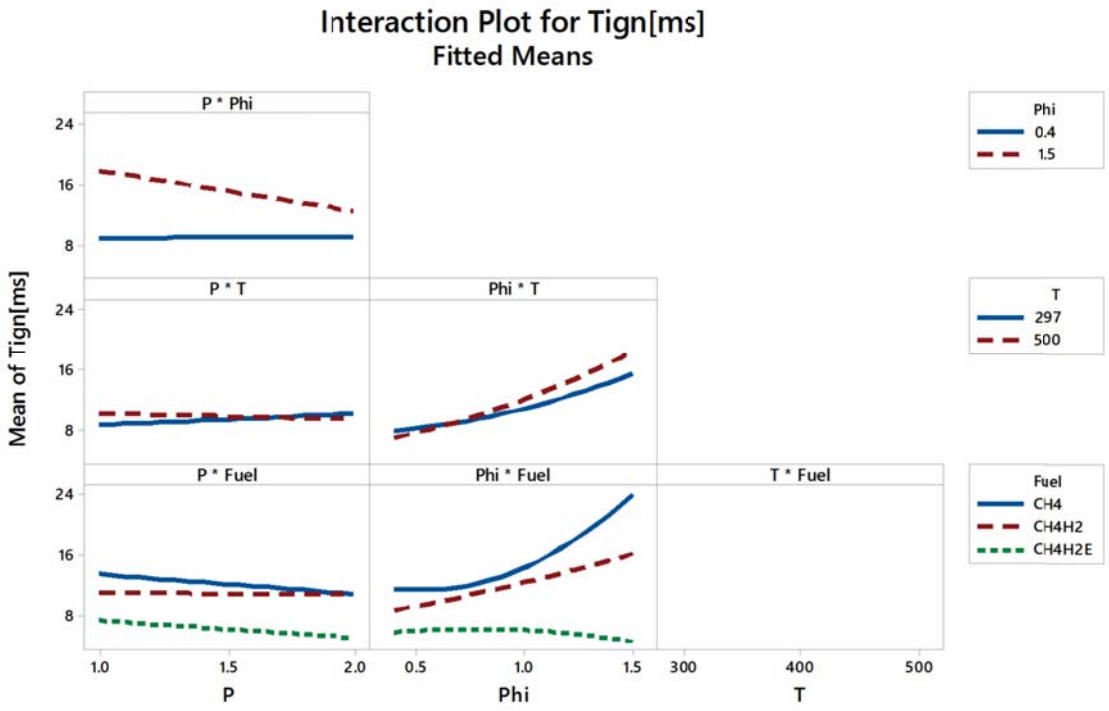


Fig. 3.21.: Graphs shows interaction of multiple variables and its effect on ignition delay

### 3.4.4 Analysis

The initial ignition delay analysis portrayed by the plots in section 3.3 did not include the additional testing at a lower main chamber mixture pressure performed to simulate the same density in the main chamber between experiments at 297K, and experiments at 500K.

Reproducing the $CH_4$ (in blue) and $CH_4/H_2$ (red) data in Fig. 3.22, and adding to it the results of the $CH_4/H_2 - E$ (equivalent density to T=500K, but tests performed at T=297K) offers a new insight into the data. Ignition delay of $CH_4/H_2 - E$ are much lower compared to $CH_4/H_2$ under the same conditions. Having less fuel and air to burn in the main chamber is resulting in a faster ignition delay overall. This indicates that the initial amount of mass in the main chamber is an important variable that needs to be considered.

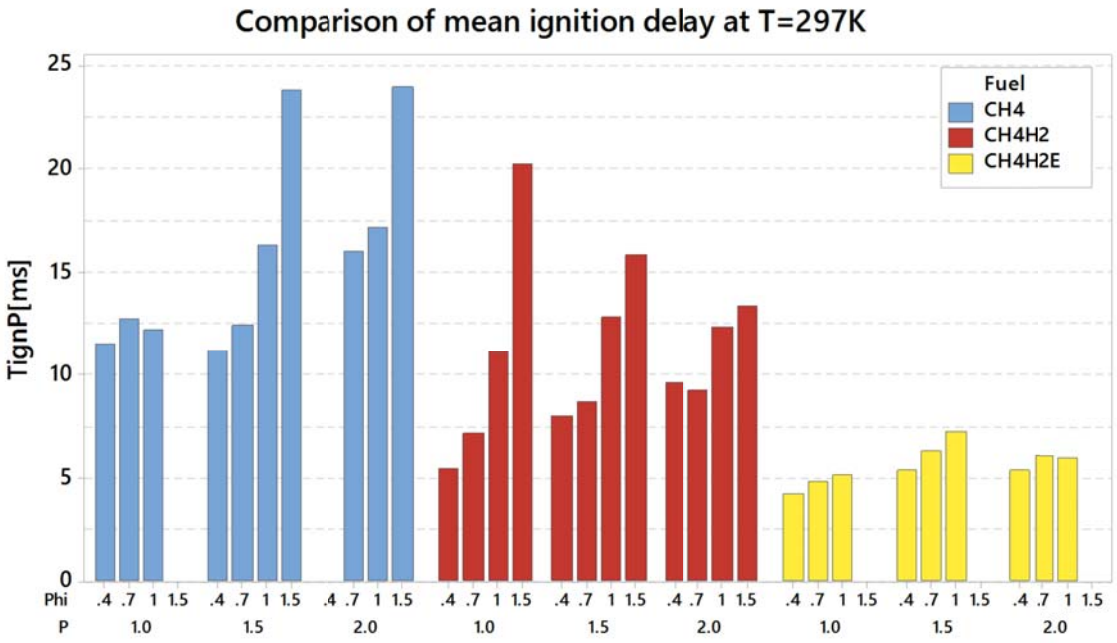


Fig. 3.22.: Mean ignition delay for each fuel at different equivalence ratio and initial pre chamber pressure for initial main chamber temperature of T=297K.

A direct comparison of the $T = 500K$ experiments (blue) to the $T = 297K$ experiments (red) at equivalent density is shown in Fig. 3.23. One would expect similar results for the two experiments, however the $CH_4/H_2 - E$ ignition delay is considerably smaller specially at $Phi > 0.7$. To summarize: fuel and air in a closed chamber at high temperature will ignite slower than the same mass of fuel and air at room temperature.

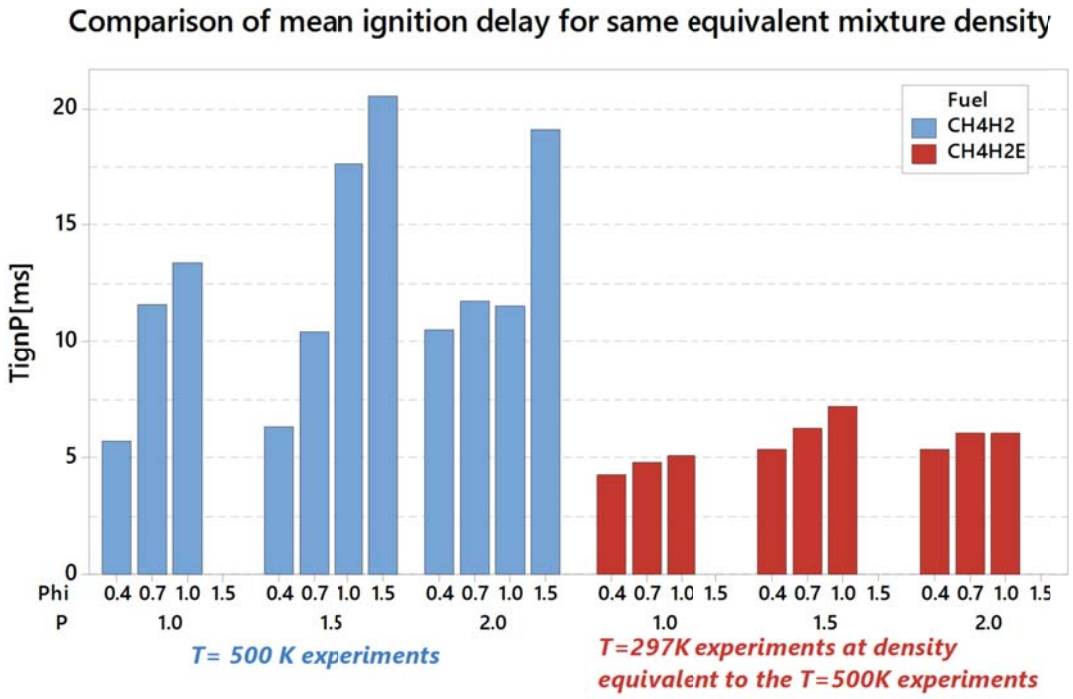


Fig. 3.23.: Mean ignition delay for $CH_4/H_2$ at T=500K and for equivalent density $CH_4/H_2$ at T=297K. The big gap between the two indicates that the mixture overall equivalence ratio has a greater effect on ignition delay compared to temperature

The main chamber total fuel/air mass is the same in both cases of T=500K and T=297K. The 297K case has the main chamber vacuumed to around 587 mbar (this corresponds to the temperature ratio of 1.68 using the ideal gas law) compared to the 500K experiments occurring at atmospheric pressure close to 995mbar.Experiments are compared at the same mass to fuel ration. In all cases the

ignition delay of the lower temperatures is significantly lower that of the higher temperatures.

This is a counter-intuitive results because based on published experimental data, chemical ignition delay decrease with temperature which is typically modeled with an Arrhenius type regression [33]:

$$\tau = A.p^a.\phi^b.X_{O_2}^c.exp(Ea/RT) \tag{3.2}$$

However this equation is limited to the chemical reaction ignition delay typically found in shock tube experiments. The hot jet ignition case is different than shock tube ignition experiments since the hot jet ignition mechanism adds physical mixing time of the pre-chamber jet with the main chamber mixture to the ignition process.

Possible explanations for the discrepancy between the high and low temperature experiments ignition delay results in Fig. 3.23 might be:

1. High temperatures of the chamber solid body, and of the air/fuel mixtures causes natural convection currents which alter the uniform mixing of the fuel with air. Possible fuel stratification to the top of the chamber due to lighter density and higher thermal gradients may also contribute to non ideal mixing.

2. Experimental error where the actual air mass calculated in the main chamber at T= 500K is not accurate. In both the T=297K equivalent density experiment and the T=500K the same amount of fuel is injected in the main chamber. In the T=297K case the main chamber is vacuumed to reach the required overall mass of fuel and air that is equivalent to the T=500K case. However this would not explain the big differences in the ignition delay results.

A summary of ignition delay data can be seen in contour plots in function of $P$ and $Phi$ as well as in function of $T$ and $Phi$ in Figures 3.24 to 3.28 The contour plot color concentration increases with equivalence ratio $Phi$ as a general conclusion for all figures.

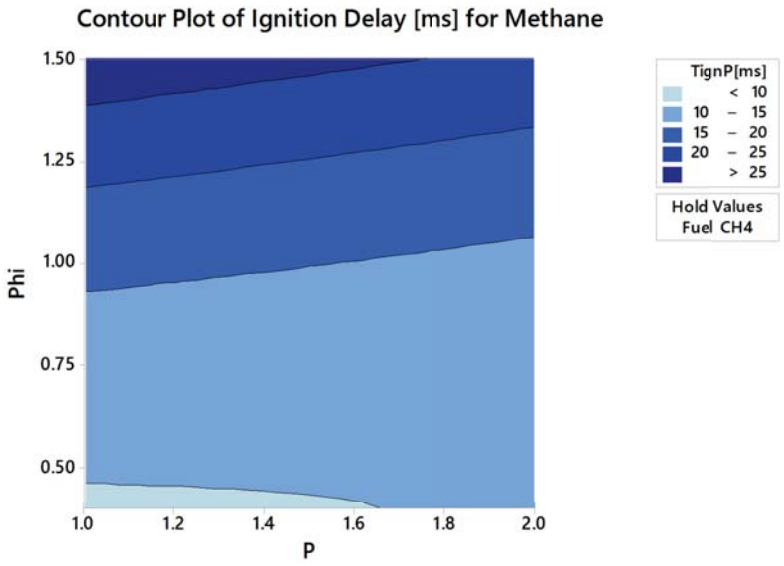


Fig. 3.24.: Contour plot showing $CH_4$ ignition delay variation with equivalence ratio $Phi$ and initial pre-chamber pressure $P$.

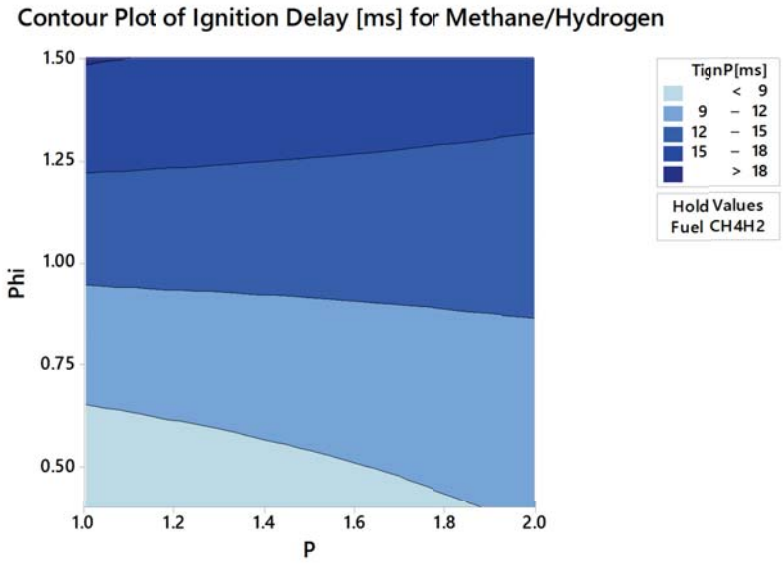


Fig. 3.25.: Contour plot showing $CH_4/H_2$ ignition delay variation with equivalence ratio $Phi$ and initial pre-chamber pressure $P$.

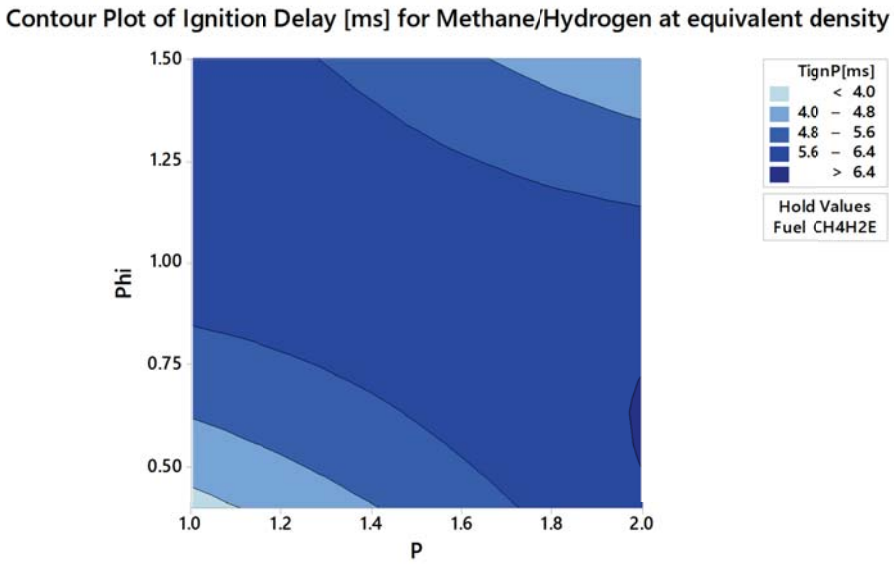


Fig. 3.26.: Contour plot showing $CH_4/H_2 - E$ ignition delay variation with equivalence ratio $Phi$ and initial pre-chamber pressure $P$.

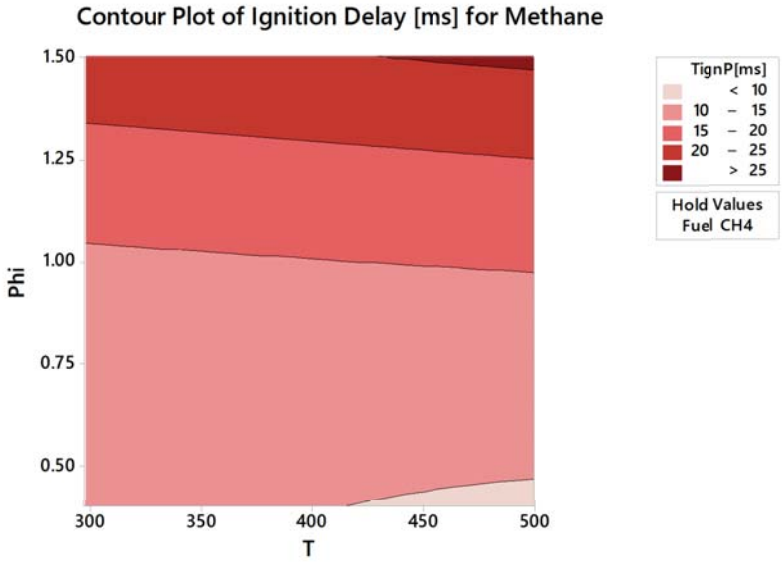


Fig. 3.27.: Contour plot showing $CH_4$ ignition delay variation with equivalence ratio $Phi$ and initial main chamber mixture temperature $T$ for an initial pre-chamber pressure of 1atm.

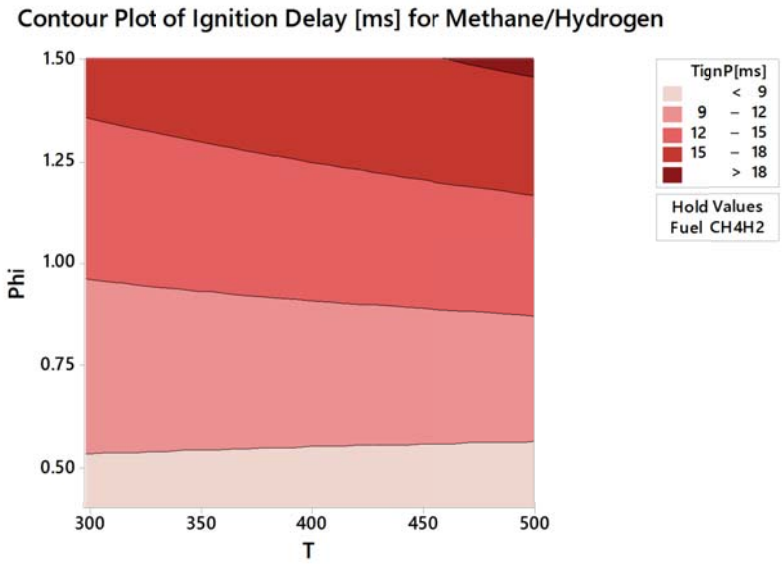


Fig. 3.28.: Contour plot showing $CH_4/H2 - E$ ignition delay variation with equivalence ratio $Phi$ and initial main chamber mixture temperature $T$ for an initial prechamber pressure of 1atm.

## 3.5 Measurement Uncertainty Analysis

The uncertainty of the experiments related to physical measurement can be summarized by Table 3.5. A total of 14.97% experiment uncertainty has been estimated factoring in: the pre-chamber fueling in $P_{pre}$; the timing bias $t_{PT}$ in picking up two point on the near pressure trace to calculate the shock speed and estimate rupture pressure; the ignition delay time frame $ID_{time}$ spotted by schlieren imaging allowing an bias error of 10 frames; the error induced in the calibration of the MFC $m_{MFC}$; the error induced in estimating the temperature of the air at the near location $T$. It should be noted that the bias error estimate is a conservative estimate of human measurement error during the experiment. The precision error is due to the measurement instrument precision. The nominal values selected for this sample calculation are for Test# 177. Uncertainty is calculated as per

$$Uncertainty = \sqrt{Bias^2 + Precision^2}$$

Table 3.5: Summary of uncertainty analysis

| Variable | Units | Nominal | Bias | % Bias | Precision | % Precision | % Uncertainty |
|---|---|---|---|---|---|---|---|
| $P_{pre}$ | psig | 7.11 | 0.100 | 1.406 | 0.001 | 0.014 | 1.41 |
| $t_{PT}$ | seconds | 0.00057 | 0.000032 | 5.614 | 0.000004 | 0.702 | 5.66 |
| $ID_{time}$ | seconds | 0.052686 | 0.00048 | 0.911 | 0.000048 | 0.091 | 0.92 |
| $m_{mfc}$ | mg | 20.19 | 1.00 | 4.953 | 0.10 | 0.495 | 4.98 |
| $T$ | Kelvin | 500 | 10 | 2.00 | 1 | 0.200 | 2.01 |
| Total | | | | | | | 14.97% |

Ignition delay uncertainty can be summarized by 6.58% as the sum of $t_{PT}$ and $ID_{time}$. While the MFC, the pre-chamber fueling, and the temperature uncertainty sum is 8.39%.

# 4. SUMMARY

An experiment was designed to study the hot jet ignition initiated from a stationary pre-chamber into a long aspect ratio optically accessible constant volume combustion chamber. A new constant volume combustor has been fabricated to study the effect of high initial temperature on ignition delay of methane and hydrogen fuel mixtures. A new heating system has been installed to supply hot air to the main chamber. A new fueling system has been developed to reduce the experiment set up time. A new control system has been designed to interface with an electronic ignition system, solenoid valves and a mass flow controller. A total of 226 initial tests were performed on methane, hydrogen, and 50% methane hydrogen mixtures. These mixtures equivalence ratio was varied from 0.4 to 1.5, and their initial temperature was from 297 K to 500 K. During all tests the pre-chamber equivalence ratio was fixed at 1.1, but it was filled at different initial pressure of 1, 1.5 and 2 times atmospheric pressure. The data was collected using high sampling rate pressure transducers and Schlieren images through a high speed camera. Initial reported results include ignition delay time estimation, and qualitative discussions of the Schlieren images. Ignition delay of methane mixtures was comparatively lower than ignition delay of methane hydrogen mixtures. Ignition delay was found to be proportional to equivalence ratio. The leaner mixtures had in general smaller ignition delays. Initial mixture temperature was found to affect ignition delay, but more investigation and analysis of the results is needed to determine the relationship. Hydrogen ignition delay results are not reported, and need further analysis. As a recommendation, the channel entrance design should be modified if further pure hydrogen ignition delay experiments are to be performed to enable visual observation of the early ignition steps.

# REFERENCES

# REFERENCES


[1] H. Burghard. German Patent DE485386C,1928.

[2] N. Energie-Forschungs-Fonds and H. Gränicher, *NEFF 1977-97: Förderung der Energieforschung : allgemeiner Rechenschaftsbericht zum Abschluss der Tätigkeit des NEFF; Bedeutung der NEFF-Förderung; zwanzig ausgewählte Forschungsprojekte*. vdf, Hochschulverlag an der ETH Zürich, 1997.

[3] Wikipedia, "Pressure wave supercharger — Wikipedia, the free encyclopedia." `http://en.wikipedia.org/w/index.php?title=Pressure%20wave%20supercharger&oldid=685585810`, 2017. [Online; accessed 13-March-2017].

[4] A. Ashiro. US Patent 4,563,997,1986.

[5] S. Claude. US Patent 2461186,1942.

[6] P. Akbari and M.R.Nalim, "Review of recent developments in wave rotor combustion technology," *Journal of Propulsion and Power*, vol. 25, no. 4, pp. 833–844, 2009.

[7] I. Perrera, "Experimental investigation into combustion torch jet ignition of methane-air, ethylene-air, and propane-air mixtures," Master's thesis, Indiana University Purdue University, 2010.

[8] M. R. Nalim, P. H. Snyder, and M. Kowalkowski, "Experimental test, model validation, and viability assessment of a wave-rotor constant-volume combustor," *Journal of Propulsion and Power*, vol. 33, pp. 163–175, 2016.

[9] Y. Matsutomi, S. Meyer, S. Wijeyakulasuriya, Z. Izzy, M. Nalim, M. Shimo, M. Kowalkowski, and P. Snyder, "Experimental investigation on the wave rotor constant volume combustor," *46th AIAA/ASME/SAE/ASEE Joint Propulsion Conference Exhibit*, 2010. Paper No:7043 - doi: 10.2514/6.2010.

[10] C. D. Cathey, T. Tang, T. Shiraishi, T. Urushihara, A. Kuthi, and M. A. Gundersen, "Nanosecond plasma ignition for improved performance of an internal combustion engine," *IEEE Transactions on Plasma Science*, vol. 35, no. 6, pp. 1664–1668, 2007.

[11] F. Wang, J. Liu, J. Sinibaldi, C. Brophy, A. Kuthi, C. Jiang, P. Ronney, and M. A. Gundersen, "Transient plasma ignition of quiescent and flowing air/fuel mixtures," *IEEE Transactions on Plasma Science*, vol. 33, no. 2, pp. 844–849, 2005.

[12] R. K. Prasad, S. Jain, G. Verma, and A. K. Agarwal, "Laser ignition and flame kernel characterization of HCNG in a constant volume combustion chamber," *Fuel*, vol. 190, pp. 318–327, 2017.

[13] D. K. Srivastava, K. Dharamshi, and A. K. Agarwal, "Flame kernel characterization of laser ignition of natural gas–air mixture in a constant volume combustion chamber," *Optics and Lasers in Engineering*, vol. 49, no. 9, pp. 1201–1209, 2011.

[14] N. Pavel, M. Tsunekane, K. Kanehara, and T. Taira, "Composite all-ceramics, passively q-switched nd: Yag/cr 4+: Yag monolithic micro-laser with two-beam output for multi-point ignition," in *2011 Conference on Lasers and Electro-Optics (CLEO)*, pp. 1–2, IEEE, 2011.

[15] K. Y. Paik, "Experimental investigation of hot jet ignition of methane-hydrogen mixtures in a constant volume combustor," Master's thesis, Indiana University Purdue University, 2016.

[16] A. Karimi, M. Rajagopal, and R. Nalim, "Traversing hot-jet ignition in a constant-volume combustor," *Journal of Engineering for Gas Turbines and Power*, vol. 136, no. 4, 2014. Paper No: GTP-13-1325; doi: 10.1115/1.4025659.

[17] E. Toulson, H. J. Schock, and W. P. Attard, "A review of pre-chamber initiated jet ignition combustion systems," tech. rep., SAE Technical Paper, 2010.

[18] T. Ma, H. Zhao, J. Li, and N. Ladommatos, "Experimental investigation of controlled auto-ignition (cai) combustion in a 4-stroke multi-cylinder gasoline engine and drive cycle simulations," *A new generation of engine combustion processes for the future*, pp. 115–124, 2001.

[19] M. Elhsnawi and A. Teodorczyk, "Experimental study of hot inert gas jet ignition of hydrogen-oxygen mixture," *First International Conference on Hydrogen Safety Pisa, Italy*, p. 8, 2005.

[20] R. Sadanandan, D. Markus, R. Schiel, U. Maas, J. Olofsson, H. Seyfried, M. Richter, and M. Alden, "Detailed investigation of ignition by hot gas jets," *Proceedings of the Combustion Institute, vol. 31, no. 1,*, pp. 719–726, 2007.

[21] I. Iglesias, M. Vera, A. L. Sanchez, and A. Linan, "Numerical analyses of deflagration initiation by a hot jet," *Combustion Theory and Modelling, vol. 16,no. 6*, pp. 994–1010, 2012.

[22] M. Bilgin, *Stationary and rotating hot jet ignition and flame propagation in a premixed cell.* PhD thesis, University of Washington, 1998.

[23] P. Chinnathambi, "Experimental investigation on traversing hot jet ignition of lean hydrocarbon-air mixtures in a constant volume combustor," Master's thesis, Indiana University Purdue University, 2014.

[24] Watlow, "Circulation heaters catalog." `http://www.watlow.com/en/products/heaters/circulation-heaters/watrod-firebar-circulation-heaters`, 2017. [Online; accessed 1-July-2017].

[25] Novus-Automation, "N1020 temperature controller - instructions manual v1.0x b." `http://www.advindsys.com/Manuals/Novus/ManualN1020English.pdf`, 2017. [Online; accessed 1-July-2017].

[26] M. G. Zabetakis, "Flammability characteristics of combustible gases and vapors," tech. rep., Bureau of Mines Washington DC, 1965.

[27] Horiba, *What is a mass flow controller?*, 2017 (accessed January 21, 2017). http://www.horiba.com/horiba-stec/products/mass-flow-technology/what-is-a-mass-flow-controller/.

[28] Coastal-Instruments, *Mass flow controller tutorial theory of operation*, 2017 (accessed January 21, 2017). http://mfchelp.com/mass-flow-controller-tutorial/theory-of-operation.

[29] T. R. Marrero and E. A. Mason, "Gaseous diffusion coefficients," *Journal of Physical and Chemical Reference Data*, vol. 1, no. 1, pp. 3–118, 1972.

[30] J. Kestin, K. Knierim, E. A. Mason, B. Najafi, S. T. Ro, and M. Waldman, "Equilibrium and transport properties of the noble gases and their mixtures at low density," *Journal of physical and chemical reference data*, vol. 13, no. 1, pp. 229–303, 1984.

[31] S. Socolofsky, "Concepts, definitions, and the diffusion equation." http://www.ifh.uni-karlsruhe.de/lehre/envflu_i/Downloads/course_script/ed2/ch1.PDF, 2017. [Online; accessed 13-March-2017].

[32] Wikipedia, "Linear regression — wikipedia, the free encyclopedia," 2017. [Online; accessed 13-July-2017].

[33] Y. Zhang, Z. Huang, L. Wei, J. Zhang, and C. K. Law, "Experimental and modeling study on ignition delays of lean mixtures of methane, hydrogen, oxygen, and argon at elevated pressures," *Combustion and Flame*, vol. 159, no. 3, pp. 918–931, 2012.

# APPENDIX

# A. SUMMARY OF DATA ANALYSIS PER TEST RUN

| Case | $Test\#$ | $P$ | $\phi$ | Shock (m/s) | $t_{ID}(ms)$ | $P_{far}(psig)$ | $Freq(Hz)$ |
|---|---|---|---|---|---|---|---|
| $CH_4$ | 214 | 1 | 0.4 | 376.21 | 11.68 | 27.32 | 757.58 |
| $T = 297K$ | 215 | 2 | 0.7 | 365.62 | 15.99 | 46.3 | 1086.96 |
| | 216 | 1 | 1 | 381.75 | 12.45 | 37.28 | 862.07 |
| | 217 | 1.5 | 0.4 | 370.84 | 10.65 | 38.65 | 847.46 |
| | 218 | 1.5 | 0.4 | 370.84 | 11.06 | 33.75 | 862.07 |
| | 219 | 2 | 1 | 365.62 | 16.49 | 71.1 | 1149.43 |
| | 220 | 2 | 0.4 | 370.84 | 25.34 | 40.04 | 787.4 |
| | 221 | 1.5 | 0.7 | 360.54 | 11.86 | 68.95 | 0 |
| | 222 | 1 | 0.7 | 376.21 | 12.07 | 41.13 | 862.07 |
| | 223 | 1.5 | 1 | 370.84 | 15.77 | 60.11 | 1136.36 |
| | 224 | 1 | 1.5 | 387.44 | NA | 0 | 0 |
| | 225 | 2 | 1.5 | 387.44 | 23.99 | 53.36 | 0 |
| | 226 | 1.5 | 1.5 | 370.84 | 24.38 | 39.53 | 0 |
| $CH_4$ | 153 | 1 | 0.7 | 463.55 | 12.09 | 30.92 | 1030.93 |
| $T = 500K$ | 154 | 1 | 1 | 455.42 | 17.65 | 37.23 | 1162.79 |
| | 155 | 1 | 1 | 455.42 | 17.09 | 43.8 | 1282.05 |
| | 156 | 1.5 | 0.7 | 447.57 | 12.97 | 46.73 | 1176.47 |
| | 157 | 1.5 | 1 | 463.55 | 15.3 | 51.72 | 1086.96 |
| | 158.1 | 1.5 | 1 | 447.57 | 16.08 | 55.35 | 1136.36 |
| | 158 | 1.5 | 0.4 | 463.55 | 8.3 | 29.53 | 826.45 |
| | 159 | 1.5 | 0.7 | 447.57 | 11.95 | 49.99 | 1123.6 |
| | 160 | 1.5 | 0.7 | 455.42 | 9.28 | 47.32 | 1818.18 |
| | 161 | 2 | 1 | 447.57 | 13.55 | 67.82 | 1298.7 |

| Case | $Test\#$ | $P$ | $\phi$ | Shock (m/s) | $t_{ID}(ms)$ | $P_{far}(psig)$ | $Freq(Hz)$ |
|---|---|---|---|---|---|---|---|
| | 162 | 1.5 | 1 | 455.42 | 18.88 | 60.18 | 1265.82 |
| | 163 | 1.5 | 0.7 | 463.55 | 10.83 | 50.6 | 1075.27 |
| | 164 | 2 | 0.7 | 455.42 | 8.3 | 49.8 | 2173.91 |
| | 166 | 2 | 0.4 | 432.65 | 12.31 | 38.36 | 1851.85 |
| | 167 | 2 | 0.4 | 439.98 | 10.48 | 36.74 | 925.93 |
| | 168 | 2 | 0.4 | 447.57 | 9.04 | 44.86 | 2631.58 |
| | 169 | 1 | 0.4 | 439.98 | 9.62 | 20.55 | 800 |
| | 170 | 2 | 1.5 | 432.65 | 21.78 | 51.11 | 1123.6 |
| | 171 | 2 | 1.5 | 432.65 | 35.21 | 2500 | |
| | 172 | 2 | 1.5 | 439.98 | 25.71 | 49.19 | 2000 |
| | 173 | 1.5 | 1.5 | 439.98 | 29.26 | 33.39 | 2173.91 |
| | 174 | 1 | 1.5 | 0 | NA | 0 | 0 |
| $CH_4$ | 175 | 1 | 1 | 439.98 | 14.36 | 46.51 | 2040.82 |
| $T = 500K$ | 176 | 1 | 0.4 | 0 | NA | 0 | 0 |
| | 177 | 1 | 0.7 | 455.42 | 11.44 | 26.37 | 1724.14 |
| | 178 | 1.5 | 1 | 432.65 | 13.24 | 62.45 | 2325.58 |
| | 179 | 2 | 0.4 | 432.65 | 9.49 | 50.93 | 2173.91 |
| | 180 | 1.5 | 0.7 | 463.55 | 6.99 | 53.01 | 2222.22 |
| | 181 | 2 | 1 | 432.65 | 12.32 | 77.7 | 2380.95 |
| | 182 | 1.5 | 0.4 | 432.65 | 9.68 | 30.07 | 2000 |
| | 183 | 2 | 0.7 | 455.42 | 7.7 | 60.64 | 2325.58 |
| | 184 | 1.5 | 1.5 | 425.55 | NA | 38.09 | 2325.58 |
| | 185 | 2 | 1.5 | 447.57 | 20.44 | 74.49 | 1250 |
| $CH_4/H_2$ | 30 | 1 | 0.4 | 376.21 | 6.28 | 34.02 | 847.46 |
| $T = 297K$ | 32 | 1 | 1 | 387.44 | 11.24 | 94.7 | 1234.57 |
| | 33 | 1 | 0.7 | 393.32 | 5.52 | 89.19 | 1041.67 |
| | 34 | 1.5 | 1 | 381.75 | 12.42 | 110.98 | 1098.9 |
| | 35 | 1.5 | 0.4 | 376.21 | 9.01 | 60.48 | 900.9 |

| Case | $Test\#$ | $P$ | $\phi$ | Shock (m/s) | $t_{ID}(ms)$ | $P_{far}(psig)$ | $Freq(Hz)$ |
|---|---|---|---|---|---|---|---|
| | 38 | 1.5 | 0.7 | 360.54 | 8.62 | 82.29 | 1010.1 |
| | 40 | 2 | 0.4 | 387.44 | 8 | 75.63 | 1041.67 |
| | 41 | 2 | 1 | 393.32 | 11.67 | 102.89 | 1086.96 |
| | 42 | 1.5 | 0.7 | 393.32 | 6.92 | 87.63 | 1020.41 |
| | 43 | 1.5 | 0.7 | 370.84 | 9.08 | 105.53 | 1030.93 |
| | 44 | 1.5 | 0.4 | 381.75 | 7.5 | 57.85 | 877.19 |
| | 45 | 1 | 0.7 | 381.75 | 8.12 | 73.52 | 980.39 |
| | 46 | 2 | 0.7 | 381.75 | 12.37 | 122.06 | 1063.83 |
| | 47 | 2 | 0.4 | 376.21 | 9.49 | 75.5 | 943.4 |
| $CH_4/H_2$ | 48 | 1 | 1 | 399.37 | 11.45 | 67.44 | 1010.1 |
| $T = 297K$ | 49 | 2 | 1 | 381.75 | 13.37 | 104.13 | 1123.6 |
| | 50 | 2 | 1 | 387.44 | 11.8 | 151.85 | 1265.82 |
| | 51 | 1 | 1 | 393.32 | 10.38 | 73.05 | 1111.11 |
| | 52 | 1.5 | 1 | 399.37 | 13.98 | 86.55 | 1234.57 |
| | 53 | 1 | 0.7 | 405.61 | 7.66 | 73.9 | 1063.83 |
| | 54 | 2 | 0.4 | 393.32 | 10.97 | 72.31 | 1052.63 |
| | 55 | 1.5 | 0.4 | 381.75 | 7.15 | 42.4 | 900.9 |
| | 56 | 1.5 | 1 | 393.32 | 10.69 | 74.59 | 1086.96 |
| | 57 | 2 | 0.7 | 393.32 | 10 | 112.4 | 1219.51 |
| | 58 | 1 | 0.4 | 393.32 | 5.63 | 28.64 | 775.19 |
| | 59 | 1 | 0.4 | 387.44 | 4.35 | 32.41 | 847.46 |
| | 227 | 1 | 1.5 | 405.61 | 20.45 | 41.82 | 1086.96 |
| | 228 | 1.5 | 1.5 | 412.04 | 15.6 | 51.05 | 0 |
| | 229 | 2 | 1.5 | 399.37 | 13.42 | 69.03 | 1123.6 |
| $CH_4/H_2$ | 60 | 1 | 1 | 418.69 | 15.62 | 60.69 | 1111.11 |
| $T = 400K$ | 61 | 1 | 0.4 | 405.61 | 6.07 | 50.3 | 1000 |
| | 62 | 1 | 0.7 | 412.04 | 12.23 | 61.57 | 1136.36 |
| | 63 | 1.5 | 1 | 412.04 | 14.92 | 78.93 | 1492.54 |

| Case | $Test\#$ | $P$ | $\phi$ | Shock (m/s) | $t_{ID}(ms)$ | $P_{far}(psig)$ | $Freq(Hz)$ |
|---|---|---|---|---|---|---|---|
| | 64 | 1.5 | 0.7 | 412.04 | 11.29 | 77.88 | 1111.11 |
| | 65 | 2 | 1 | 425.55 | 9.47 | 102.77 | 1204.82 |
| | 66 | 1.5 | 0.7 | 418.69 | 8.85 | 74.86 | 1219.51 |
| | 67 | 2 | 0.4 | 418.69 | 8.15 | 78.33 | 1086.96 |
| | 68 | 1 | 0.7 | 432.65 | 9.22 | 63.41 | 1351.35 |
| | 69 | 1 | 0.4 | 425.55 | 9.22 | 60.68 | 980.39 |
| | 70 | 2 | 0.7 | 412.04 | 9.1 | 90.97 | 1408.45 |
| | 71 | 1.5 | 0.4 | 432.65 | 8 | 55.86 | 1408.45 |
| | 72 | 1.5 | 0.7 | 425.55 | 12.69 | 76.41 | 1666.67 |
| $CH_4/H_2$ | 73 | 1.5 | 0.7 | 412.04 | 13.12 | 75.88 | 2941.18 |
| $T = 400K$ | 74 | 1 | 1 | 412.04 | 11.63 | 67.79 | 2272.73 |
| | 76 | 1.5 | 0.7 | 405.61 | 11.71 | 76.76 | 1449.28 |
| | 78 | 2 | 1 | 418.69 | 13.56 | 87.91 | 1388.89 |
| | 79 | 1 | 0.4 | 425.55 | 8.94 | 55.56 | 1010.1 |
| | 80 | 1.5 | 1 | 418.69 | 12.89 | 76.48 | 1204.82 |
| | 81 | 1 | 0.7 | 425.55 | 9.6 | 69.73 | 1086.96 |
| | 82 | 1 | 1 | 425.55 | 13.06 | 58.26 | 2325.58 |
| | 83 | 1.5 | 0.7 | 412.04 | 11.54 | 79.57 | 1562.5 |
| | 84 | 2 | 0.7 | 418.69 | 8.44 | 90.24 | 1724.14 |
| | 85 | 1.5 | 0.4 | 412.04 | 9.2 | 71.68 | 1020.41 |
| | 233 | 2 | 1.5 | 439.98 | 17.24 | 70.54 | 0 |
| | 234 | 1.5 | 1.5 | 418.69 | 16.34 | 55.74 | 0 |
| | 235 | 1 | 1.5 | 432.65 | 15.33 | 45.27 | 0 |
| $CH_4/H_2$ | 111 | 1 | 0.7 | 447.57 | 8.97 | 53 | 2272.73 |
| $T = 500K$ | 112 | 1 | 1 | 463.55 | 10.49 | 60.69 | 2083.33 |
| | 113 | 1.5 | 0.7 | 447.57 | 8.93 | 71.78 | 1162.79 |
| | 114 | 1.5 | 1 | 439.98 | 7.02 | 69.27 | 1234.57 |
| | 115 | 1.5 | 0.4 | 432.65 | 6.22 | 35.44 | 1851.85 |

| Case | $Test\#$ | $P$ | $\phi$ | Shock (m/s) | $t_{ID}(ms)$ | $P_{far}(psig)$ | $Freq(Hz)$ |
|---|---|---|---|---|---|---|---|
| | 116 | 1.5 | 0.7 | 439.98 | 9.89 | 56.38 | 2272.73 |
| | 117 | 1.5 | 0.7 | 418.69 | 8.47 | 67.21 | 1388.89 |
| | 118 | 2 | 1 | 463.55 | 11.92 | 69.63 | 2272.73 |
| | 119 | 1.5 | 0.7 | 439.98 | 10.92 | 54.24 | 1818.18 |
| | 120 | 2 | 0.7 | 412.04 | 14.61 | 62.4 | 2127.66 |
| | 121 | 1 | 0.4 | 432.65 | 4.25 | 22.54 | 2272.73 |
| | 122 | 2 | 0.4 | 425.55 | 9.07 | 44.71 | 1960.78 |
| | 123 | 1.5 | 0.7 | 418.69 | 11.15 | 61.26 | 1041.67 |
| | 124 | 2 | 0.7 | 455.42 | 11.66 | 67.39 | 1052.63 |
| | 125 | 1 | 0.4 | 412.04 | 6.27 | 23.05 | 1470.59 |
| | 126 | 2 | 0.4 | 447.57 | 9.92 | 52.25 | 2083.33 |
| | 127 | 1 | 0.5 | 439.98 | 4.06 | 29.87 | 1818.18 |
| | 128 | 1 | 0.3 | NA | NA | 0 | NA |
| | 129 | 1 | 0 | NA | NA | 0 | NA |
| $CH_4/H_2$ | 186 | 1 | 1 | 463.55 | 15.75 | 39.81 | 1960.78 |
| $T = 500K$ | 187 | 1 | 0.4 | 418.69 | 5.98 | 28.54 | 2000 |
| | 188 | 1 | 0.7 | 432.65 | 14.27 | 40.36 | 1612.9 |
| | 189 | 1.5 | 1 | 405.61 | 17.26 | 58.51 | 2272.73 |
| | 190 | 2 | 0.4 | 425.55 | 11.67 | 51.49 | 2000 |
| | 191 | 1.5 | 0.7 | 412.04 | 11.3 | 50.53 | 2272.73 |
| | 192 | 2 | 1 | 463.55 | 11.15 | 72.44 | 2325.58 |
| | 193 | 1.5 | 0.4 | 439.98 | 6.08 | 35.61 | 1960.78 |
| | 194 | 2 | 0.7 | 447.57 | 8.69 | 63.54 | 1639.34 |
| | 195 | 1.5 | 1.5 | 432.65 | 19.97 | 44.08 | 0 |
| | 196 | 2 | 1.5 | 418.69 | 18.8 | 63.95 | 1315.79 |
| | 197 | 1 | 1.5 | 463.55 | NA | 0 | NA |
| $H_2$ | 86 | 1 | 0.4 | 387.44 | NA | 53.49 | 2173.91 |
| $T = 297K$ | 87 | 1 | 0.7 | 425.55 | 0.95 | 122 | 3225.81 |

| Case | $Test\#$ | $P$ | $\phi$ | Shock (m/s) | $t_{ID}(ms)$ | $P_{far}(psig)$ | $Freq(Hz)$ |
|---|---|---|---|---|---|---|---|
| | 89 | 1.5 | 0.4 | 405.61 | 1.21 | 175.6 | 2857.14 |
| | 90 | 1.5 | 0.7 | 418.69 | 1.05 | 216.2 | 2857.14 |
| | 91 | 1.5 | 1 | 463.55 | 0.82 | 141.94 | 1369.86 |
| | 93 | 2 | 0.4 | 381.75 | 1.91 | 119.93 | 1041.67 |
| | 94 | 2 | 0.7 | 432.65 | 1.16 | 157.44 | 1408.45 |
| | 95 | 2 | 1 | 471.98 | 0.72 | 199.55 | 1492.54 |
| | 96 | 1 | 0.4 | NA | NA | 0 | NA |
| | 97 | 1 | 1 | NA | NA | 0 | NA |
| | 98 | 1 | 0.7 | 435.55 | 1.46 | 0 | NA |
| | 99 | 1 | 1 | NA | NA | 0 | NA |
| | 100 | 1.5 | 0.7 | 439.98 | 0.84 | 0 | NA |
| | 101 | 1.5 | 1 | 471.98 | 0.92 | 181.25 | NA |
| | 102 | 1.5 | 0.4 | 412.04 | 0.98 | 86.26 | NA |
| | 103 | 1.5 | 0.7 | 432.65 | 1.14 | 211.85 | NA |
| | 104 | 1.5 | 0.7 | 432.65 | 0.99 | 106.86 | NA |
| $CH_4/H_2 - E$ | 243 | 1 | 1 | 432.65 | 4.02 | | |
| $T = 297K$ | 244 | 1 | 0.4 | 439.98 | 4.95 | | |
| | 245 | 1 | 0.7 | 441.48 | 5.62 | | |
| | 246 | 1 | 1 | 444.5 | 5.91 | | |
| | 247 | 1 | 0.4 | 441.48 | 4.61 | | |
| | 248 | 1 | 0.7 | 432.65 | 4.54 | | |
| | 249 | 1 | 1 | 447.57 | 7.38 | | |
| | 250 | 1.5 | 0.4 | 425.55 | 6.58 | | |
| | 251 | 1.5 | 0.7 | 421.41 | 6.24 | | |
| | 252 | 1.5 | 1 | 426.95 | 7.26 | | |
| | 253 | 1.5 | 0.4 | 424.16 | 5.28 | | |
| | 254 | 1.5 | 0.7 | 399.37 | 7.47 | | |
| | 255 | 1.5 | 1 | 416.01 | 8.05 | | |

| Case | $Test\#$ | $P$ | $\phi$ | Shock (m/s) | $t_{ID}(ms)$ | $P_{far}(psig)$ | $Freq(Hz)$ |
|---|---|---|---|---|---|---|---|
| | 256 | 2 | 0.4 | 432.65 | 6.58 | | |
| | 257 | 2 | 0.7 | 418.69 | 6.84 | | |
| | 258 | 2 | 1 | 435.55 | 6.5 | | |
| | 259 | 2 | 0.4 | 418.69 | 4.49 | | |
| | 260 | 2 | 0.7 | 412.04 | 5.99 | | |
| | 261 | 2 | 1 | 435.55 | 6.1 | | |
| | 262 | 1 | 0.7 | 447.57 | 5.38 | | |
| | 263 | 1.5 | 0.7 | 439.98 | 6.52 | | |

Table A.1: Summary of preliminary analysis of test data. $t_{ID}(ms)$ is ignition delay time in milliseconds. $P_{far}(psig)$ is the peak pressure in the main chamber in psig. $Freq(Hz)$ is the shock wave frequency measured from the peak far pressure to the next consecutive peak.

# B. DATA EXTRACTION USING PYTHON

Data extraction of rupture pressure from the labview pressure data given a table listing ignition delay time corresponding to each labview file. Python code written for batch processing of all the test files .

```
"""
This function takes a lvm or csv file and look at the first
two columns after a number of rows for the rupture time from column
one. It returns the corresponding pressure in column two. It takes
the closest to rupture time in the list, if the input
variable trup is not exactly matched. It needs an input file
list to scan through your list of trup and list of lvm or
csv files. It writes an output csv file with the corresponding
trup and the found pressure from column 2.
All lvm files to be scanned and the list input file
should be in the same folder with find_pressure_infile.py
---in line split use "," for csv and "\t" for lvm
---Written by Ali T. ali.tarraf@gmail.com 6/17/17
"""
import csv

def find_pressure_infile(trup,filename):
#initialise time and pressure list
    a=[]
    time=[]
    pressure=[]
```

```
    f=open(filename,'r').readlines()
    N=len(f)-1
# split the lvm file by the tab delimiter and read
#line by line and save columns after row 70
    for i in range(70,N):
        a= f[i].split("\t")
        time.append(float(a[0]))
        pressure.append(float(a[1]))

    def locate_time(trup,time):
    #function locates the closest time to the
    #Trupture time available in the data list
        diff=[]
        for i in time:
            diff.append(abs(trup-i))
        return diff.index(min(diff))

    return pressure[locate_time(trup,time)]

"""
print find_pressure_infile(0.036105528,
"215A10.147B 19_14.750H2885_53.12_16-12-19_1231.lvm")
"""
#open the input file stored as test number, time rupture , file name
c = open('list.csv','r').readlines()
N=len(c)-1
pressurelist=[]
test=[]
time=[]
```

```
#read the input file list.csv line by line and use trup and
#filename as input to find pressure infile function
for y in range(1,N):
    x=c[y].split(',')
    pressurelist.append(find_pressure_infile(float(x[1]),x[2][:-1]))
    #[:-1] to remove the /n newline at the end of the string
    test.append(float(x[0]))
    time.append(float(x[1]))

#save test,time,pressurelist in a results file
with open('results.csv', 'w') as f:
    writer = csv.writer(f, delimiter=',')
    writer.writerows(zip(test,time,pressurelist))
```

# C. DESIGN DRAWINGS

Drawings included in this section are design drawings. Machining of the actual parts led to modifications which were not documented in the current drawings. To the author best knowledge, differences between the drawings in this section and the final parts are summarized in the table below. Double check all measurements on actual parts before making design decisions.

| Drawing | Notes |
|---|---|
| Main chamber center block | Added two 1/2" NPT holes for air inlet and outlet |
| | Holes position is different than displayed on drawings |
| Main chamber seal | New design is different with O-ring on front and back |
| Wear plate | 4 holes drilled instead of 6 as shown in drawing |

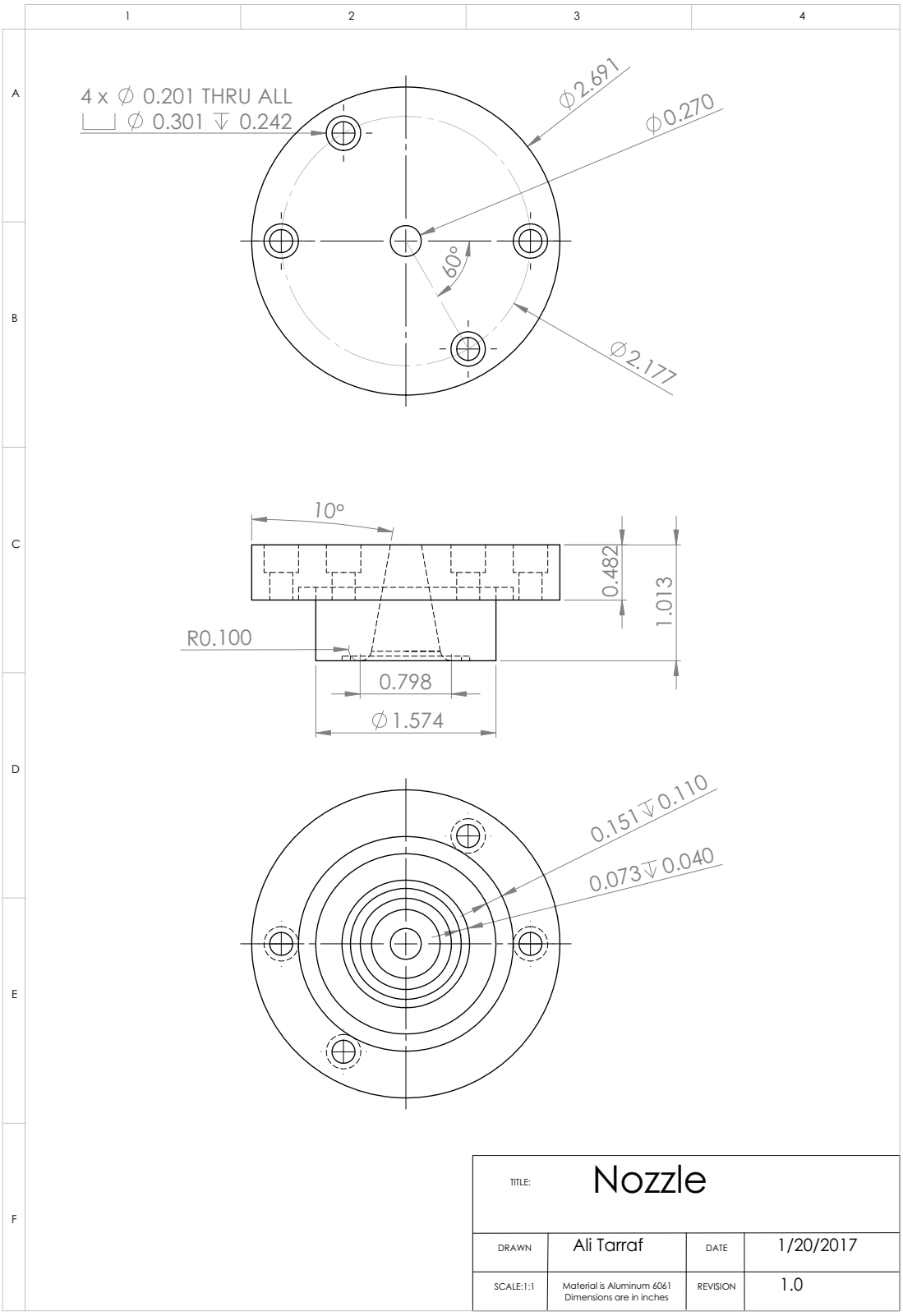


Fig. C.1.: New machined nozzle

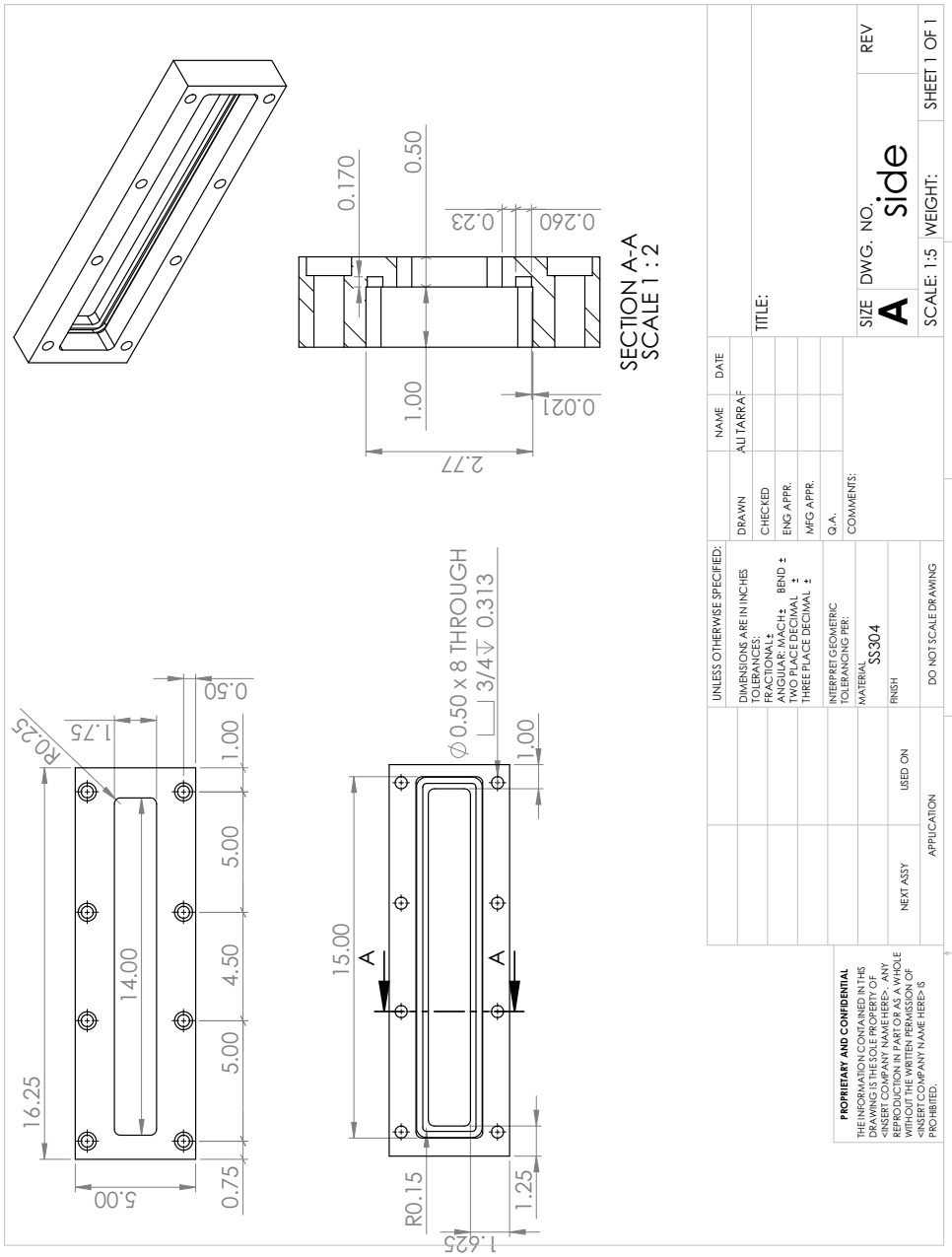


Fig. C.2.: Chamber block side drawing

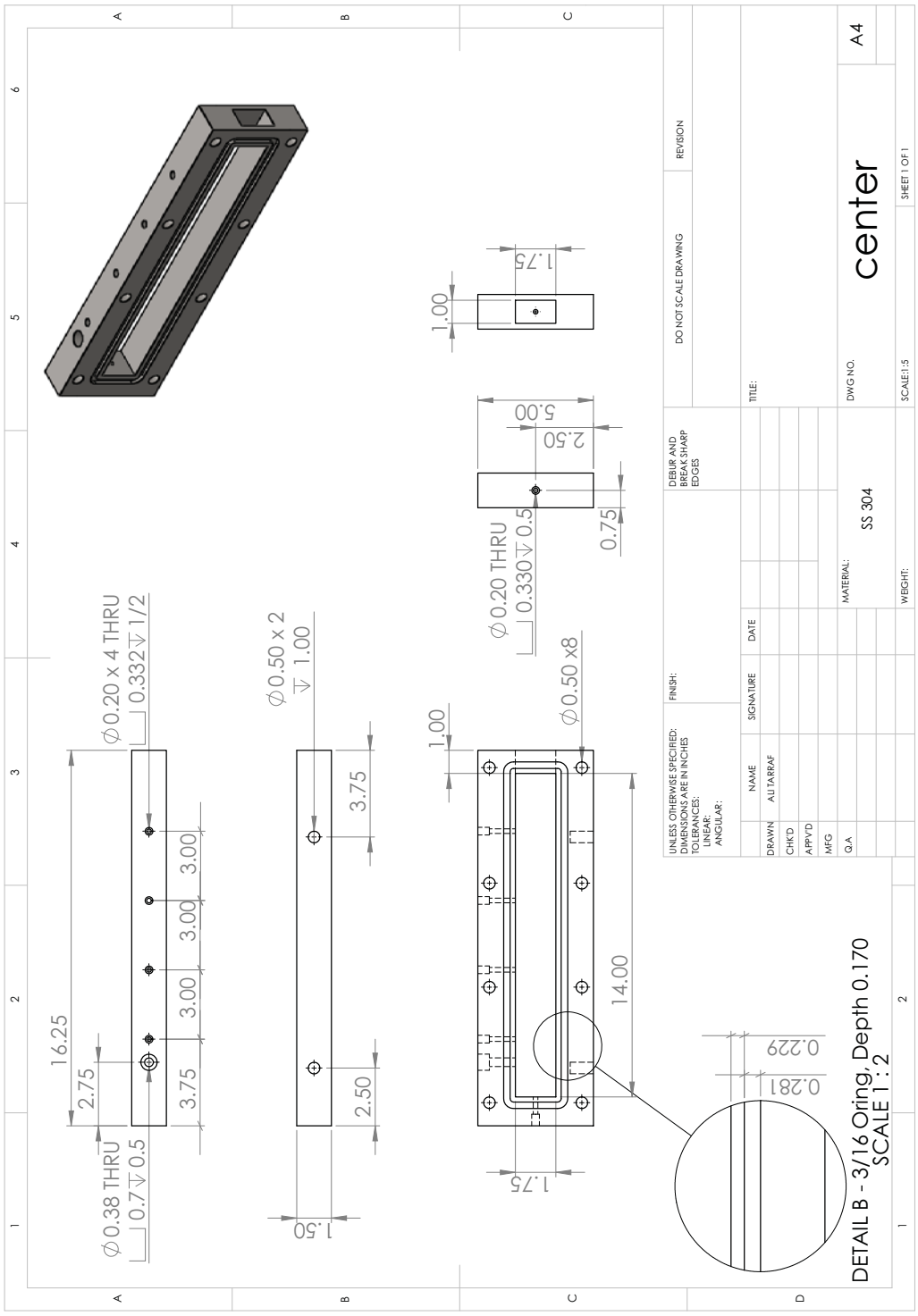


Fig. C.3.: Chamber block center drawing

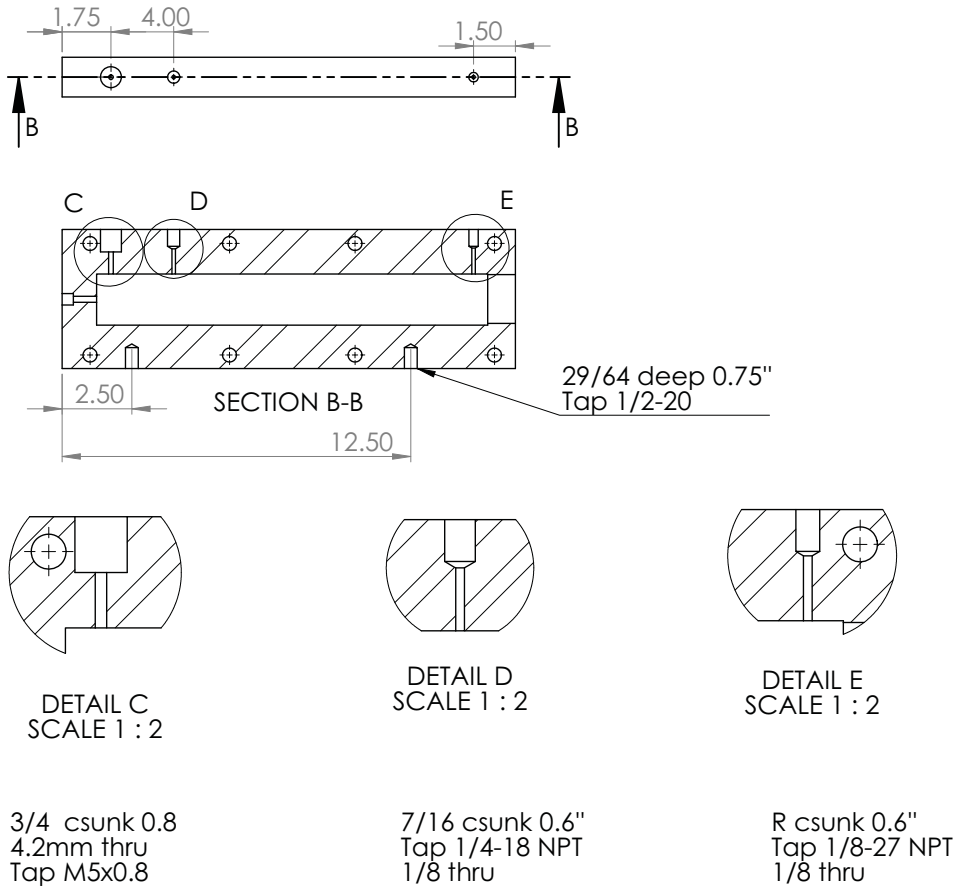


Fig. C.4.: Hole drilling specifications

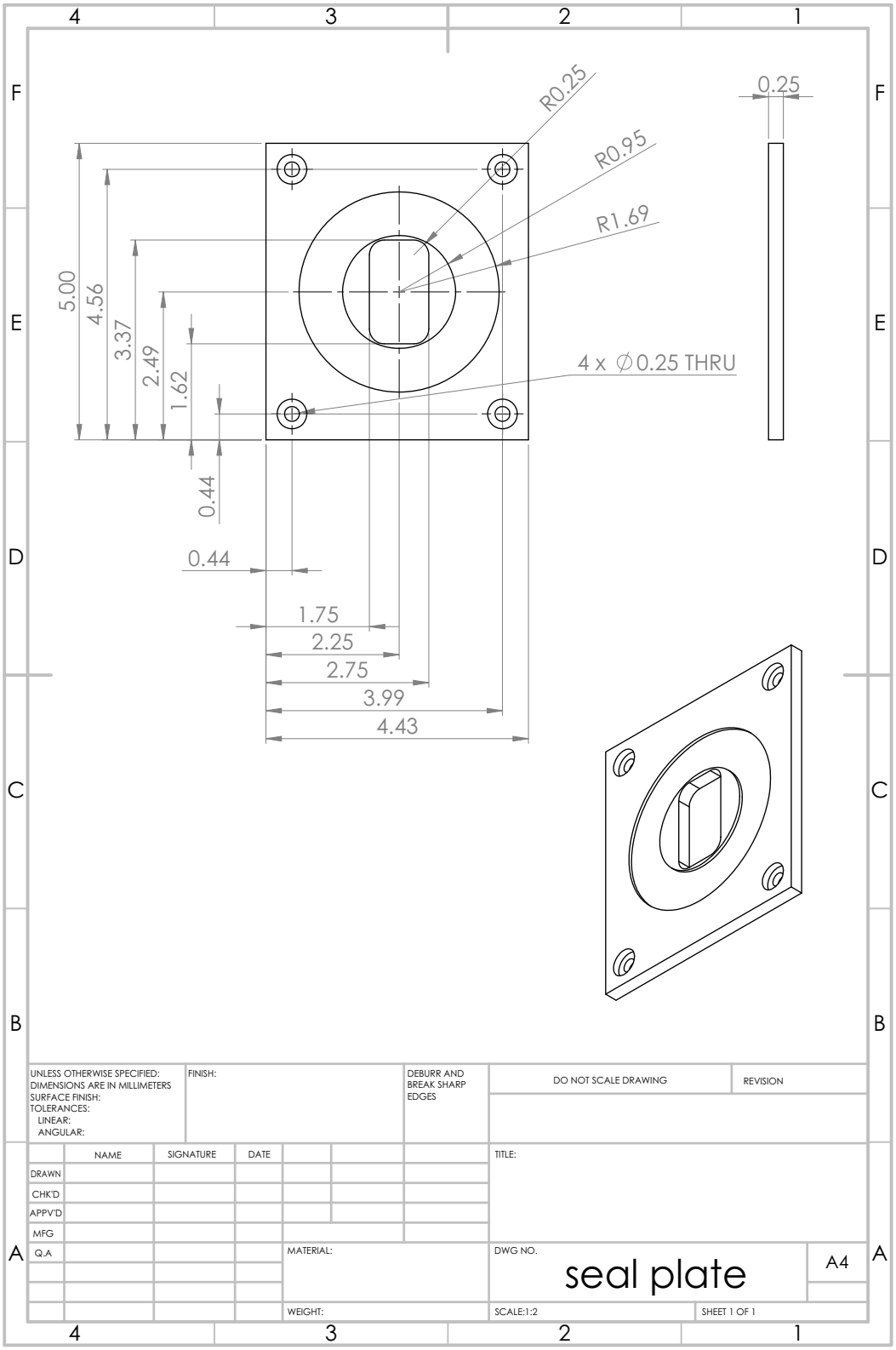


Fig. C.5.: Seal plate for main chamber version 1. This design was not successful, and a new seal plate was machined with O-ring grooves along the rectangular opening on the front and back of the plate as shown in section

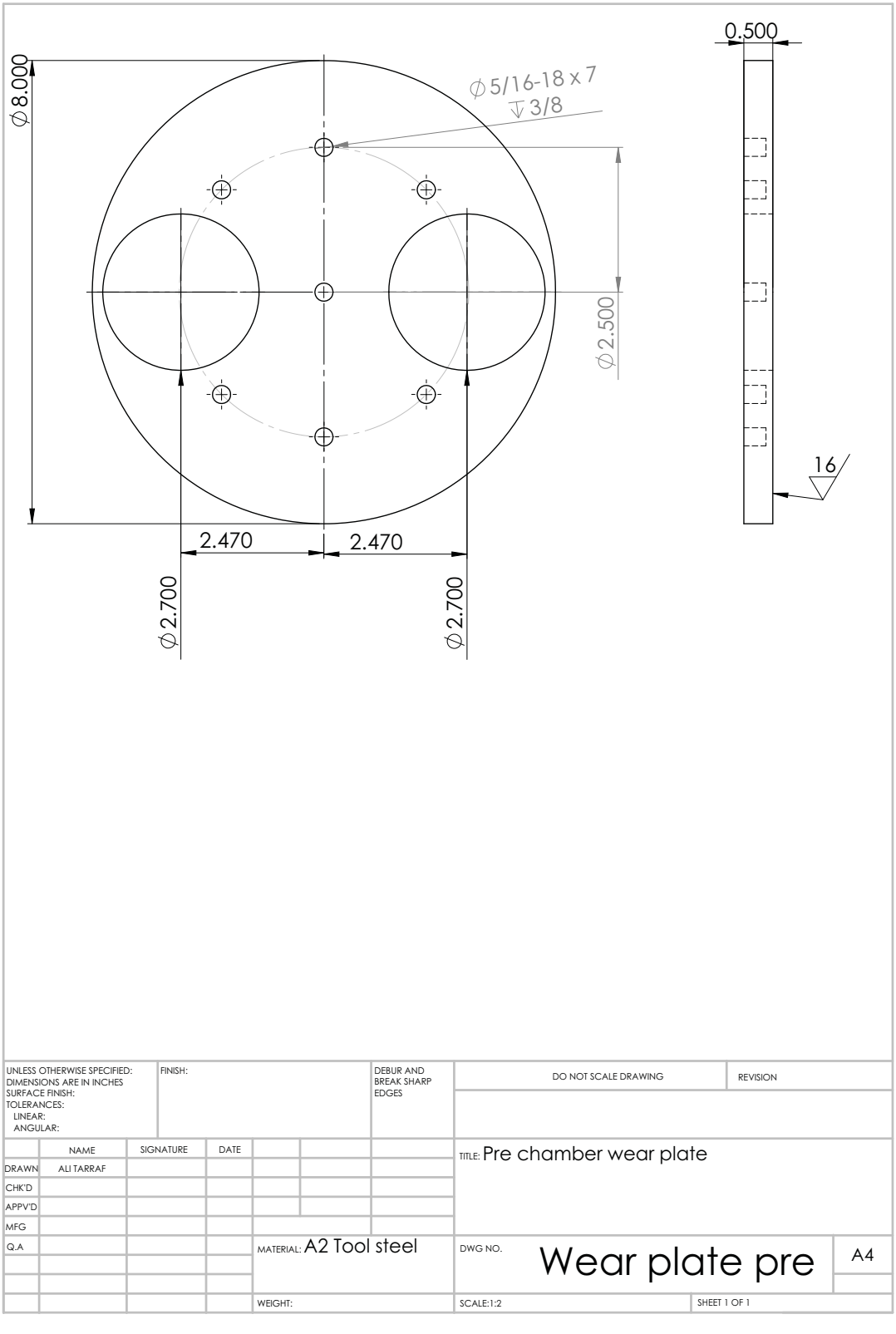


Fig. C.6.: Wear plate machined out of A2 tool steel for the pre-chamber

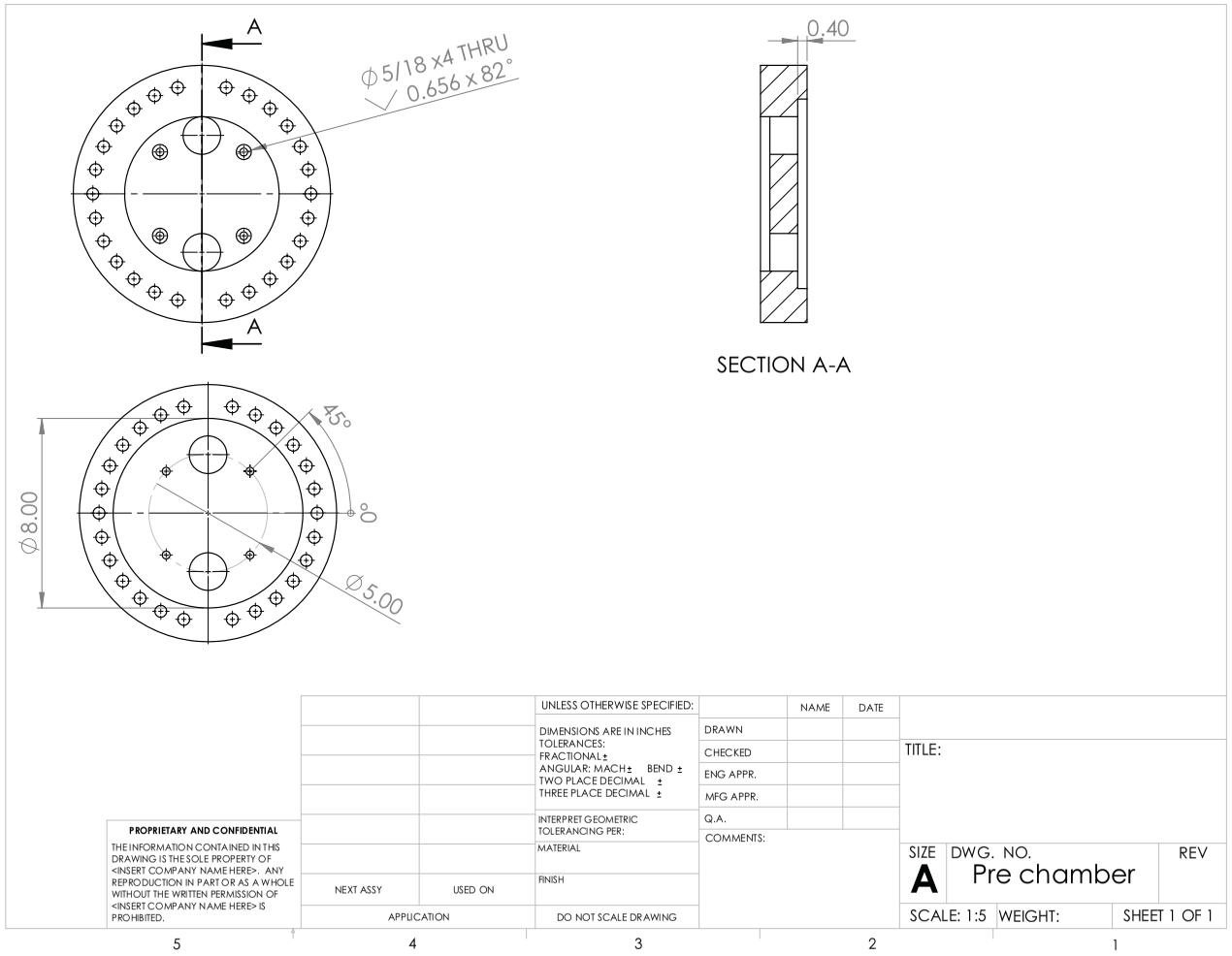


Fig. C.7.: Pre-chamber front cylinder block pocket drawing to fit in the A2 tool steel wear plate

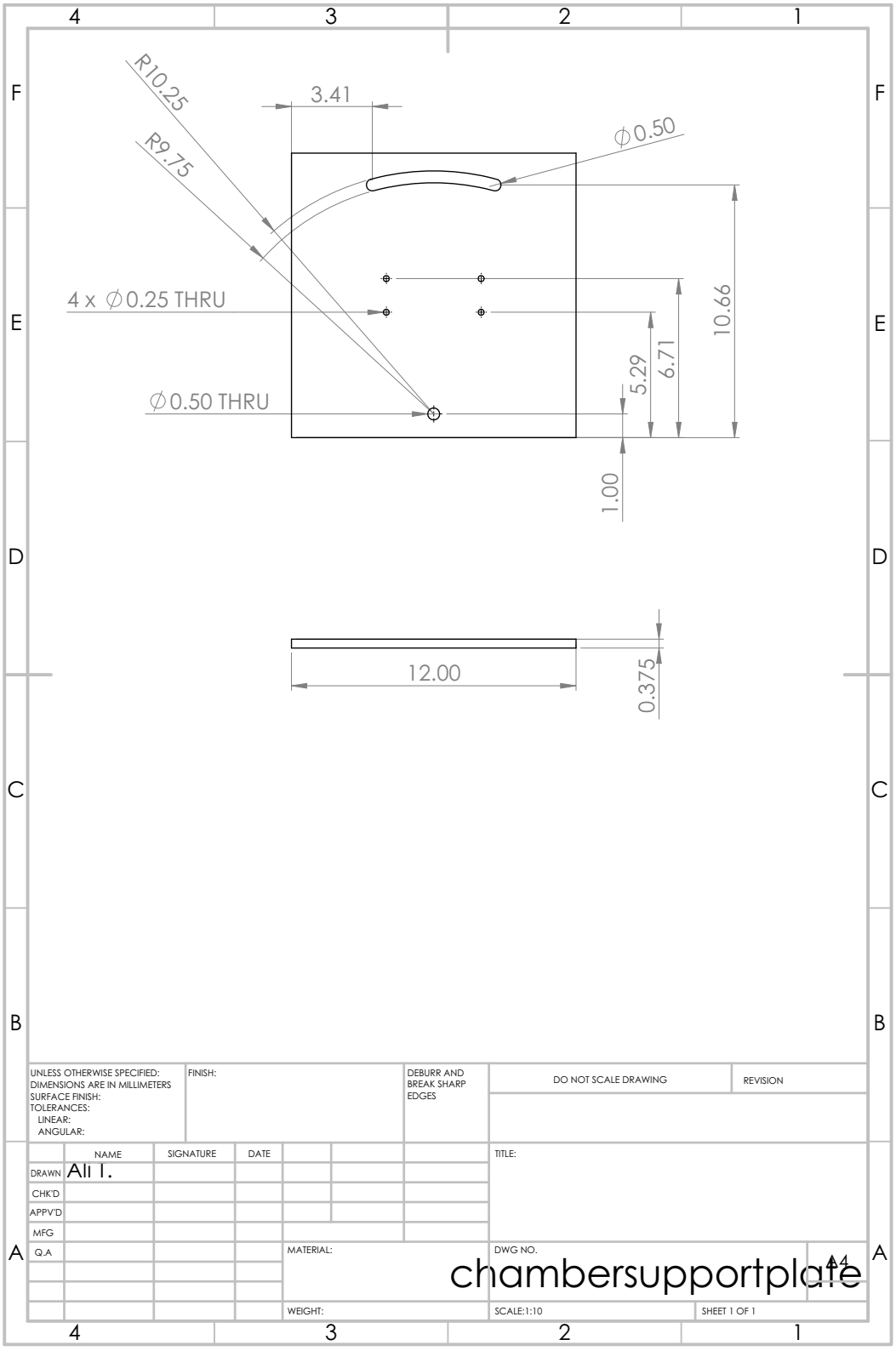


Fig. C.8.: Main chamber support plate to be fixed on the xy positioning table

# D. DESIGN AND MANUFACTURING FIGURES

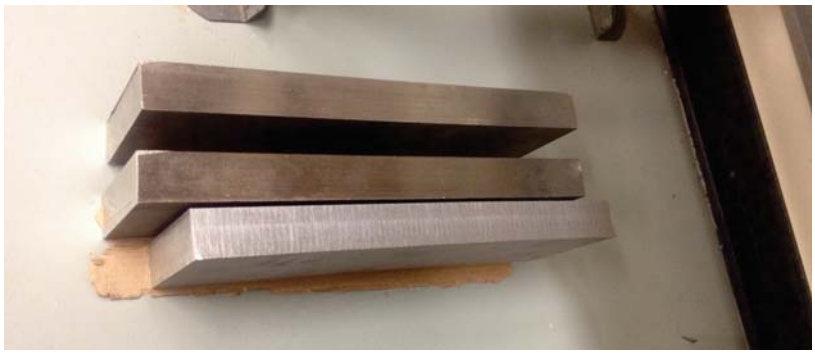

Fig. D.1.: Raw stock of Stainless Steel 304 blocks before machining. Stocks rectangular cuts were performed by a water-jet machine, and the rest of the details was precision machined with a CNC.

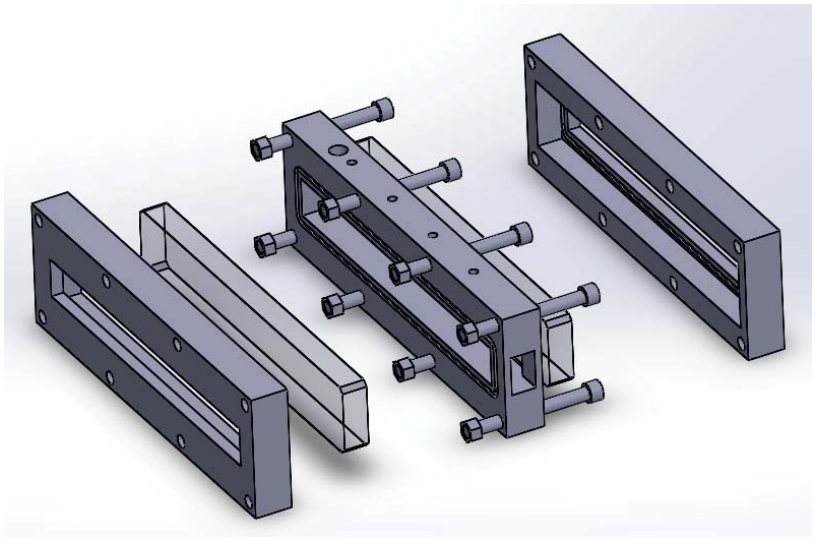

Fig. D.2.: Main chamber exploded CAD drawing

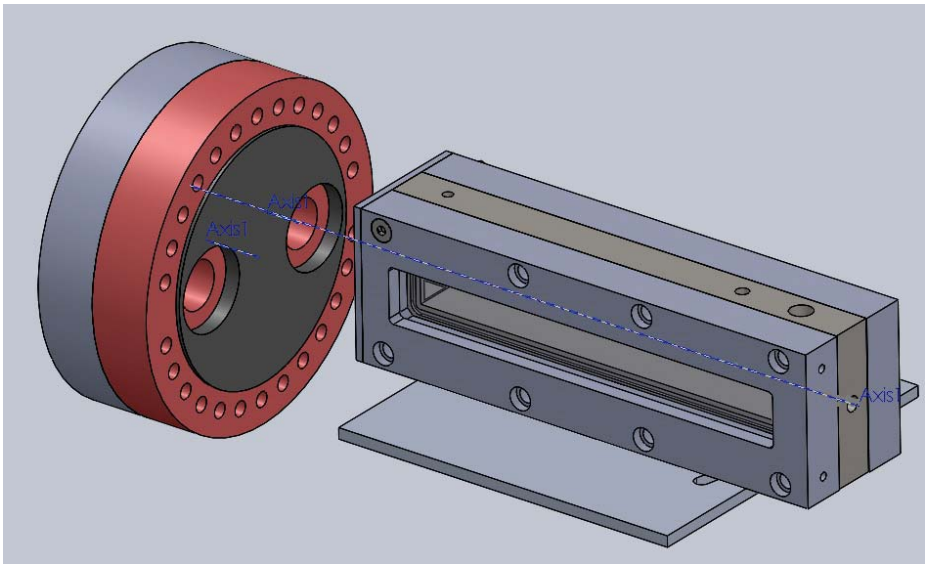


Fig. D.3.: Main chamber and Pre-chamber assembly CAD drawing

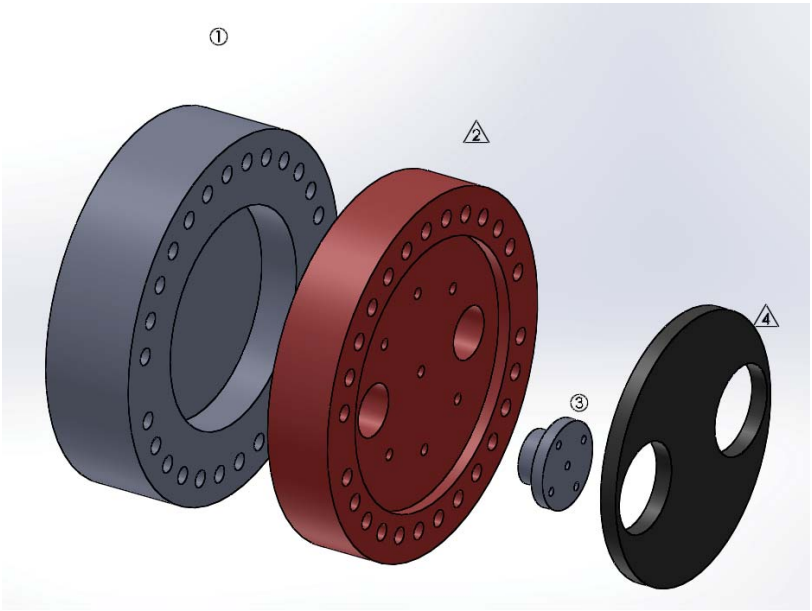


Fig. D.4.: Wear plate and Pre-chamber exploded drawing

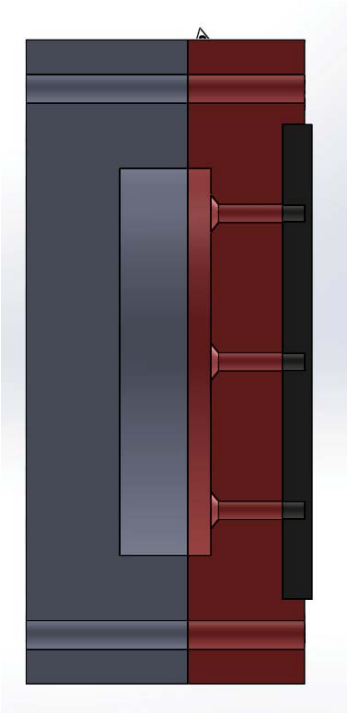

Fig. D.5.: Wear plate and Pre-chamber cross section drawing

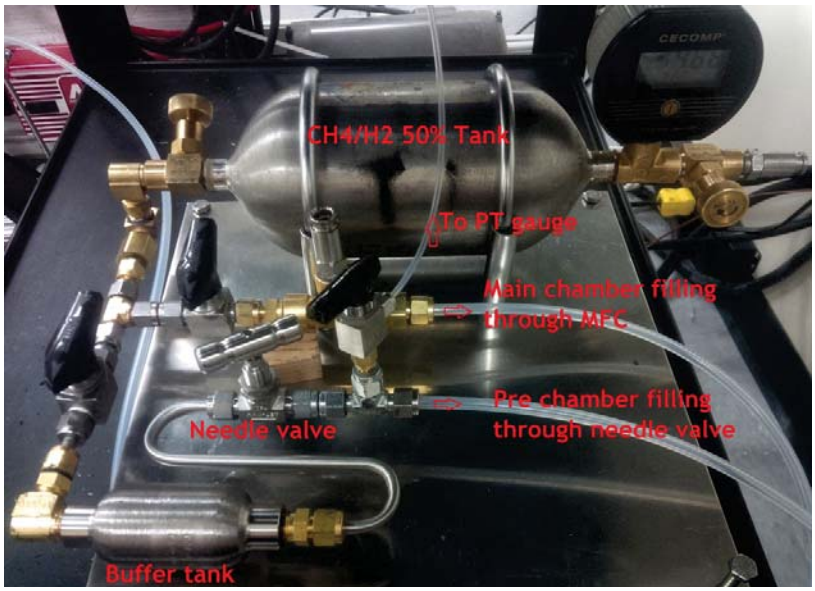


Fig. D.6.: New mixing station developed for pre-chamber and main chamber fueling using MFC